Politecnico di Torino

ScuDo
Scuola di Dottorato ~ Doctoral School
WHAT YOU ARE, TAKES YOU FAR

Doctoral Dissertation
Doctoral Program in Electronic Engineering (35^{th}cycle)

Advanced modeling of nanoscale devices for analog applications

By

Eva Catoggio

******

Supervisor(s):
Prof. Simona Donati Guerrieri, Supervisor
Prof. Fabrizio Bonani, Co-Supervisor

Doctoral Examination Committee:
Prof. Teresa María Martín-Guerrero, Referee, Universidad de Málaga
Prof. Valeria Vadalà, Referee, Università degli Studi di Milano-Bicocca

Politecnico di Torino
2023

Declaration

I hereby declare that, the contents and organization of this dissertation constitute my own original work and does not compromise in any way the rights of third parties, including those relating to the security of personal data.

Eva Catoggio
2023

* This dissertation is presented in partial fulfillment of the requirements for **Ph.D. degree** in the Graduate School of Politecnico di Torino (ScuDo).

To my grandfather

Acknowledgements

I would like to acknowledge the Microwave and Optoelectronic Group of Politecnico di Torino, in particular my supervisors Simona Donati Guerrieri and Fabrizio Bonani for the great opportunity they gave me and for all the support, advice and help throughout my PhD. I would also like to thank my collegues Gemma Giliberti and Alberto Gullino with whom I shared this experience from the beginning and for the beautiful friendship created during these three years. Last but not least, I want to thank Matteo Cagnoni for the valuable advice and great support not only at work, but also at personal level.

Abstract

Physics-based simulations are a powerful tool to analyze the behavior of semiconductor devices under different operating conditions. Due to the continued shrinking of transistor dimensions, the scenario of semiconductor device technology is nowadays characterized by the significant technological variability and difficult thermal management, strongly affecting the device operation and producing a spread of their performances. Physics-based sensitivity analysis is the ideal tool to link physical/technological parameter variations to the device performance spread, but its numerical burden may prove to be a limiting factor in the widespread diffusion of TCAD tools, especially in frequency-dependent multi-harmonic analyses. One way to overcome this limit is to rely on new agile and flexible techniques, such as the Green's Function (GF) approach.

This thesis presents the framework of advanced physics-based modeling for the peculiar needs of microwave devices. An in-house, pre-existing 2D physics-based simulator, allowing for large-signal multi-tone periodic and quasi-periodic analysis through the Harmonic Balance technique, has been extended and optimized. The original version of the in-house code, implementing the drift-diffusion model, has been improved through the treatment of more accurate temperature dependencies in the most important materials, e.g. Silicon, GaAs, GaN. The worsening of environmental conditions makes thermal management increasingly important, leading to the need of implementing the self-heating equation. The investigation of trap signatures, another fundamental aspect to achieve good RF performances, has been accounted implementing the trap rate equation. These advanced capabilities make the in-house simulator able to evaluate frequency dispersion effects related to temperature and trapping mechanisms, also including an interplay of traps and thermal dynamics. Moreover, the TCAD solver has been extended to allow for efficient sensitivity analyses in both static and dynamic conditions through the GF technique, with the aim of assessing the device response to a small physical/technological parameter variation,

e.g. temperature, doping concentration, trap energy, etc. These improvements make the TCAD solver very appealing with respect to commercial tools for the simulation of nanoscale devices in analog RF/microwave applications.

The research activity has addressed two significant case studies to demonstrate the TCAD capabilities. A T-dependent sensitivity analysis is presented on a 54 nm Si FinFET Class A Power Amplifier (PA) in both the DC case, including self-heating, and the LS regime. The analysis demonstrates the accuracy of the GF technique and its advantage in terms of simulation time of about 20%. Thermal sensitivity affects all operating conditions, showing more than 1 dB output power reduction at $T = 350$ K. LS T-dependent simulations are also performed with the concurrent variation of an additional parameter, i.e. load and doping concentration of the source/drain regions. The analyses are carried out with no extra numerical burden and demonstrate that temperature variations dominate over load sensitivity, while concurrent doping variations further affect the PA 1 dB compression point.

The TCAD high computational cost suggests that it cannot be used routinely for circuit design, but it can a basis to extract computationally efficient circuit-level models. As a demonstrator, a complete dynamic electro-thermal analysis has been developed on the same PA exploiting the T-dependent X-parameter model, exported from TCAD simulations into EDA tools. The accuracy of the T-dependent X-parameter model is demonstrated by comparing circuit simulations with TCAD results in continuous wave, including self-heating. The analysis is extended to pulsed modulated operation, highlighting thermal dynamic effects as a function of the pulse period. Finally, the pulsed operated analysis is repeated for a Class B PA to highlight the different role of thermal memory.

TCAD analysis represents a unique opportunity to investigate the impact of traps in the GaN technology: DC and AC GF-based sensitivity analyses are performed on a 0.150 μm Fe-doped AlGaN/GaN HEMT through to the variation of a trap physical parameter, e.g. trap energy and concentration, showing accurate results with respect to repeated TCAD simulations. Traps are responsible for the low-frequency dispersion peak of the Y-parameters, which is shifted towards higher values with decreasing trap energy level. Furthermore, the GF approach allows to extract the local sensitivity, giving a unique insight into the device operating conditions and showing the parts of the device where traps influence most the HEMT AC parameter.

Contents

List of Figures

List of Tables

List of Symbols

C_{th}	Thermal Capacitance
D_n	Electron Diffusivity
D_p	Hole Diffusivity
E_{C}	Conduction Band Energy
E_{Fi}	Intrinsic Fermi Level
E_{F}	Fermi Level
E_{V}	Valence Band Energy
E_{g}	Energy Gap
E_{t}	Trap Energy Level
$E_{\mathrm{F}n}$	Electron Quasi-Fermi Level
$E_{\mathrm{F}p}$	Hole Quasi-Fermi Level
F_{hfs}	Driving Force
J_{D}	Displacement Current Density
N_{A}	Acceptor impurity concentration
N_{C}	Conduction Band Density of States
N_{D}	Donor impurity concentration
N_{V}	Valence Band Density of States

N_t	Total Trap Concentration
P_diss	Dissipated Power
R_th	Thermal Resistance
T	Lattice Temperature
U_0	Vacuum Energy Level
U_n	Electron Recombination Rate
U_p	Hole Recombination Rate
V_T	Thermal Voltage
Z_th	Thermal Impedance
χ	Electron Affinity
ε	Permittivity
$\hbar$	Reduced Planck Constant
$\mathbf{i}$	Current
$\mathbf{E}$	Electric Field
$\mathbf{Z}$	Circuit Impedance Matrix
$\mathbf{P}$	Total Polarization Vector
μ_n	Electron Mobility
μ_p	Hole Mobility
ϕ	Electrostatic Potential
ϕ_B	Schottky Barrier
ϕ_M	Metal Workfunction
ϕ_r	Reference Potential
ρ	Space Charge density

ρ_{F} Fixed Charge

σ Trap Cross Section

σ_n Electron Conductivity

σ_p Hole Conductivity

τ_n Electron Lifetime

τ_p Average Momentum Relaxation Time

τ_p Hole Lifetime

$\mathbf{J}_n$ Electron Current density

$\mathbf{J}_p$ Hole Current density

θ_{C} Reference Potential Difference

$\mathbf{v}$ Voltage

$\mathbf{v}_n$ Average Electron Velocity

$\mathbf{v}_p$ Average Hole Velocity

c^n Electron Capture Rate

c^p Hole Capture Rate

e^n Electron Emission Rate

e^p Hole Emission Rate

f^n Electron Occupation Probability

k_{B} Boltzmann Constant

$m_{\mathrm{eff},n}$ Electron Effective Mass

$m_{\mathrm{eff},p}$ Hole Effective Mass

n Electron Concentration

n_{t} Occupied Trap Concentration

n_i	Intrinsic Concentration
p	Hole Concentration
q	Electron Elementary Charge
q_{PE}	Volumic Polarization Charge
v_{th}^{n}	Electron Thermal Velocity
v_{th}^{p}	Hole Thermal Velocity
v_{sat}	Saturation Velocity

Chapter 1

Introduction

Physics-based simulation is a powerful way to understand, optimize and design semiconductor devices under different operating conditions, through the development of physical models describing electrical, optical and thermal properties. Technology Computer-Aided Design (TCAD) simulators are the best environment to accurately describe the behavior of active devices. Their development started in the late 1960s from underlying the fundamental physical principles of bipolar technology and moving on with an increasingly in-depth analysis of the scaling issues related to the Very-Large-Scale-Integration (VLSI) technology. The hierarchy of TCAD tools, shown in Fig. 1.1, starts from *process simulation*, aimed at modeling the fabrication of semiconductor devices giving information about geometry, doping profiles, contact placement; the first modeling tool in this panorama was SUPREM developed by Stanford University, later commercialized by Silvaco, Inc. These data are then exploited by *device simulation* in order to analyze the physical behavior of semiconductor devices providing an output in terms of temperature, voltage and current as a function of time or frequency; very common examples are Synopsys TCAD Sentaurus and PADRE. Finally, terminal current and voltages are the basis for *circuit simulation*, aimed at the generation of compact models; a well-known example is SPICE.

The growth of VLSI technology is due to the continued shrinking of transistors to even smaller dimensions, leading to higher packing densities, higher circuit speeds, low power dissipation and lower cost per unit function realized. These benefits have been a central role during the years, leading to today's computers, wireless units and

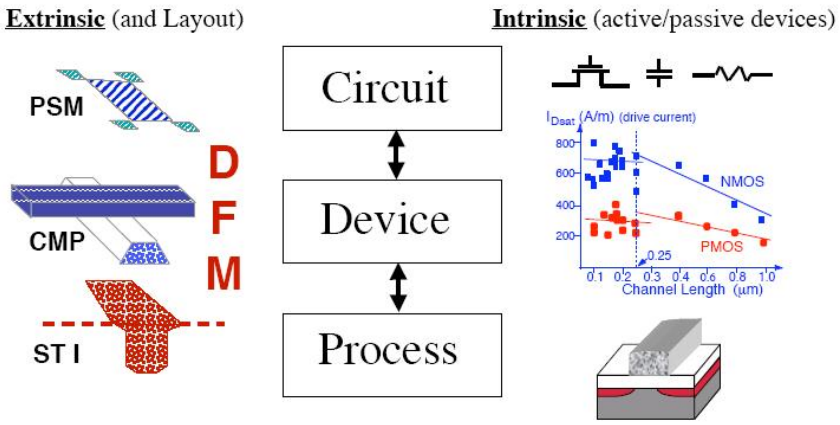

Fig. 1.1 Hierarchy of TCAD tools.

communication systems characterized by better performances, lower cost and smaller size [15]. Nevertheless, the miniaturization process has led to a significant technological variability and a difficult thermal management, which strongly affect the electron device operation and produce a spread of their performances. An efficient way to evaluate the device performance variation is the *sensitivity analysis*, which provides information in terms of threshold voltage, saturation current and subthreshold slope in digital applications, while relevant parameters become the power gain, harmonic distortion and efficiency in analog RF/microwave circuits. In this scenario, physics-based sensitivity analysis is the ideal tool to link physical and technological parameter variations to the device performance spread. Nevertheless, TCAD analysis of RF/microwave devices is limited by the important numerical burden of physics-based simulations, especially in frequency-dependent multi-harmonic analyses. The high computational cost is further worsened not only in three-dimensional (3D) structures, but also in simulations accounting for deterministic or random concurrent variations of multiple parameters (e.g. temperature and source/drain doping concentration). In the last years, numerically efficient TCAD sensitivity analysis has been introduced exploiting, for example, the Green's Function approach, and reaching the right compromise between accuracy and computational cost. Several TCAD commercial tools, such as Synopsys Sentaurus, are able to perform these kinds of analyses in 2D or 3D dimensions, but limited to the DC conditions only. In-house physics-based implementations overcome these issues, restricting the analysis to the 2D case, but allowing for frequency-dependent sensitivity simulations [16].

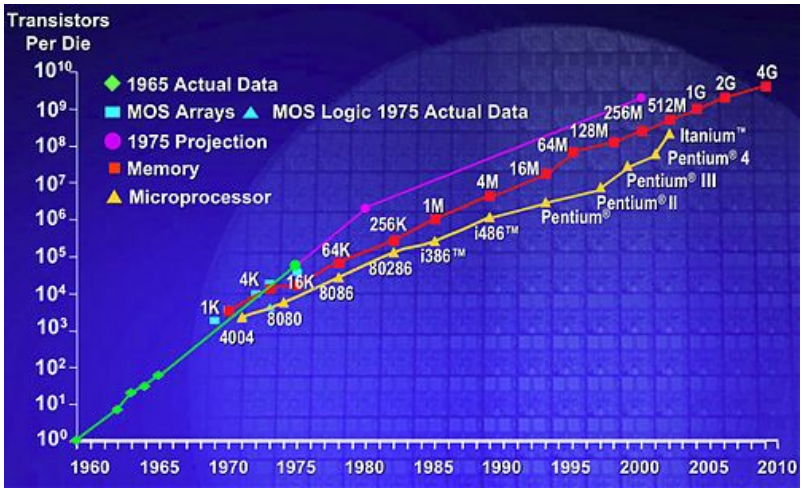

Fig. 1.2 Electronic circuits miniaturization.

Nowadays, technological variability, ever increasing with the development of the new technology nodes, is a relevant issue in device fabrication, especially in nanometer scale MOSFETs, FinFETs, UTB-SOI, FDSOI and AlGaN/GaN HEMTs [17]. It is considered a device parameter as important as performance improvements in meeting the requirements of Moore's Law and can be more easily mitigated in digital than analog circuits. The overall uncertainty in device perfomance can be affected by various phenomena, including process variations, inherent spread of physical parameters, induced crystal strain or thermal stress. Process variations refer to the variation in the manufacturing process, such as gate length, gate dielectric thickness or doping, and lead to performance differences from one device to another, even if they are fabricated on the same wafer. The inherent spread of physical parameters is related to the material variability in terms of mobility, trapped charge density or metal work function, having a stronger impact in conjunction with induced crystal strain or thermal stress [17]. Many studies have been carried out in order to investigate variability: in MOSFET devices random dopant fluctuations (RDFs) in the channel are the main contributor to the threshold voltage fluctuations. Fig. 1.3 shows the threshold voltage variability σ_{V_T} of a MOSFET, measured on different gate dimensions and scales, providing a picture of *global variability* within a wafer and *local variability* in two cases: within mismatch-paired MOSFETs and within SRAM cells, for an in-depth investigation on how the distance between devices can impact on σ_{V_T} [1]. Fabrication process-induced fluctuations also affect the device performance in RF/microwave applications, such as mixers or power amplifiers.

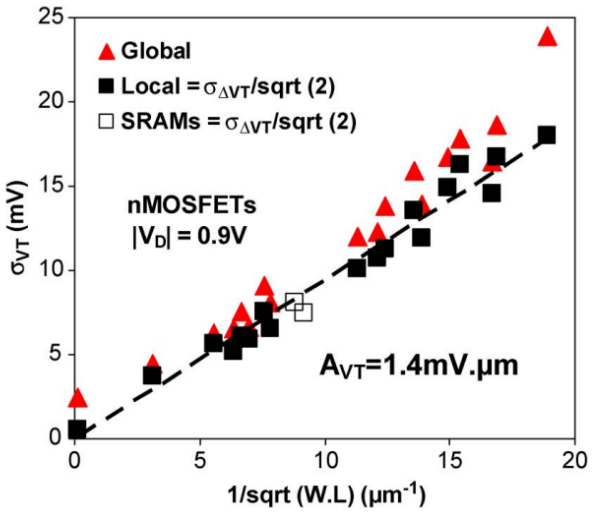

Fig. 1.3 V_T standard deviation at different levels [1]. Triangles: within-wafer (global variability). Filled squares: within-mismatch-structure (local variability). Empty squares: within-SRAM-cells.

For instance, Fig. 1.4 shows the output power and the Power-Added Efficiency (PAE) due to process fluctuations simulated on a 24-GHz class-AB power amplifier topology, based on a 65-nm MOSFET technology [2].

The thermal management is another critical issue: in any given technology the power dissipation of active and passive devices makes heat generation inevitable and the poor heat dissipation to the surroundings leads to a local temperature increase, namely the self-heating effect. Moreover, the semiconductor industry has been pushing towards extremely scaled technologies and higher performance, leading to the use of new material systems, such as III-V semiconductors, and the development of new non-planar devices, such as FinFETs. Their peculiar 3D structure brings along a set of parasitics, in terms of mutual capacitances and access resistances, due to the scaled interconnects and the reduced device drive capability related to the small size. Consequences of these choices are the further increase of the local power dissipation and, hence, of self-heating. One of the earliest examples of this phenomenon, reported in literature, dates back to 1989, when Mautry and Trager measured a local temperature increase up to 60 K in a MOSFET with design dimensions $W/L = 10/0.6\ \mu$m and supply voltage of 5 V [3], demonstrating a linear behavior with respect to power dissipation (see Fig. 1.5). In planar structures, this heat dissipation to the bulk occurs through lateral spreading, while in 3D architectures, there is

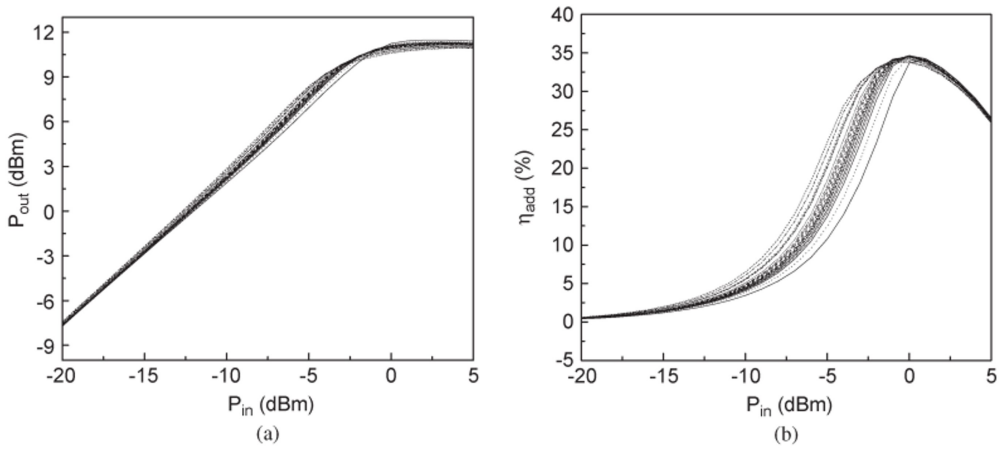

Fig. 1.4 Power amplifier performance fluctuation of (a) the output power and (b) the PAE as a function of the input power [2].

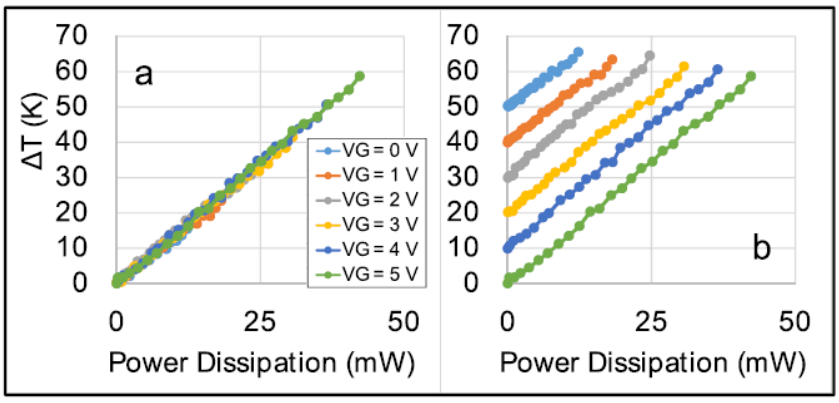

Fig. 1.5 Temperature increase as a function of power dissipation on a 0.6 μm-MOSFET [3]. Left: total variation vs. power. Right: curves for each gate bias offset for clarity starting with zero offset at 5 V and increasing by 10 K for each lower gate voltage.

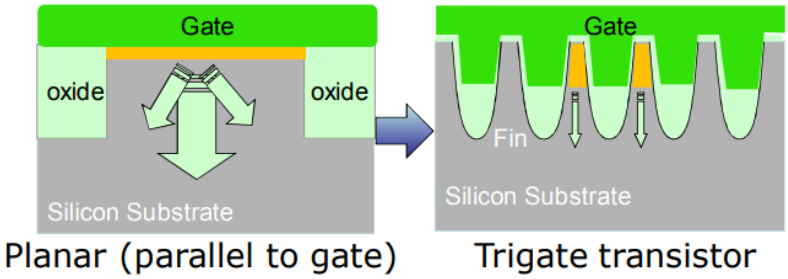

Fig. 1.6 Heat dissipation through the substrate in planar (left) and 3D (right) structures [4].

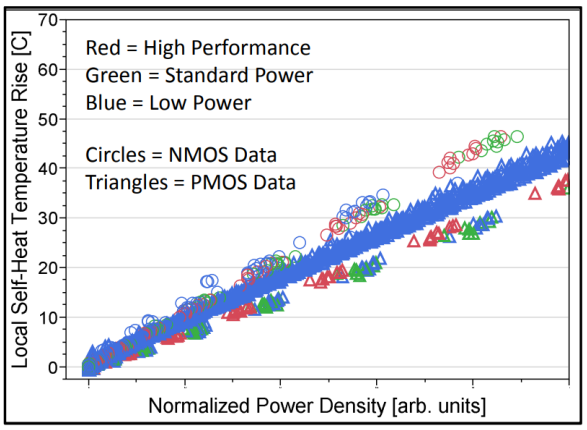

Fig. 1.7 Measurements of local temperature rise on the metal sensor as a function of the normalized input power. The input power is such that the power dissipation is mainly in the channel region and reduced at the contact resistances [4].

a potential higher thermal resistance due to the lateral isolation, as shown in Fig. 1.6. For instance, the local self-heating can be extracted as a function of the input power, using metal-line thermometers above large multi-gate MOS transistors as test structures [4]. In this way, the temperature coefficient of the metal resistance is exploited to measure the local temperature. In Fig. 1.7, the extracted local temperature rise shows a linear behavior for three different Intel's 22 nm Tri-Gate transistors, targeted for analog applications thanks to the cut-off frequency higher than 200 GHz and the maximum frequency up to 4 THz. The layout size has a strong influence on the drain current degradation, in fact a multi-fin multi-gate structure has higher temperature increase and lower current with respect to a small-single-fin device, as shown in Fig. 1.8.

Furthermore, the deployment of III-V semiconductors, such as Gallium Nitride (GaN) and Aluminum Nitride (AlN), finds a match in GaN-based HEMT devices,

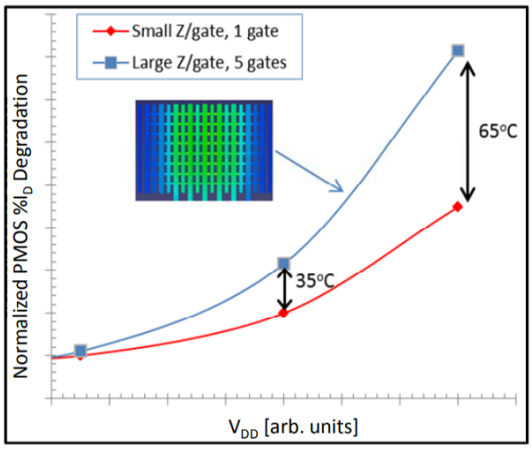

Fig. 1.8 Drain current degradation vs. drain voltage in different device layouts [4].

which have a great relevance in high-power and high-frequency applications. In fact, nitride-based semiconductors are promising materials thanks to their superior properties, such as wide band gap, high electron mobility, high breakdown voltage and high saturation velocity. Nevertheless, they are characterized by the high cost of the growth techniques, mainly due to the presence of dislocation layers, which may compromise their optical and electrical properties [18]. In fact, HEMT technology is affected by trapping and de-trapping mechanisms due to the presence of deep-level traps, which degrade the dynamic device performance. The type of traps and their localization inside the structure play a key role to determine RF performances and device reliability. The investigation of trap signatures has been carried out in many different ways including pulsed measurements and, more recently, also with low-frequency Y-parameters measurements and simulations in a Fe-doped AlGaN/GaN HEMT of 0.150 μm gate length and 8×50 μm gate width [5]. In particular, Fig. 1.9 shows two frequency peaks of the Y_{21} parameter from 25 °C to 75 °C: the positive one is associated to surface traps localized at the interface between the AlGaN barrier and the oxide passivation layer, while the negative one is due to the presence of buffer traps. Moreover, the temperature increase shifts the two peaks towards higher frequency values.

Purpose of this thesis is the extension and optimization of a pre-existing two-dimensional in-house physics-based simulator, implementing large-signal and small-signal-large-signal simulations through the Harmonic Balance technique. With this aim, the original version of the in-house code has been improved through the treatment of all temperature dependencies involved in a wide set of physical

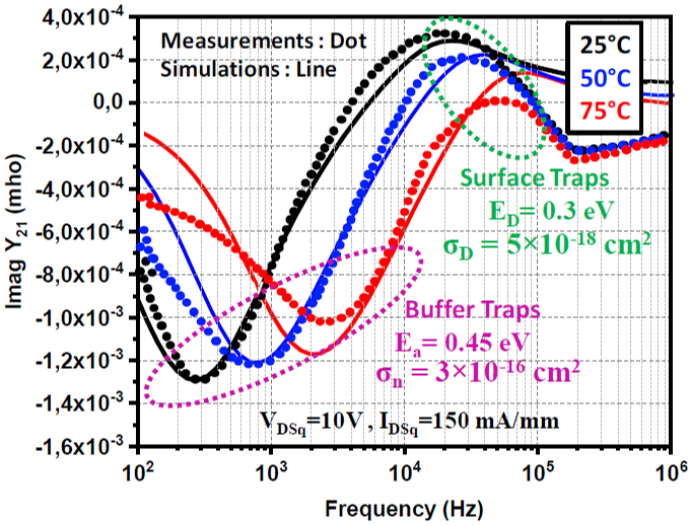

Fig. 1.9 Imaginary part of the Y_{21} parameter at different temperatures [5].

models. Furthermore, the device heat dissipation has been accounted allowing for both parametric temperature variations and self-heating. The temperature-dependent in-house solver has been further enriched through the refinement of the trap rate equation for the investigation of different trapping mechanisms and the introduction of new physical models suited for the analysis of heterostructures and/or nitride-based semiconductor devices. These improvements make the TCAD solver suited for the simulation of nanoscale devices for analog RF/microwave applications, which are typically modeled in large-signal multi-tone periodic or quasi-periodic operating conditions. Moreover, the enhanced version of the TCAD solver opens the way to sensitivity analyses aimed at evaluating the device performance spread due to the variation of temperature or of a trap model parameter. In the second instance, the thesis also highlights how in-house physics-based simulations are exploited for the extraction of behavioral models, such as the X-parameters, which are the ideal framework to translate TCAD simulations into Electronic Design Automation (EDA) tools suited for circuit-oriented analysis.

The thesis organization is hereafter reported. Chapter 2 is aimed at describing the semiconductor equations implemented in the in-house code, paying particularly attention to the temperature dependencies involved in the physical models. Chapter 3 provides a description of how the TCAD solver is implemented, giving details on discretization techniques and solution methods. Chapter 4 presents the efficient numerical implementation for the calculation of the so-called Green's functions and

explains how they are exploited for the sensitivity analysis. Chapter 5 shows the results of an efficient large-signal thermal variability analysis perfomed by the TCAD solver on a 54 nm Si FinFET power amplifier. Chapter 6 presents the electro-thermal compact modeling of the same device exploiting the X-parameter model. Chapter 7 exhibits the results of the DC and AC sensitivity analyses through the trap rate equation in an $0.150\ \mu$m AlGaN/GaN HEMT. Finally, in Chapter 8 some conclusions will be drawn.

Chapter 2

Physics-based thermal modeling and advanced features

2.1 Introduction

Physics-based device simulations represent an ideal environment to accurately model the behavior of an active device, especially in RF/microwave circuits, as they keep trace of the underlying technological and physical parameters. With the ever increasing capability of computation machines, the frequency domain analysis of electron devices operated in highly nonlinear conditions has proved to be a fairly manageable task even within TCAD simulators, especially in mixed-mode simulations, where the device physical equations need to be solved concurrently with an external embedding circuits.

This chapter is aimed at presenting the main semiconductor device equations included in an in-house, pre-existing two-dimensional (2D) physics-based simulator developed within the Microwave and Optoelectronic Group (MOG) of the Department of Electronics and Telecommunications (DET) of Politecnico di Torino. The solver basically consists of a 2D drift-diffusion code, including the Poisson equation, the continuity equations for electrons and holes, the trap rate equation and the external circuit equations. It allows not only for time-invariant and small-signal simulations, but also for large-signal multi-tone periodic and quasi-periodic analyses [19], which exploit the Harmonic Balance frequency domain technique and are typically performed in the scenario of RF/microwave devices.

The original version of the in-house semiconductor device simulator neglected temperature dependencies, which take place through a wide number of physical parameters and models, such as doping activation, mobility, diffusivity, thermal voltage, etc., and are especially relevant in the behavior of power devices, for instance GaAs or GaN based HEMTs, and nanoscale devices, such as FinFETs [20, 21]. The ideal choice to address this problem would be a self-consistent physics-based electro-thermal model, coupling the Fourier equation to the electrical device simulations, which however often represents a too demanding task for efficient and fast simulations. On the other hand, when the intrinsic device can be considered approximately isothermal at an equivalent lattice temperature T, electrical TCAD simulations varying T as a position-independent free parameter, allow to identify a T-dependent electrical device model. In the light of this consideration, the purpose of my work has been to realize a *temperature-dependent in-house solver* through the modification of already implemented physical models describing, for example, the doping-dependent mobility, the high-field mobility and the thermionic emission process, as well as the addition of new T-dependent physical models concerning the band gap, the electron affinity, the phonon-scattering mobility, etc. Moreover, the device heat dissipation process has been also accounted for in the implementation of the self-heating equation, which further enhances the in-house solver allowing for both parametric temperature variations and self-heating.

The treatment of temperature dependencies is not the only improvement of the original in-house solver, which has been further enriched through the optimization of pre-existing physical models and the introduction of new advanced models. With this aim, the refinement of the thermionic emission model, particularly useful for the simulation of possible conduction mechanisms characterizing heterojunction devices, has been carried out. Furthermore, despite the full ionization of dopants is a common practice in device modeling, it may introduce considerable errors in predicting the semiconductor device behavior, leading to the need of implementing from scratch the incomplete ionization model. Another key capability of the TCAD solver is the possibility to investigate trapping/de-trapping mechanisms in both static and dynamic conditions through the refinement of the trap rate equation, allowing the user to define different types of traps, each one with a certain concentration, energy level, lifetime and cross section. These advanced features make the TCAD solver very profitable for the simulation of heterostructure and/or nitride-based semiconductor devices. In conclusion, since the spontaneous and piezoelectric polarization charge

assume a central role in the behavior of III-V semiconductor devices, the polarization model has been implemented from scratch.

The following sections are focused on the physical description of all equations and models included in the in-house simulator. Details on implementation techniques will be provided in Chapter 3.

2.2 Poisson-drift-diffusion model

Semiconductor device simulation can be performed through the implementation of several approaches based on a semiclassical foundation such as the Maxwell's equations of electromagnetism and the Boltzmann transport equation (BTE). The most common simplified description of semiconductor device behavior is:

$$\nabla \cdot (\varepsilon \nabla \phi) = -\rho \tag{2.1a}$$

$$\frac{1}{q}\nabla \cdot \mathbf{J}_n = \frac{\partial n}{\partial t} + U_n \tag{2.1b}$$

$$-\frac{1}{q}\nabla \cdot \mathbf{J}_p = \frac{\partial p}{\partial t} + U_p \tag{2.1c}$$

This system of equations is based on the assumption that the effect of self-heating is neglected at present, therefore the lattice temperature T is considered uniform in the device and equal to the heat sink temperature T_0 (typically 300 K). This assumption can be relaxed, as described later on, coupling the system to an additional equation.

The Poisson equation (2.1a) depends on the electrical time-independent permittivity ε, the electrostatic potential ϕ, which is related to the electric field $\mathbf{E}$ in (2.2), and the space charge density ρ, expressed in (2.3). The space charge depends on the electron elementary charge q, the electron and hole charge concentrations n and p, the ionized donor and acceptor impurity densities N_D and N_A and the charge density due to the presence of traps or fixed charges ρ_F.

$$\mathbf{E} = -\nabla \phi \tag{2.2}$$

$$\rho = q \cdot (p - n + N_\mathrm{D} - N_\mathrm{A}) + \rho_\mathrm{F} \tag{2.3}$$

The electron and hole continuity equations (2.1b) and (2.1c) depend on the carrier conduction current densities $\mathbf{J}_n$ and $\mathbf{J}_p$, such that $\mathbf{J}_{\text{tot}} = \mathbf{J}_n + \mathbf{J}_p$, and the net recombination rates for each carrier U_n and U_p, expressed as the difference between the recombination rate R and the generation rate G. The carrier current densities depend on the average carrier velocities $\mathbf{v}_n$ and $\mathbf{v}_p$:

$$\mathbf{J}_n = -q\, n\, \mathbf{v}_n \quad \text{and} \quad \mathbf{J}_p = q\, p\, \mathbf{v}_p \tag{2.4}$$

They can be determined starting from the Boltzmann transport equation, which can be reduced, after mathematical manipulations and simplifications, to the following expressions:

$$\mathbf{J}_n = q\mu_n n\, \mathbf{E} + qD_n \nabla n = -q\mu_n n\, \nabla\phi + qD_n \nabla n \tag{2.5a}$$

$$\mathbf{J}_p = q\mu_p p\, \mathbf{E} - qD_p \nabla p = -q\mu_p p\, \nabla\phi - qD_p \nabla p \tag{2.5b}$$

where μ_n is the electron mobility, μ_p the hole mobility, D_n the electron diffusivity and D_p the hole diffusivity. System (2.1), together with the current relations (2.5), constitutes the Poisson-Drift-Diffusion system (PDD), first presented by Shockley [22] and VanRoosbroeck [23]. The PDD formulation is the most useful form for transport equations because it requires the solution of a single PDE for each carrier type thanks to the fact that (2.5) are not PDEs, rather a closed-form for the current. Therefore, the whole PDD model needs the solution of three PDEs if both electrons and holes are considered in the simulation.

The PDD current density equations are the sum of a *drift* contribution, where the motion of particles is induced by the electric field, and of a *diffusion* contribution, due to a gradient of the carriers concentration. At thermodynamic equilibrium the drift and diffusion components are equal and opposite, while out of equilibrium, carriers are subjected to an external driving force, giving a net current density different from zero. The drift involves the product between the electrical conductivity ($\sigma_n = q\mu_n n$ in (2.5a) and $\sigma_p = q\mu_p p$ in (2.5b)) and the electric field $\mathbf{E}$. The electrical conductivity depends on the concentrations n and p and the carrier mobilities μ_n and μ_p, which are expressed as follows:

$$\mu_n = \frac{q\tau_p}{m_{\text{eff},n}} \quad \text{and} \quad \mu_p = \frac{q\tau_p}{m_{\text{eff},p}} \tag{2.6}$$

where τ_p is the average momentum relaxation time, while $m_{\text{eff},n}$ and $m_{\text{eff},p}$ are the electron and hole effective masses, respectively. The diffusion term involves

the gradient of the carrier concentrations and the diffusivities D_n and D_p, whose expression is given by the Einstein relation:

$$D_n = \underbrace{\frac{k_B T}{q}}_{V_T} \mu_n = V_T \mu_n \quad \text{and} \quad D_p = \underbrace{\frac{k_B T}{q}}_{V_T} \mu_p = V_T \mu_p \tag{2.7}$$

where k_B is the Boltzmann constant, T the lattice temperature and V_T the thermal voltage. The Einstein relation links, at equilibrium or close to, the diffusion phenomenon, ruled by the diffusivity, to the drift phenomenon, represented by the mobility.

Hereafter, some important quantities involved in the PDD model are mentioned. In the Poisson equation (2.1a) the electrostatic potential is defined apart from a constant, hence it is possible to arbitrarily choose the reference potential. A typical choice is:

$$E_{Fi} = -q\phi \tag{2.8}$$

where E_{Fi} is the intrinsic Fermi level, that is the energy level such that the electron concentration at equilibrium is equal to the intrinsic concentration n_i. Concerning the continuity equations (2.1b) and (2.1c), at equilibrium electrons and holes are defined by the Shockley's equations:

$$n = n_i \exp\left(\frac{E_F - E_{Fi}}{k_B T}\right) \quad \text{and} \quad p = n_i \exp\left(\frac{E_{Fi} - E_F}{k_B T}\right) \tag{2.9}$$

where E_F is the Fermi level. Shockley's equations quantify the carrier distributions in a semiconductor which follow the Maxwell-Boltzmann statistics for a non-degenerate semiconductor. The carrier densities expressed in terms of Boltzmann statistics are:

$$n \simeq N_C \exp\left(\frac{E_F - E_C}{k_B T}\right) \tag{2.10a}$$

$$p \simeq N_V \exp\left(\frac{E_V - E_F}{k_B T}\right) \tag{2.10b}$$

where E_C and E_V are the conduction and valence band energies, while N_C and N_V are the conduction and valence band densities of states, which can be written as [24]:

$$N_C = 2\left[\frac{m_{\text{eff},n}\, k_B T}{2\pi\hbar^2}\right]^{\frac{3}{2}} \quad \text{and} \quad N_V = 2\left[\frac{m_{\text{eff},p}\, k_B T}{2\pi\hbar^2}\right]^{\frac{3}{2}} \tag{2.11}$$

where $\hbar$ is the reduced Planck constant. For degenerate semiconductors, the Boltzmann statistics no longer applies and carriers follow the Fermi-Dirac distribution [25]. A preliminary implementation of the Fermi-like in-house solver has been carried out, but not exploited in this thesis, hence not reported in the discussion. At thermodynamic equilibrium, for the Boltzmann statistics, the mass action law $np = n_i^2$ is valid. The intrinsic concentration reads:

$$n_i = \sqrt{N_C N_V}\exp\left(-\frac{E_g}{2k_B T}\right) \tag{2.12}$$

where $E_g = E_C - E_V$ is the energy gap of a semiconductor. Starting from (2.10a) and plugging in (2.12) and (2.8), one can write:

$$E_C = -q\phi + \frac{E_g}{2} + \frac{k_B T}{2}\ln\left(\frac{N_C}{N_V}\right) \quad \text{and} \quad E_V = E_C - E_g \tag{2.13}$$

An alternative formulation of the drift-diffusion transport equations exploits the concept of the quasi-Fermi levels E_{Fn} and E_{Fp}:

$$\mathbf{J}_n = \mu_n n\, \nabla E_{Fn} \tag{2.14a}$$

$$\mathbf{J}_p = \mu_p p\, \nabla E_{Fp} \tag{2.14b}$$

where E_{Fn} and E_{Fp} are obtained recalling the Boltzmann statistics:

$$n \simeq N_C \exp\left(\frac{E_{Fn} - E_C}{k_B T}\right) \Longrightarrow E_{Fn} = E_C + k_B T \ln\left(\frac{n}{N_C}\right) \tag{2.15a}$$

$$p \simeq N_V \exp\left(\frac{E_V - E_{Fp}}{k_B T}\right) \Longrightarrow E_{Fp} = E_V - k_B T \ln\left(\frac{p}{N_V}\right) \tag{2.15b}$$

Substituting (2.15) into (2.14), one finds (2.5).

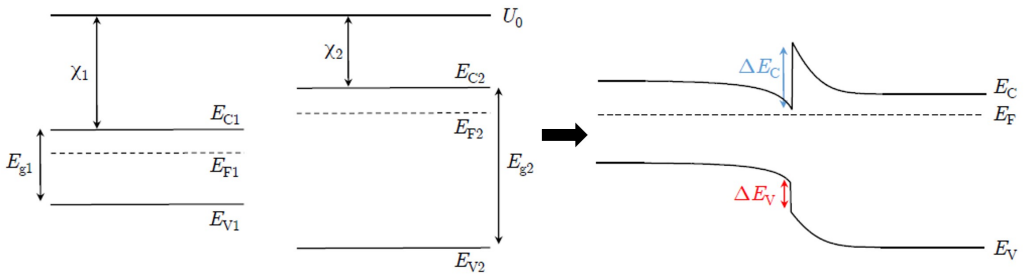

Fig. 2.1 Example of a typical heterojunction between two materials.

The final expression of the PDD system implemented in the in-house TCAD simulator is:

$$\begin{cases} \nabla \cdot (\varepsilon \nabla \phi) = -\rho = -q \cdot (p - n + N_{\mathrm{D}} - N_{\mathrm{A}}) - \rho_{\mathrm{F}} \\ \\ \dfrac{1}{q} \nabla \cdot \mathbf{J}_n = \dfrac{\partial n}{\partial t} + U_n \quad \text{with} \quad \mathbf{J}_n = -q\mu_n n \, \nabla \phi + q D_n \nabla n \\ \\ -\dfrac{1}{q} \nabla \cdot \mathbf{J}_p = \dfrac{\partial p}{\partial t} + U_p \quad \text{with} \quad \mathbf{J}_p = -q\mu_p p \, \nabla \phi - q D_p \nabla p \end{cases} \tag{2.16}$$

2.2.1 Treatment of heterostructures

The PDD model and all the related expressions are only valid in homostructures, where there is a uniform material composition along the device, which can be characterized by a different type of doping. Heterostructure devices include more than one material and, since they are characterized by different physical properties, they produce discontinuities in the band diagram. Let us consider a typical heterostructure example, shown in Fig. 2.1, where it can be noticed that the conduction and valence band discontinuities are related to different values of bandgap and affinity between the two materials. At the interface between material 1 and material 2, the conduction band discontinuity is given by the *affinity rule*:

$$\Delta E_{\mathrm{C},21} = E_{\mathrm{C}2} - E_{\mathrm{C}1} = (U_0 - \chi_2) - (U_0 - \chi_1) = \chi_1 - \chi_2 \tag{2.17}$$

where U_0 is the vacuum energy level and χ the electron affinity. Due to the energy

band discontinuities, (2.13) can be modified in the following way:

$$E_{\mathrm{C}} = -q\phi + \underbrace{\frac{E_{\mathrm{g}}}{2} + \frac{k_{\mathrm{B}}T}{2}\ln\left(\frac{N_{\mathrm{C}}}{N_{\mathrm{V}}}\right) + \theta_{\mathrm{C}}}_{\Delta E_{\mathrm{C}}} \tag{2.18a}$$

$$E_{\mathrm{V}} = E_{\mathrm{C}} - E_{\mathrm{g}} = -q\phi + \underbrace{\Delta E_{\mathrm{C}} - E_{\mathrm{g}}}_{\Delta E_{\mathrm{V}}} \tag{2.18b}$$

where θ_{C} is defined as:

$$\theta_{\mathrm{C}} = q\phi_{\mathrm{r}} - q\phi_{\mathrm{r,const}} \tag{2.19}$$

The term ϕ_{r} is the *reference potential* of (2.20), calculated from the vacuum level, while the term $\phi_{\mathrm{r,const}}$ is the so-called *constant reference potential* and can be obtained evaluating ϕ_{r} in a *reference material*. Typically, the reference material is the one with the smallest bandgap, for example in a single heterojunction AlGaAs/GaAs, $\phi_{\mathrm{r,const}} = \phi_{\mathrm{r}}(\mathrm{GaAs})$.

$$q\phi_{\mathrm{r}} = -q\chi - \frac{E_{\mathrm{g}}}{2} - \frac{k_{\mathrm{B}}T}{2}\ln\left(\frac{N_{\mathrm{C}}}{N_{\mathrm{V}}}\right) \tag{2.20}$$

Plugging (2.18) into (2.15), quasi-Fermi levels can be re-written as:

$$E_{\mathrm{F}n} = -q\phi + \Delta E_{\mathrm{C}} + k_{\mathrm{B}}T\ln\left(\frac{n}{N_{\mathrm{C}}}\right) \tag{2.21a}$$

$$E_{\mathrm{F}p} = -q\phi + \Delta E_{\mathrm{V}} - k_{\mathrm{B}}T\ln\left(\frac{p}{N_{\mathrm{V}}}\right) \tag{2.21b}$$

Finally, (2.21) can be plugged into (2.14), leading to:

$$\begin{aligned}\mathbf{J}_n = n\mu_n\nabla E_{\mathrm{F}n} &= qD_n\nabla n - qn\mu_n\nabla\left[\phi \underbrace{-\frac{\Delta E_{\mathrm{C}}}{q} + V_{\mathrm{T}}\ln(N_{\mathrm{C}})}_{\phi_{\mathrm{het},n}}\right] \\ &= qD_n\nabla n - qn\mu_n\nabla(\phi + \phi_{\mathrm{het},n})\end{aligned} \tag{2.22a}$$

$$\mathbf{J}_p = p\mu_p \nabla E_{\mathrm{F}p} = -qD_p \nabla p - qp\mu_p \nabla \left[\phi \underbrace{-\frac{\Delta E_{\mathrm{V}}}{q} - V_{\mathrm{T}} \ln(N_{\mathrm{V}})}_{\phi_{\mathrm{het},p}} \right]$$
$$= -qD_p \nabla p - qp\mu_p \nabla(\phi + \phi_{\mathrm{het},p}) \tag{2.22b}$$

2.2.2 Boundary conditions

The basic semiconductor equations are correctly solved in order to simulate the device behavior, only once appropriate boundary conditions are defined in some specific device regions. Each device is characterized by electrical contacts, needed to bias it or, mathematically speaking, essential to make the problem well-posed. As a consequence, the boundary conditions are enforced on the electrical contacts, which can be of different types [26].

Ohmic contacts

Ohmics contacts require to enforce the charge neutrality, hence for the Boltzmann statistics, one can obtain:

$$\phi = v_k + \frac{k_{\mathrm{B}}T}{q} \operatorname{asinh}\left(\frac{N_{\mathrm{D}} - N_{\mathrm{A}}}{2n_i} \right) \tag{2.23}$$

$$\begin{aligned} n_0 &= \sqrt{\frac{(N_{\mathrm{D}} - N_{\mathrm{A}})^2}{4} + n_i^2} + \frac{N_{\mathrm{D}} - N_{\mathrm{A}}}{2} \\ p_0 &= \sqrt{\frac{(N_{\mathrm{D}} - N_{\mathrm{A}})^2}{4} + n_i^2} - \frac{N_{\mathrm{D}} - N_{\mathrm{A}}}{2} \end{aligned} \tag{2.24}$$

with the assumption of full ionization of dopants (see later the incomplete ionization model). Moreover, the terms n_0 and p_0 are the electron and hole concentrations at equilibrium, while v_k is the voltage applied to the k-th contact.

Contacts on insulator

If the contact is put on an insulator (like the gate contact of MOSFET devices), different boundary conditions are applied:

$$\phi = v_k - \phi_{\mathrm{MS}} \tag{2.25}$$

$$n_0 = p_0 = 0 \tag{2.26}$$

where ϕ_{MS} is the workfunction difference between the contact metal and the semiconductor. Notice that if an ohmic contact touches both a semiconductor and an insulator, the potential is discontinuous and (2.23) prevails over (2.25).

Schottky contacts

For the Schottky contact, like the gate of an HEMT structure, there is the following boundary condition:

$$\phi = v_k - \phi_{\mathrm{B}} + \frac{k_{\mathrm{B}}T}{q}\ln\left(\frac{N_{\mathrm{C}}}{n_i}\right) \tag{2.27}$$

$$\mathbf{J}_n \cdot \mathbf{n} = q v_{\mathrm{th}}^n (n - n_0^{\mathrm{B}}) \quad \text{and} \quad \mathbf{J}_p \cdot \mathbf{n} = -q v_{\mathrm{th}}^p (p - p_0^{\mathrm{B}}) \tag{2.28}$$

where ϕ_{B} is the Schottky barrier, i.e. the difference between the metal workfunction and the semiconductor electron affinity, if the semiconductor is n-doped, or the difference between the band gap and the barrier, if the semiconductor is p-doped. Moreover, v_{th}^n and v_{th}^p are the thermionic emission velocities, while n_0^{B} and p_0^{B} are the equilibrium concentrations, characterized by the following expression:

$$n_0^{\mathrm{B}} = N_{\mathrm{C}} \exp\left(\frac{-q\phi_{\mathrm{B}}}{k_{\mathrm{B}}T}\right) \quad \text{and} \quad p_0^{\mathrm{B}} = N_{\mathrm{V}} \exp\left(\frac{-E_{\mathrm{g}} + q\phi_{\mathrm{B}}}{k_{\mathrm{B}}T}\right) \tag{2.29}$$

2.3 External circuit equations for RF circuit modeling

Consider the typical microwave circuit of Fig. 2.2: the *non-linear* part is characterized by the device physical equations, e.g. the PDD model, while the *linear* part consists of a set of equations relating currents and voltages to the ports connecting the two sections, e.g. the passive circuit implementing the matching network of Fig.

2.2. The in-house TCAD solver gives the possibility to couple the physics-based model to External Circuit Equations (ECEs), describing the electrical network in which the device is embedded. This leads to the so-called *mixed-mode simulations*, where the solution of the PDD model is directly embedded into the solution of the ECEs. In this way active devices can be described in terms of physical quantities, such as electrostatic potential, carrier concentration, etc., but also in terms of their performances into an electrical circuit. This has a great importance in the scenario of power devices, such as HEMTs, HBTs or MOSFETs, which need the accuracy of physics-based simulations and thus, can not be handled by pure compact models. The in-house simulator was originally limited to the analysis of circuits including a single device, but starting from [27], it has been extended to circuits with multiple interacting devices, for example the Doherty power amplifier which is one of the most promising circuits for the development of high efficiency power amplifiers.

The resulting PDD-ECE system might be solved in the time domain, where voltages and currents are expressed as a function of time, or in the frequency domain, where the same quantities are expressed in terms of harmonic components, exploiting the Fourier transform. Time-domain simulations are very time consuming and particularly critical, since they need to integrate equations until the onset of the steady-state regime. This point may be reached after a great number of time steps and increases the computational burden of the simulation. On the contrary, frequency-domain approaches are preferred for the analysis of the steady-state periodic and quasi-periodic regime, since they are easier and more efficient in terms of computational cost and numerical stability. One of the most used frequency-domain techniques is the *Harmonic Balance* (HB) method [28], originally developed for non-linear circuit analysis and then, extended to physics-based device analysis in [29]. The HB formalism, reviewed in Appendix A, is exploited in the in-house TCAD solver in order to solve, directly in the frequency domain, the PDD-ECE system, whose HB numerical implementation will be explained in Chapter 3.

Purpose of this section is simply to introduce the circuit equations of the external electrical network, already implemented in the original version of the in-house solver, directly in a frequency-domain notation. Consider the the schematic representation of the active device coupled to the external electrical network, as shown in Fig. 2.3: the involved unknowns are the vectors of voltages and currents, namely respectively $\mathbf{v}$ and $\mathbf{i}$, defined at each device terminal $k = (1, 2, \ldots, K)$, where K is the total number

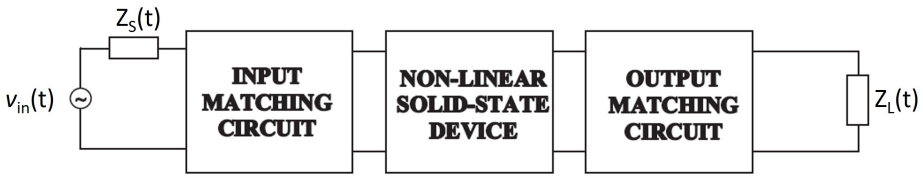

Fig. 2.2 Schematic representation of a mixed-mode configuration characterized by solide-state device connected to the input and output matching network.

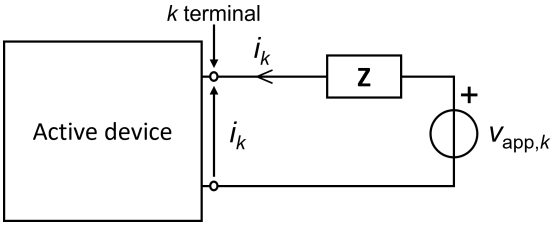

Fig. 2.3 Schematic of the outer electrical network coupled to the active device in a mixed-mode simulation.

of terminals:

$$\mathbf{v} = (v_1, v_2, \ldots, v_K) \tag{2.30a}$$

$$\mathbf{i} = (i_1, i_2, \ldots, i_K) \tag{2.30b}$$

The first ECE is the *voltage-controlled equation*:

$$\mathbf{v} + \mathbf{Z}\,\mathbf{i} = \mathbf{v}_{\text{app}} \tag{2.31}$$

where $\mathbf{Z}$ is the circuit impedance matrix, in the phasor domain, with size $K \times K$:

$$\mathbf{Z} = \begin{pmatrix} Z_{11} & \ldots & Z_{1K} \\ \vdots & \ddots & \vdots \\ Z_{K1} & \ldots & Z_{KK} \end{pmatrix} \tag{2.32}$$

The second external circuit expression is the *current equation*:

$$\mathbf{i} = \int_A (\mathbf{J}_n + \mathbf{J}_p + \mathbf{J}_{\text{D}})\, \mathrm{d}A \tag{2.33}$$

where A is the area of the terminal contact, while $\mathbf{J}_n$, $\mathbf{J}_p$ and $\mathbf{J}_{\text{D}}$ are the electron, hole and displacement current, respectively. The displacement contribution arises in

dynamic conditions only and its derivation comes from the Maxwell's equations:

$$\mathbf{J}_{\mathrm{D}} = \frac{\partial \mathbf{D}}{\partial t} = \varepsilon \frac{\partial \mathbf{E}}{\partial t} \tag{2.34}$$

where $\mathbf{D}$ is the displacement vector, ε the permittivity and $\mathbf{E}$ the electric field.

The final PDD-ECE system is represented as follows:

$$\begin{cases} \nabla \cdot (\varepsilon \nabla \phi) = -q \cdot (p - n + N_{\mathrm{D}} - N_{\mathrm{A}}) - \rho_{\mathrm{F}} \\ \\ \dfrac{1}{q} \nabla \cdot \mathbf{J}_n = \dfrac{\partial n}{\partial t} + U_n \quad \text{with} \quad \mathbf{J}_n = -q\mu_n n \, \nabla \phi + q D_n \nabla n \\ \\ -\dfrac{1}{q} \nabla \cdot \mathbf{J}_p = \dfrac{\partial p}{\partial t} + U_p \quad \text{with} \quad \mathbf{J}_p = -q\mu_p p \, \nabla \phi - q D_p \nabla p \\ \\ \mathbf{v} + \mathbf{Z}\,\mathbf{i} = \mathbf{v}_{\mathrm{app}} \\ \\ \mathbf{i} = \int_A (\mathbf{J}_n + \mathbf{J}_p + \mathbf{J}_{\mathrm{D}}) \, \mathrm{d}A \end{cases} \tag{2.35}$$

2.4 Modeling of frequency dispersion phenomena

Frequency dispersion phenomena have a significant impact on the behavior and performance of active devices, especially in analog RF and microwave applications. One of the main dispersion mechanism is related to the thermal management, which is becoming more and more important due to the shrinking of device dimension, the worsening of the environmental conditions in which they operate and the deployment of non-planar structures, as explained in Chapter 1. Another important dispersion phenomena is related to trapping and de-trapping mechanisms occurring in III-V semiconductors or in oxide materials. Nowadays, the investigation of trap signatures has a central role in order to achieve good RF performances and an adequate device reliability, especially if the combined effect of temperature and traps is considered in the same structure.

The in-house simulator provides advanced capabilities to evaluate the influence of both frequency dispersion effects on device performance. In fact, it allows to

couple the PDD model to the Self-Heating (SH) equation for the prediction of dynamic thermal effects and the Trap Rate Equation (TRE) for the investigation of frequency-dependent trapping mechanisms. The SH equation was not present in the original version of the TCAD solver, hence it has been implemented from scratch. On the other hand, the TRE was partially available, hence its implementation has been improved allowing the user to define different trap types with a certain concentration and energy level.

2.4.1 Self-heating equation

The effect of self-heating can be analyzed from different points of view. At the microscopic level, carriers transfer a certain amount of energy to the lattice producing vibrations, i.e. acoustic and optical phonons. The more the number of phonons, the more the scattering process with carriers, whose kinetic energy increases the dissipated power and fuels self-heating. At the macroscopic level, the dissipated power is translated into heat, leading to a local temperature rise: the temperature increase depends on the thermal resistance and heat capacitance associated to the device and the surrounding materials, moreover it can be uniform or non-uniform, producing in this case hot-spots inside the device [30]. Since the lattice temperature enters essentially the analytical formulation of every physical model parameter, such as energy gap, electron affinity, carrier mobility, etc., the temperature increase aggressively degrades the active device performances, in both static and dynamic conditions, and needs to be accounted for. To this aim, the Self-Heating (SH) equation has been implemented in the in-house simulator: the PDD-ECE system is self-consistently solved with the SH equation, forming the Self-Heating System (SHS). This point represents a great advantage for the in-house solver, in fact TCAD commercial simulators also give the possibility to account for the temperature increase, but with some limitations. For instance, Synopsys TCAD Sentaurus implements a self-heating model, restricted to static conditions only, able to calculate uniform temperature variations by post-processing rather than self-consistently compute it with all other solution variables.

In the PDD model, the device lattice temperature T is considered as a uniform parameter throughout the device and equal to the heat sink temperature T_0 (typically 300 K), as shown in the schematic of Fig. 2.4. If T_0 is varied to a certain value, such as 305 K, 320 K, 350 K, etc., the T parameter and all the temperature-dependent

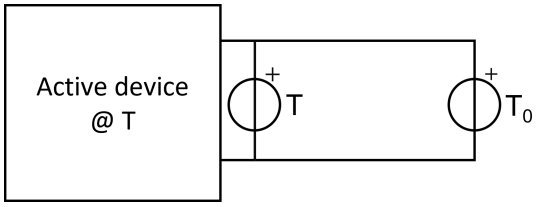

Fig. 2.4 Schematic of the active device in absence of a thermal impedance.

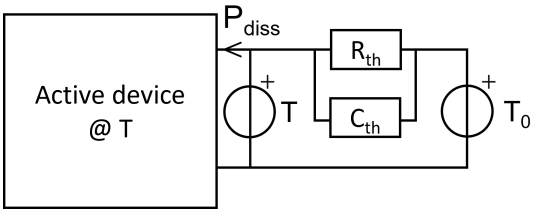

Fig. 2.5 Schematic of the active device coupled to a thermal impedance.

physical quantities involved in the PDD model, such as mobility, diffusivity, velocity saturation, etc., will follow that temperature variation. Therefore, this model is able to predict the effect of parametric variations of the device temperature, avoiding however a direct evaluation of device self-heating. If the effect of self-heating is accounted for, the device is considered coupled to an external lumped thermal impedance Z_{th} through which heat is dissipated towards a heat sink at temperature T_0, as shown in Fig. 2.5. According to the classical theory for linear thermal behavior [31], the temperature increase can be calculated in the frequency domain by the so-called thermal impedance, akin to the electrical impedance. The formulation in the frequency domain exploits phasors to represent the Fourier transform of both temperature and dissipated power:

$$\Delta T = T - T_0 = Z_{\text{th}}\, P_{\text{diss}} \tag{2.36}$$

where T is the final temperature of the device and a new unknown of the problem, T_0 is the heat sink temperature and P_{diss} is the Fourier transform of the dissipated power. The time-dependent expression of the dissipated power is given by the instantaneous product of terminal voltages $v_{0,k}(t)$ and currents $i_k(t)$:

$$p_{\text{diss}}(t) = \sum_k i_k(t) v_{0,k}(t) \tag{2.37}$$

The term Z_{th} corresponds to the thermal impedance, expressed in the phasor domain and given by the parallel between a thermal resistance R_{th} and a thermal capacitance C_{th}. This equation provides an increase of the lattice temperature and, consequently, a uniform device self-heating.

The final SHS system implemented in the TCAD solver is:

$$\begin{cases} \nabla \cdot (\varepsilon \nabla \phi) = -q \cdot (p - n + N_{\mathrm{D}} - N_{\mathrm{A}}) - \rho_{\mathrm{F}} \\ \\ \dfrac{1}{q} \nabla \cdot \mathbf{J}_n = \dfrac{\partial n}{\partial t} + U_n \quad \text{with} \quad \mathbf{J}_n = -q\mu_n n \, \nabla \phi + q D_n \nabla n \\ \\ -\dfrac{1}{q} \nabla \cdot \mathbf{J}_p = \dfrac{\partial p}{\partial t} + U_p \quad \text{with} \quad \mathbf{J}_p = -q\mu_p p \, \nabla \phi - q D_p \nabla p \\ \\ \mathbf{v} + \mathbf{Z}\,\mathbf{i} = \mathbf{v}_{\mathrm{app}} \\ \\ \Delta T = T - T_0 = Z_{\mathrm{th}} \, P_{\mathrm{diss}} \\ \\ \mathbf{i} = \int_A (\mathbf{J}_n + \mathbf{J}_p + \mathbf{J}_{\mathrm{D}}) \, \mathrm{d}A \end{cases} \tag{2.38}$$

2.4.2 Trap rate equation

III-V semiconductors, such as GaN, AlN and relative alloys, have an evergrowing importance thanks to their superior characteristics with respect to more conventional materials, such as wide band gap, high electron mobility, high saturation velocity and high breakdown field. On the other hand, they are characterized by a high cost due to the presence of non-intentional doping and the development of dislocations layers, which may worsen their electrical and optical properties [18]. The deployment of nitride-based semiconductors finds a match in HEMT devices: in the last years several technological improvements have enabled GaN-based HEMT structures to achieve a great relevance in high-power and high-frequency applications. Examples can be the development of appropriate substrate materials [32], the improvement of the material quality of epitaxial and passivation layers [33, 34], the use of field plates [35], the optimization of some geometrical parameters, such as the barrier thickness, the addition of a GaN cap layer, the reduction of the gate length [36]. Another goal has been the reduction of short-channel effects which strongly affect nanoscale devices: one way to reduce them in GaN HEMTs is to make the GaN buffer layer semi-insulating through intrinsic defects or extrinsic deep-level dopants, such as Iron or Carbon [37]. Nonetheless, the superior performances of nitride-based

HEMT devices are still degraded by trapping and de-trapping mechanisms due to deep-level traps, which are present in the buffer layer, in the barrier or at the surface [6].

Traps are mainly due to material defects, dislocations, lattice mismatch between two materials or the presence of impurities in the crystal. These defects/dislocations create a localized trap at a certain energy level inside the material bandgap. There are mainly two different types of traps: a donor-like trap is considered neutral if occupied by an electron and positive if empty, while an acceptor-like trap is neutral if empty and negative if occupied by an electron. The different trapping mechanisms, whose nature is not yet entirely clear, and traps localization inside the device have a key role to determine RF performances and device reliability. In particular, traps are responsible of the drain current collapse and the degradation of the dynamic device performance, for example the low-frequency dispersion phenomenon characterizing Y-parameters [6]. With the aim of optimizing the GaN-based HEMT device performance, the in-house simulator implements the trap rate equation, coupled to the PDD-ECE model, leading to the PDD-ECE-TRE system. This represents another key advantage of the in-house TCAD solver with respect to commercial simulators: for example, Synopsys TCAD Sentaurus is a flexible platform to compute the occupied trap concentration with different spatial distributions and energy levels, but with some limitations in frequency domain simulations.

The trap occupation probability in non-equilibrium conditions is:

$$\frac{\partial f^n}{\partial t} = \sum_i r_i^n \qquad \text{where} \qquad r_i^n = (1-f^n)c_i^n - f^n e_i^n \tag{2.39}$$

where f^n is the electron occupation, which is a number between 0 and 1, while c_i^n is the capture rate of an empty trap and e_i^n is the emission rate of a full trap. The index i refers to a capture or an emission process from the conduction or valence band, therefore the sum is over all capture and emission processes:

$$\frac{\partial f^n}{\partial t} = (1-f^n)c_{\mathrm{C}}^n - f^n e_{\mathrm{C}}^n + (1-f^n)e_{\mathrm{V}}^p - f^n c_{\mathrm{V}}^p \tag{2.40}$$

where c_{C}^n and e_{C}^n are expressed in the *electron picture*, while c_{V}^p and e_{V}^p in the *hole picture*, knowing that the capture and emission of an electron correspond,

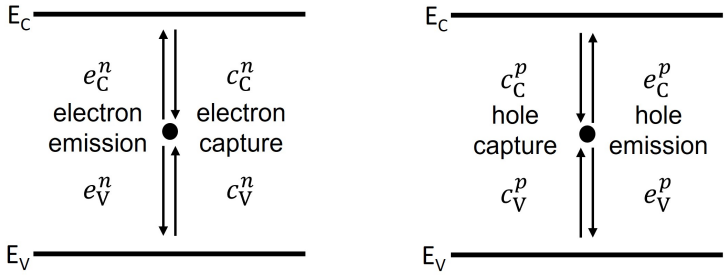

Fig. 2.6 Electron picture (left) and hole picture (right).

respectively, to the emission and capture of a hole (see Fig. 2.6):

$$c_i^n = e_i^p \qquad \text{and} \qquad e_i^n = c_i^p \tag{2.41}$$

In (2.40), one can distinguish four possible events (see Fig. 2.7):

a. The capture of an electron by an empty trap from the conduction band:

$$c_{\mathrm{C}}^n = \sigma_n v_{\mathrm{th}}^n n$$

b. The emission of an electron from the trap to the conduction band:

$$e_{\mathrm{C}}^n = \sigma_n v_{\mathrm{th}}^n n_1$$

c. The capture of a hole by an occupied trap from the valence band:

$$c_{\mathrm{V}}^p = \sigma_p v_{\mathrm{th}}^p p$$

d. The emission of a hole from the empty trap to the valence band:

$$e_{\mathrm{V}}^p = \sigma_p v_{\mathrm{th}}^p p_1$$

where σ_n and σ_p are the trap cross sections, v_{th}^n and v_{th}^p the thermal velocities, while $n_1 = N_{\mathrm{C}} \exp[(E_{\mathrm{t}} - E_{\mathrm{C}})/k_{\mathrm{B}}T]$ and $p_1 = N_{\mathrm{V}} \exp[(E_{\mathrm{V}} - E_{\mathrm{t}})/k_{\mathrm{B}}T]$, where E_{t} is the trap energy level. In the TCAD solver the equation is implemented expressing f^n as the

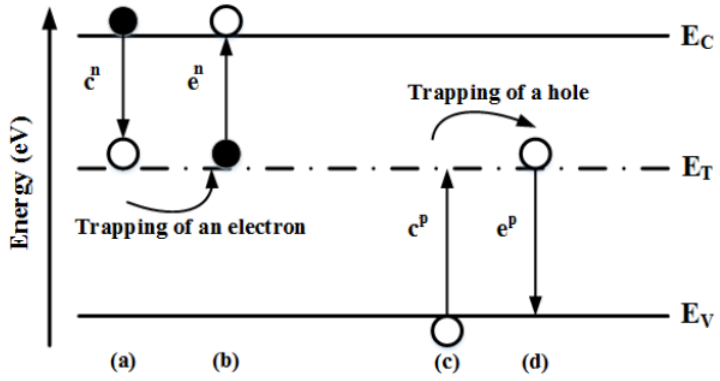

Fig. 2.7 Electron and hole capture/emission processes [6].

ratio between the number of occupied traps n_t and the number of total traps N_t:

$$\begin{aligned}\frac{\partial n_\mathrm{t}}{\partial t} &= \underbrace{N_\mathrm{t}\left(1-\frac{n_\mathrm{t}}{N_\mathrm{t}}\right)c_\mathrm{C}^n}_{R_n} - \underbrace{N_\mathrm{t}\frac{n_\mathrm{t}}{N_\mathrm{t}}e_\mathrm{C}^n}_{G_n} - \left[\underbrace{N_\mathrm{t}\frac{n_\mathrm{t}}{N_\mathrm{t}}c_\mathrm{V}^p}_{R_p} - \underbrace{N_\mathrm{t}\left(1-\frac{n_\mathrm{t}}{N_\mathrm{t}}\right)e_\mathrm{V}^p}_{G_p}\right] \\ &= \underbrace{R_n - G_n}_{U_n} - \underbrace{(R_p - G_p)}_{U_p} = U_n - U_p\end{aligned} \tag{2.42}$$

where $G_{n,p}$ and $R_{n,p}$ are respectively the generation and recombination rates, while $U_{n,p}$ is the net recombination rate. In static steady-state conditions, the TRE is uncoupled from the PDD system, since the number of occupied traps is given by (2.43), which corresponds to the SRH recombination model.

$$\frac{\partial n_\mathrm{t}}{\partial t} = 0 \Longrightarrow n_\mathrm{t} = N_\mathrm{t}\left(\frac{c_\mathrm{C}^n + e_\mathrm{V}^p}{c_\mathrm{C}^n + e_\mathrm{C}^n + c_\mathrm{V}^p + e_\mathrm{V}^p}\right) \tag{2.43}$$

In dynamic conditions, the TRE needs to be solved consistently with the PDD-ECE model. First of all, the concentration of occupied traps n_t must be included in the space charge density and recalling (2.3), one can write:

$$\rho_F = -qn_\mathrm{t} \tag{2.44}$$

Hence, the Poisson equation is modified:

$$\nabla\cdot(\varepsilon\nabla\phi) = -q\cdot(p - n + N_\mathrm{D} - N_\mathrm{A} - n_\mathrm{t}) \tag{2.45}$$

Moreover, the electron and hole recombination rates $U_{n,p}$ are also included in the continuity equations (2.1b) and (2.1c).

The final PDD-ECE-TRE system implemented in the TCAD solver is:

$$\begin{cases} \nabla \cdot (\varepsilon \nabla \phi) = -q \cdot (p - n + N_{\mathrm{D}} - N_{\mathrm{A}} - n_{\mathrm{t}}) \\ \\ \dfrac{1}{q} \nabla \cdot \mathbf{J}_n = \dfrac{\partial n}{\partial t} + U_n \quad \text{with} \quad \mathbf{J}_n = -q\mu_n n \, \nabla \phi + q D_n \nabla n \\ \\ -\dfrac{1}{q} \nabla \cdot \mathbf{J}_p = \dfrac{\partial p}{\partial t} + U_p \quad \text{with} \quad \mathbf{J}_p = -q\mu_p p \, \nabla \phi - q D_p \nabla p \\ \\ \dfrac{\partial n_{\mathrm{t}}}{\partial t} = U_n - U_p \\ \\ \mathbf{v} + \mathbf{Z}\,\mathbf{i} = \mathbf{v}_{\mathrm{app}} \\ \\ \mathbf{i} = \int_A (\mathbf{J}_n + \mathbf{J}_p + \mathbf{J}_{\mathrm{D}}) \, \mathrm{d}A \end{cases} \tag{2.46}$$

A subcategory of traps is represented by the *fixed charges*, corresponding to traps always completely occupied and, as a consequence, equal to the total concentration N_{t}. In this case, the TRE is not coupled to the PDD-ECE system and only the space charge density of the Poisson equation is modified:

$$\rho_{\mathrm{F}} = -q n_{\mathrm{t}} = -q N_{\mathrm{t}} \tag{2.47}$$

2.5 Semiconductor physical models

In order to solve the PDD model, all the physical parameters involved in the system of PDEs, such as bandgap, electron affinity, density of states, mobility, etc, need to be defined through a specific temperature-dependent model which determines their behavior [26]. As shown in the following sections, each model involves a set of coefficients depending on the selected material. The in-house simulator supports a

library of semiconductor materials, including Si, GaAs, AlGaAs, Ge, InP, InGaAsP, InGaAs, AlGaAs, GaN, AlGaN.

2.5.1 Band structure parameters

The band structure represents the most fundamental property of a semiconductor. Realistic band structures are very complex, but in this work they are reduced to bandgap and electron affinity, whose T-dependent models have been implemented in the in-house code from scratch. The bandgap model is expressed as follow: [38]:

$$E_{\mathrm{g}}(T) = E_{\mathrm{g}}(0) - \frac{\alpha T^2}{T+\beta} \tag{2.48}$$

where $E_{\mathrm{g}}(0)$ is the bandgap energy at 0 K, while α and β are coefficients depending on the material. For each material $E_{\mathrm{g}}(0) = E_{g,0} - \delta E_{g,0}$, where $E_{g,0}$ and $\delta E_{g,0}$ are adjustable parameters: the first one is fixed, while the second one depends on the chosen bandgap model. The one considered in this work is the Bennet model, for which $\delta E_{g,0}$ is a constant equal to zero by default.

The electron affinity is the difference between the conduction band energy and the vacuum level and shows the following temperature-dependence:

$$\chi(T) = \chi_0 - \frac{\alpha T^2}{2(T+\beta)} \tag{2.49}$$

where χ_0 is an adjustable parameter depending on the material. Actually, $\chi(T)$ also depends on an additional quantity due to the bandgap narrowing, which is neglected in this treatment.

2.5.2 Incomplete ionization model

Dopants are not always fully ionized at room temperature: if the impurity level is sufficiently shallow the ionization is complete, otherwise incomplete ionization should be considered. The incomplete ionization phenomenon is described by one

of the new-entry models of the in-house solver and takes the following expression:

$$N_{\mathrm{D}} = \frac{N_{\mathrm{D},0}}{1 + g_{\mathrm{D}} \dfrac{n}{n_1}} \quad \text{where} \quad n_1 = N_{\mathrm{C}} \exp\left(-\frac{\Delta E_{\mathrm{D}}}{k_{\mathrm{B}} T} \right) \tag{2.50a}$$

$$N_{\mathrm{A}} = \frac{N_{\mathrm{A},0}}{1 + g_{\mathrm{A}} \dfrac{p}{p_1}} \quad \text{where} \quad p_1 = N_{\mathrm{V}} \exp\left(-\frac{\Delta E_{\mathrm{A}}}{k_{\mathrm{B}} T} \right) \tag{2.50b}$$

where $N_{\mathrm{D},0}$ and $N_{\mathrm{A},0}$ are the donor and acceptor concentration, g_{D} and g_{A} are the degeneracy factors, while $\Delta E_{\mathrm{D}} = E_{\mathrm{C}} - E_{\mathrm{D}}$ and $\Delta E_{\mathrm{A}} = E_{\mathrm{A}} - E_{\mathrm{V}}$ are the energy differences defined by the donor and acceptor ionization activation energies, respectively E_{D} and E_{A}. The expressions for n_1 and p_1 are valid for the Boltzmann statistics.

2.5.3 Mobility models

The drift-diffusion model involves the mobility of electrons and holes through the diffusivity terms D_n and D_p. As shown in (2.6) the mobility is related to the average momentum relaxation time τ_p, which accounts for different scattering mechanisms: phonon scattering due to thermal vibrations, impurity scattering and scattering related to the electric field. The first one is described by the *constant mobility model*, implemented from scratch in the TCAD solver, the last two phenomena are outlined, respectively, by the *doping dependence model* and *high-field saturation model*, whose implementation was already present in the in-house code without the treatment of temperature dependencies.

Constant mobility model

In lightly doped semiconductors, the constant mobility model relates the mobility of electrons and holes to the lattice temperature [39]:

$$\mu_{\mathrm{const}} = \mu_{\mathrm{L}} \left(\frac{T}{300\ \mathrm{K}} \right)^{-\zeta} \tag{2.51}$$

where μ_{L} is the mobility due to bulk phonon scattering. Both μ_{L} and ζ depends on the material, for example for silicon they assume the values in Table 2.1.

Table 2.1 Constant mobility parameters for silicon.

Symbol	Electrons	Holes	Unit
μ_{L}	1417	470.5	$\mathrm{cm}^2/\mathrm{Vs}$
ζ	2.5	2.2	1

Table 2.2 Silicon coefficients for Masetti model

Symbol	Electrons	Holes	Unit
μ_{min1}	52.2	44.9	$\mathrm{cm}^2/\mathrm{Vs}$
μ_{min2}	52.2	0	1
μ_1	43.4	29	$\mathrm{cm}^2/\mathrm{Vs}$
P_{c}	0	$9.23{\cdot}10^{16}$	cm^{-3}
C_{r}	$9.68{\cdot}10^{16}$	$2.23{\cdot}10^{17}$	cm^{-3}
C_{s}	$3.43{\cdot}10^{20}$	$6.10{\cdot}10^{20}$	cm^{-3}
α	0.68	0.719	1
β	2	2	1

.

Doping dependence model

In a doped semiconductor, carrier mobility is degraded by the carrier scattering with charged impurity ions. Depending on the material, the in-house TCAD solver exploits different models: the *Masetti model* and the *Arora model*.

The *Masetti model* [7] describes the mobility behavior as a function of doping concentration and constant mobility:

$$\mu_{\mathrm{dop}} = \mu_{\mathrm{min1}} \exp\left(\frac{-P_{\mathrm{c}}}{N_{\mathrm{A},0}+N_{\mathrm{D},0}}\right) + \frac{\mu_{\mathrm{const}}-\mu_{\mathrm{min2}}}{1+\left(\frac{N_{\mathrm{A},0}+N_{\mathrm{D},0}}{C_{\mathrm{r}}}\right)^{\alpha}} - \frac{\mu_1}{1+\left(\frac{C_{\mathrm{s}}}{N_{\mathrm{A},0}+N_{\mathrm{D},0}}\right)^{\beta}} \tag{2.52}$$

where μ_{min1}, μ_{min2} and μ_1 are the reference mobilities, while P_{c}, C_{r} and C_{s} are the reference doping concentrations. All these parameters, including the exponents α and β depend on the material. Table 2.2 reports the values used in the TCAD solver for silicon, as an example. Moreover, Fig. 2.8 shows a comparison between the hole mobility of a boron-doped silicon calculated through the analytical formula (2.52) and the same quantity experimentally obtained.

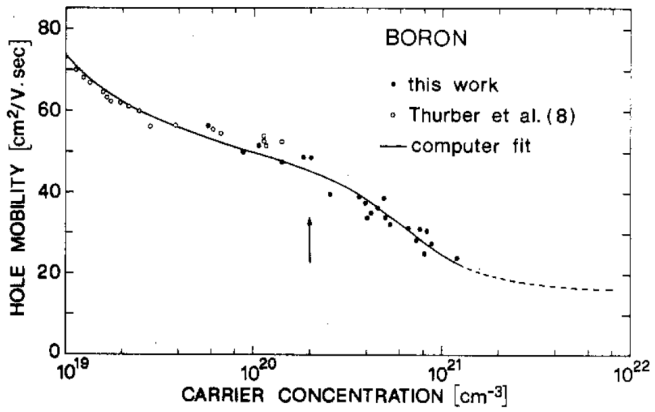

Fig. 2.8 Hole mobility in boron-doped silicon [7]. Solid line: computer fit obtained with (2.52); full dots: experimental results; empty dots: Thurber et al. [8].

The *Arora model* [9] expresses the mobility behavior as a function of doping concentration:

$$\mu_{\text{dop}} = \mu_{\text{min}} + \frac{\mu_{\text{d}}}{1 + ((N_{\text{A},0} + N_{\text{D},0})/N_0)^{A^*}} \tag{2.53}$$

where

$$\begin{gathered} \mu_{\text{min}} = A_{\text{min}} \cdot \left(\frac{T}{300\ \text{K}}\right)^{\alpha_m}, \qquad \mu_{\text{d}} = A_{\text{d}} \cdot \left(\frac{T}{300\ \text{K}}\right)^{\alpha_{\text{d}}} \\ N_0 = A_{\text{N}} \left(\frac{T}{300\ \text{K}}\right)^{\alpha_{\text{N}}}, \qquad A^* = A_{\text{a}} \cdot \left(\frac{T}{300\ \text{K}}\right)^{\alpha_{\text{a}}} \end{gathered} \tag{2.54}$$

The terms μ_{min}, μ_{d}, N_0 and A^* depend on temperature and on a set of coefficients, namely A_{min}, A_{d}, A_{N} and A_{a}. Table 2.3 reports the default parameters used in the TCAD simulator for silicon, as an example. Moreover, Fig. 2.9 demonstrates how accurate is the Arora model applied to a phosphorous-doped silicon with respect to the experimental results and, in addition, it shows that the electron mobility has strong variations with temperature for lower values of doping.

High-field saturation model

Carriers can also be subject to high electric fields and accumulate enough energy to undergo a scattering event. The carrier drift velocity is proportional to the electric field, unless the field is high enough to let drift velocity saturate to a finite speed v_{sat}.

Table 2.3 Silicon coefficients for Arora model.

Symbol	Electrons	Holes	Unit
A_{min}	88	54.3	cm^2/Vs
α_{m}	-0.57	-0.57	1
A_{d}	1252	407	cm^2/Vs
α_{d}	-2.33	-2.23	1
A_{N}	$1.25 \cdot 10^{17}$	$2.35 \cdot 10^{17}$	cm^{-3}
α_{N}	2.4	2.4	1
A_{a}	0.88	0.88	1
α_{a}	-0.146	-0.146	1

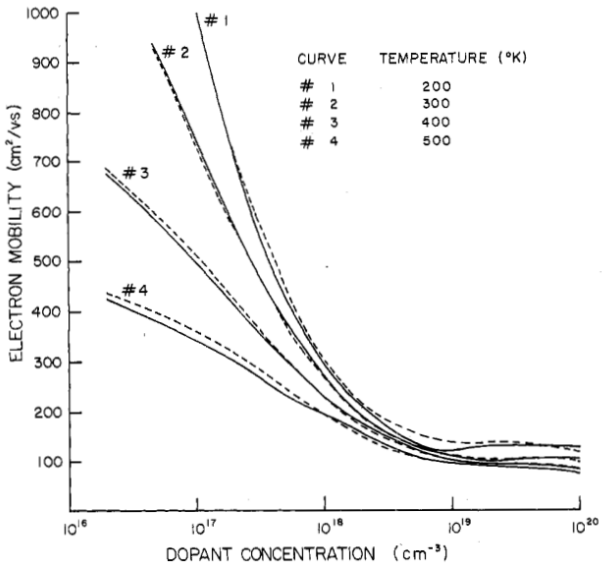

Fig. 2.9 Electron mobility in a phosphorous-doped silicon at four temperatures [9]. Solid lines: experimental values; dashed lines: corresponding values calculated with (2.53).

Table 2.4 Silicon coefficients for Canali model.

Symbol	**Electrons**	**Holes**	**Unit**
β_0	1.109	1.213	1
β_{exp}	0.66	0.17	1
α	0	0	1

The high-field saturation models includes three submodels [26]: the actual mobility model, the velocity saturation model and the driving force model.

The actual mobility model implemented in the in-house simulator is called *Canali model*: it originates from the Caughey-Thomas formula [40] and adds temperature-dependencies to the mobility. The model has the following expression:

$$\mu(F) = \frac{(\alpha+1)\mu_{\text{low}}}{\alpha + \left[1 + \left(\dfrac{(\alpha+1)\mu_{\text{low}}F_{\text{hfs}}}{v_{\text{sat}}}\right)^{\beta}\right]^{1/\beta}} \tag{2.55}$$

where μ_{low} is the low-field mobility, v_{sat} is the saturation velocity, F_{hfs} is the driving force, α is a coefficient and β is a temperature-dependent exponent:

$$\beta = \beta_0 \left(\frac{T}{300\ \text{K}}\right)^{\beta_{\text{exp}}} \tag{2.56}$$

The low field mobility corresponds to the constant mobility (2.51) or to the doping-dependent mobility (2.52) and (2.53). Table 2.4 reports the parameter values used in the TCAD solver for silicon, as an example. The carrier drift velocity is related to the electric field through the equation $v = \mu E$, as shown in Fig. 2.10. For sufficiently large electric field values, the velocity saturates to a finite value v_{sat}, described by different models. The in-house solver supports two velocity saturation models: the first one in (2.57) is recommended for silicon, the second one in (2.58) is recommended for GaAs.

$$v_{\text{sat}} = v_{\text{sat},0}\left(\frac{300\ \text{K}}{T}\right)^{v_{\text{sat,exp}}} \tag{2.57}$$

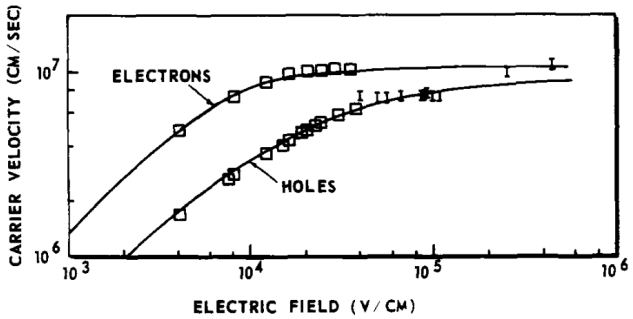

(a) Velocity-field curve in lightly-doped silicon [41].

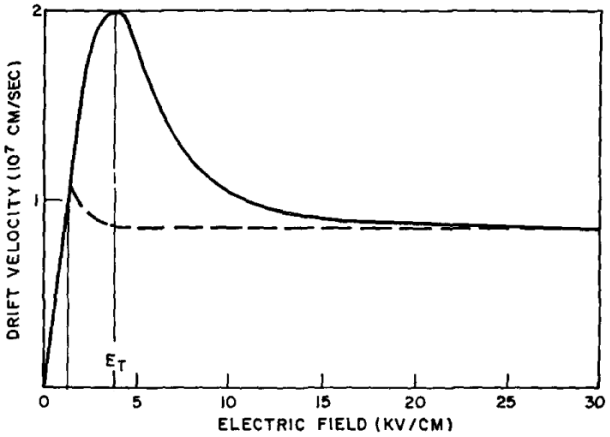

(b) Velocity-field curve for electrons in lightly-doped GaAs [42].

Fig. 2.10 Velocity-field curve at 300 K using typical parameter values.

$$v_{\text{sat}} = \begin{cases} A_{v_{\text{sat}}} - B_{v_{\text{sat}}} \left(\dfrac{T}{300\ \text{K}} \right) & v_{\text{sat}} > v_{\text{sat,min}} \\ v_{\text{sat,min}} & \text{otherwise} \end{cases} \tag{2.58}$$

The last quantity under analysis is the driving force for the electron and hole mobility models, which is usually modeled considering the electric field component parallel to the current density:

$$F_{\text{hfs},n} = \mathbf{E} \cdot \frac{\mathbf{J}_n}{J_n} \quad \text{and} \quad F_{\text{hfs},p} = \mathbf{E} \cdot \frac{\mathbf{J}_p}{J_p} \tag{2.59}$$

which corresponds to take the x or y component of $\mathbf{E}$. This model is physically correct, even if it can suffer from numeric instability when the current values are very small.

2.5.4 Generation-Recombination processes

Generation-Recombination processes consist of the exchange of carriers between conduction and valence band. These mechanisms can be *direct*, such as the spontaneous emission process, or *indirect*, such as the trap-assisted phenomenon. The latter is due to the presence of impurities in the semiconductor, which leads to the formation of energy levels in the bandgap. The energy levels E_t are described in terms of traps, responsible of capture/emission processes, which follow the Shockley-Read-Hole (SRH) recombination model and are described as the combination of four distinct events:

a. **Generation of a hole** (G_p): hole emission in the valence band.

b. **Generation of an electron** (G_n): electron emission in the conduction band.

c. **Recombination of a hole** (R_p): hole capture from the valence band.

d. **Recombination of an electron** (R_n): electron capture from the conduction band.

The net recombination rate for electrons and holes is $U_\alpha = R_\alpha - G_\alpha$, where $\alpha = n, p$. Since the net rates are independent and equal at the same time, the net recombination rate U^{SRH} is:

$$U^{\mathrm{SRH}} = \frac{np - n_i^2}{\tau_p(n+n_1) + \tau_n(p+p_1)} \tag{2.60}$$

where $n_1 = n_i \exp(E_t/k_B T)$ and $p_1 = n_i \exp(-E_t/k_B T)$. The terms τ_n and τ_p are the electron and hole lifetimes:

$$\tau_n = \frac{1}{N_t \sigma_n v_{th}^n} \quad \text{and} \quad \tau_p = \frac{1}{N_t \sigma_p v_{th}^p} \tag{2.61}$$

where σ_n and σ_p are the trap cross sections, v_{th}^n and v_{th}^p are the thermal velocities and N_t the trap concentration. This model is valid only in *static conditions*, whereas no time dependencies are considered, while dynamic effects can be accounted through the trap rate equation, explained in the previous section.

2.5.5 Thermionic emission model

The thermionic emission phenomenon in heterostructure devices, such as high electron mobility transistors (HEMTs) and heterojunction bipolar transistors (HBTs), is one of the most important conduction mechanisms involving the transport of carriers across the heterojunction. The PDD model is not very adequate to describe the behavior of abrupt heterointerfaces, since it neglects carrier transport across the heterojunctions. Therefore, a physical model describing the thermionic emission currents needs to be implemented.

Consider an heterointerface between material 1 and material 2, where the conduction band energy variation $\Delta E_C = E_{C2} - E_{C1}$ is higher than zero and, as a consequence, $\chi_1 > \chi_2$. The interface condition is [26, 43]:

$$J_{n,2} = J_{n,1} \quad \text{and} \quad J_{n,2} = a_n q \left[v_{\text{th}}^{n,2} n_2 - \frac{m_{\text{eff},n,2}}{m_{\text{eff},n,1}} v_{\text{th}}^{n,1} n_1 \exp\left(-\frac{\Delta E_C}{k_B T} \right) \right] \tag{2.62a}$$

$$J_{p,2} = J_{p,1} \quad \text{and} \quad J_{p,2} = -a_p q \left[v_{\text{th}}^{p,2} p_2 - \frac{m_{\text{eff},p,2}}{m_{\text{eff},p,1}} v_{\text{th}}^{p,1} p_1 \exp\left(-\frac{\Delta E_V}{k_B T} \right) \right] \tag{2.62b}$$

where the terms $m_{\text{eff},n,i}$ and $m_{\text{eff},p,i}$ are the effective masses, the coefficients a_n and a_p are equal to 2, while the emission velocities $v_{\text{th}}^{n,i}$ and $v_{\text{th}}^{p,i}$ are expressed as follows:

$$v_{\text{th}}^{n,i} = \sqrt{\frac{k_B T}{2\pi m_{\text{eff},n,i}}} \quad \text{and} \quad v_{\text{th}}^{p,i} = \sqrt{\frac{k_B T}{2\pi m_{\text{eff},p,i}}} \tag{2.63}$$

The thermionic emission current $J_{n,2}$ is the electron current density entering material 2, while $J_{n,1}$ is the electron current density leaving material 1, as shown in the AlGaAs/GaAs heterostructure of Fig. 2.11. The same mechanism can be repeated for the hole current densities.

2.5.6 Piezoelectric polarization model

In III-V semiconductors, such as Gallium Nitride (GaN) and Aluminum Nitride (AlN), the crystal structure and the type of symmetry play an important role in the definition of their electronic properties. In particular, the band gap is strictly related to the lattice constant of the crystal structure, while the hexagonal symmetry

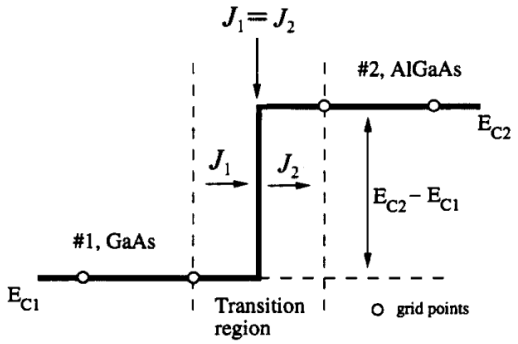

Fig. 2.11 Thermionic emission current of a general heterojunction interface [10].

affects the polarization effect, which is the sum of two components: *spontaneous polarization* and *piezoelectric polarization*.

In an unstrained III-V semiconductor, the relative movement of cations and anions with respect to their ideal position produces a spontaneous polarization, which results aligned along the <0001> direction, known also as the C-direction. If a mechanical strain is applied, a relative shift of anion and cation sub-lattices produces a piezoelectric polarization effect, which is summed to the spontaneous component, giving a total polarization vector **P**. The polarization vector follows the so-called *simplified strain model* by Ambacher *et al.* [44]:

$$\mathbf{P} = \begin{pmatrix} 0 \\ 0 \\ P_z^{\text{sp}} + P_z^{\text{pe}} \end{pmatrix} = \begin{pmatrix} 0 \\ 0 \\ P_z^{\text{sp}} + P_{\text{strain}} \end{pmatrix} \tag{2.64}$$

Notice that the x and y components are null, therefore along the C-axis, the spontaneous polarization charges cover the whole crystal, but the sum of the internal components is null, hence the remaining charge is distributed on the opposite faces of the semiconductor [18], as shown in Fig. 2.12. Furthermore, the term P_z^{sp} is a constant coefficient depending on the material and P_{strain} is expressed by:

$$P_{\text{strain}} = 2 \cdot \frac{a - a_0}{a_0} \cdot \left(e_{31} - \frac{c_{13}}{c_{33}} e_{33} \right) \tag{2.65}$$

where c_{ij} are the stiffness constants, e_{ij} are the strain-charge piezoelectric coefficients, a_0 is the strained lattice constant and a is the unstrained lattice constant. Table 2.5

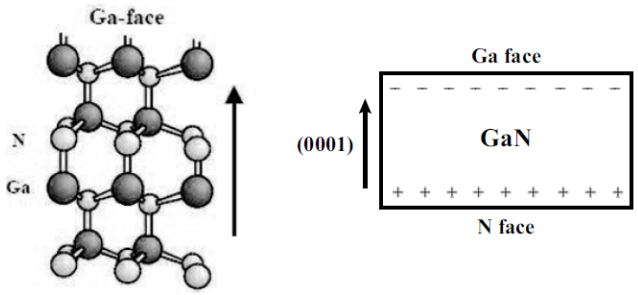

Fig. 2.12 GaN crystal structure (left) and polarization distribution along the C-axis (right).

Table 2.5 Default coefficients for spontaneous and piezoelectric polarization.

	GaN	**AlN**	**InN**
a [Å]	3.189	3.111	3.544
P_z^{sp} [C/m^2]	-0.029	-0.081	-0.032
e_{31} [C/m^2]	-0.35	-0.5	-0.48
e_{33} [C/m^2]	1.27	1.79	1.06
c_{13} [Pa]	$1.06 \cdot 10^{11}$	$1.08 \cdot 10^{11}$	$9.2 \cdot 10^{10}$
c_{33} [Pa]	$3.98 \cdot 10^{11}$	$3.73 \cdot 10^{11}$	$2.24 \cdot 10^{11}$

reports the default coefficients used in the in-house simulator for different nitride-based materials.

The vector polarization charge q_{PE} is added to the right-hand side of the Poisson equation, leading to:

$$\nabla \cdot (\varepsilon \nabla \phi) = -q \cdot (p - n + N_{\mathrm{D}} - N_{\mathrm{A}}) - q_{\mathrm{PE}} \tag{2.66}$$

where

$$q_{\mathrm{PE}} = -\mathrm{activation} \nabla \cdot \mathbf{P} \tag{2.67}$$

Notice that the activation coefficient is a positive real calibration parameter. Let us denote as *volumic* polarization charge the term q_{PE} and as *surface* polarization charge the term $\mathbf{P}$.

Chapter 3

Discretization techniques and numerical implementation

3.1 Introduction

Purpose of this chapter is to give details on how the in-house physics-based simulator is implemented. The solver has been implemented in MATLAB® and it is composed of two main parts: the *structure and grid generation* and the *device physical simulation*. The first one allows to define an initial structural description of a device in terms of geometrical dimensions, materials, doping concentration and types of contacts. Moreover, it gives the possibility to generate a spatial grid in the input structure, which can be finer or coarser depending on the device regions. The second part is dedicated to the physical simulation, hence it gives the possibility to select the system of equations to be solved and define the operating condition of the device under analysis. For instance, in static conditions, one can solve the system at thermodynamic equilibrium or at certain voltages, while in dynamic conditions, one can define not only a static working point, but also the device operating frequency and external periodic sources.

The PDD model is characterized by a system of partial differential equations (PDEs): computers are hardly able to understand PDEs, nevertheless there are different environments like MATLAB®, which are suited to deal with matrices. To this aim, PDEs need to be discretized, hence translated into a set of algebraic equations. Notice that the PDD model also involves time dependencies: in static

conditions, time derivatives are equal to zero and a *spatial discretization* is sufficient to assemble the PDEs in the TCAD simulator; in dynamic conditions, there are non-zero time derivatives, which again are hardly handled by computers, therefore *temporal discretization* is also required. Furthermore, since PDEs are non-linear, it is not possible to find a rigorous analytical expression of the discretized unknowns, therefore a numerical solution is needed and requires the use of iterative techniques, such as Newton's method.

The following sections are focused on a more detailed description of spatial and temporal discretization techniques exploited in the in-house solver. Moreover, a brief overview on solution techniques is proposed in order to understand how the discretized physics-based equations are assembled to allow for their solution.

3.2 Spatial discretization: finite-boxes scheme

The PDD model (2.16) is a set of time-dependent PDEs characterized by three unknowns depending on *time* and *space*:

$$\phi(x,y,t) \qquad n(x,y,t) \qquad p(x,y,t) \tag{3.1}$$

where the space coordinates are here x and y only. As anticipated, since computers are not well suited to handle differential operators, they need to be discretized, namely the overall domain in which they are defined must be divided into a set of discrete points, called *mesh* or *grid* points, in order to sample and compute the solution of the system of PDEs only at those discrete points. In this section, the discussion is only focused on spatial discretization techniques, while temporal discretization methods will be analysed later on.

The main discretization techniques are divided in two categories [11, 45]: the *finite difference method* and the *finite element method* (FEM). Both methods consist in establishing a set of algebraic equations, whose solution is defined at each discrete point, hence their difference lies in the way the differential operators are treated and how the algebraic expressions are obtained. The finite difference method approximates the differential operator with an incremental ratio, which is obtained from the Taylor expansion around the point of interest truncated at the first-order. Consider the generic function $f(z)$ and a set of non-uniformly distributed points $(z_1, z_2, \ldots, z_n)$,

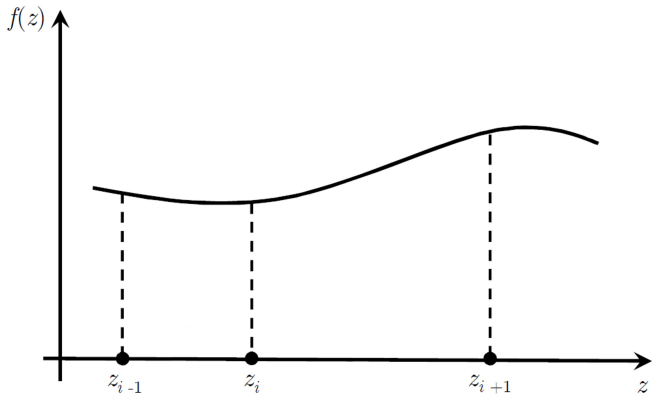

Fig. 3.1 Generic function $f(z)$ along a set of non-uniformly spaced grid points.

as shown in Fig. 3.1, the first derivative at point z_i can be written as:

$$\left.\frac{df}{dz}\right|_{z=z_i} = \frac{f(z_{i+1}) - f(z_{i-1})}{z_{i+1} - z_{i-1}} \tag{3.2}$$

This approximation strongly relies on the number of grid points: the larger the number, the higher the computational cost and the better the accuracy. On the other hand, in the finite element method, the unknowns of the problem are approximated by known polynomial functions, called basis functions and, since the differentiation of the basis function can be computed analytically, the application of the differential operator is simple. These two descriptions have different similarities, for example in terms of local errors (see [11] for details), but finite element discretizations are more limited in the treatment of parabolic or hyperbolic PDE components, leading to numerical instability issues. These problems are included in a broad category of numerical problems, called *advection-diffusion-reaction problems* [46], and they have no evidence in the discretization of Poisson equation, but rather in the transport equations. The finite difference method is the preferred technique used for the discretization of the physics-based equations. In the in-house solver a particular methodology based on finite differences, namely *finite-boxes discretization scheme*, is exploited. Nowadays, this discretization scheme is considered a standard technique, well established and widespread in commercial TCAD simulators.

Before describing the formulation of the finite-boxes discretization applied to PDD system, it is important to give some details on the definition of the grid points and how they are connected one to the other [11]. First of all, the points must

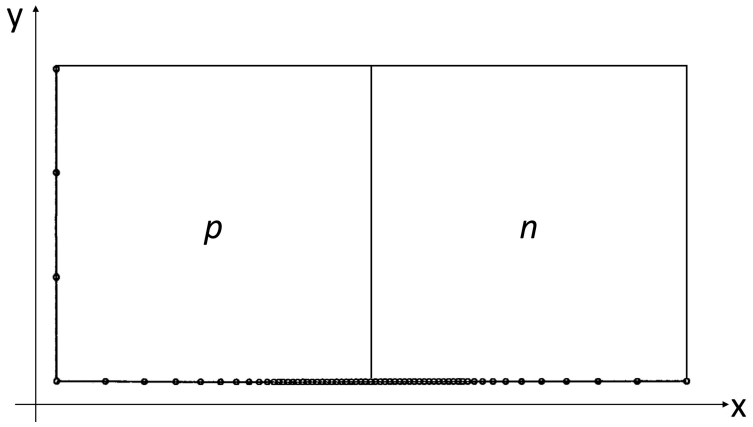

Fig. 3.2 Example of grid points distribution along the *x*-and-*y* axes in a *pn* diode.

be distributed on the overall domain in such a way that all the physical quantities involved in the system are accurately approximated. Consider for example the two-dimensional *pn* junction, shown in Fig. 3.2. Along the *y*-axis, physical quantities like electrostatic potential, carrier concentrations, doping concentration, etc. remain approximately constant, therefore the space between the grid points can be fairly large. Along the *x*-axis, in the active region around the junction, where a depletion region is formed, there are important changes of the main physical parameters, therefore a finer mesh is necessary to correctly describe them. The second aspect to consider concerns the connectivity between grid points [11]: the connection of two or more mesh points forms a *subspace*. In one dimensional problems, two adjacent nodes form a segment, in two dimensions they form polygons (triangles or rectangles) and in three dimensions polyedra (tetrahedron, hexahedron or prism). Depending on the type of subspace, there are different possible grid structures, with uniform or non-uniform mesh points distribution, as shown in Fig. 3.3 for a 2D case. In the in-house solver, the finite-boxes discretization exploits a two-dimensional non-uniform mesh structure with triangular subspaces. The starting point to obtain this grid representation is a non-uniform rectangular mesh, corresponding to a *tensor-product grid*. As shown in Fig. 3.4 (left), a set of mesh points are distributed in a non-uniform pattern along the *x*-and-*y* axes and from their intersection, rectangles are formed. The diagonal of each rectangle allows to pass from this configuration to the one of Fig. 3.4 (right), characterized by *right triangles* (see [11] for details). The finite difference discretization scheme applied to triangular (or rectangular) grids is based on the two-dimensional Gauss's Law [47], which ensures the conservation of carriers and charge, and takes the name of *generalized box discretization* [48, 49].

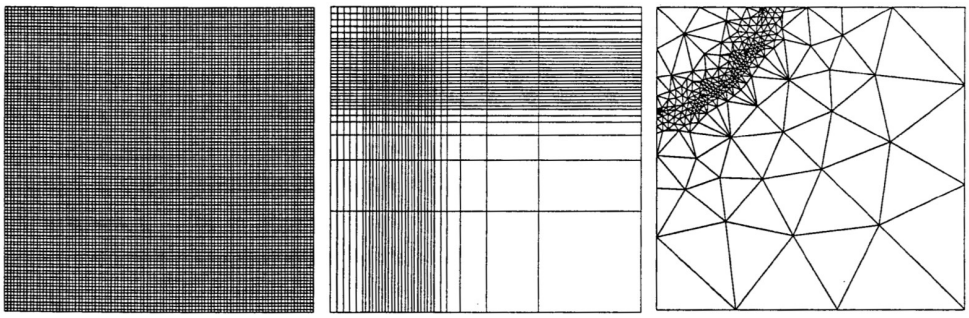

(a) (b) (c)

Fig. 3.3 Examples of 2D and 3D grid structures [11]: (a) uniform rectangular, (b) non-uniform rectangular (general tensor-product), (c) general triangular.

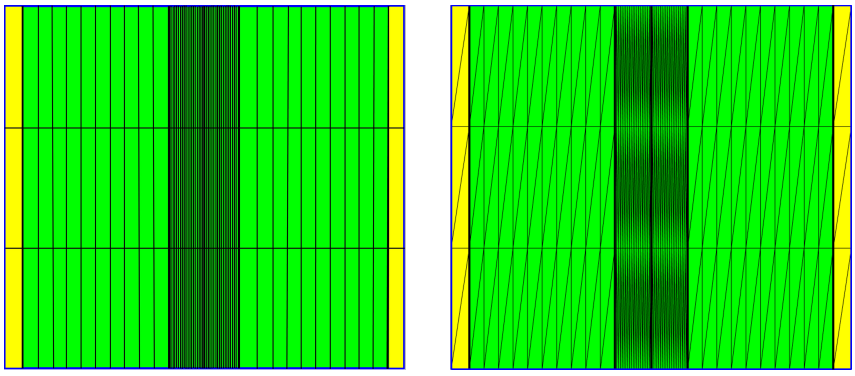

Fig. 3.4 Two-dimensional non-uniform mesh representation with different subspaces: rectangles (left) and right triangles (right).

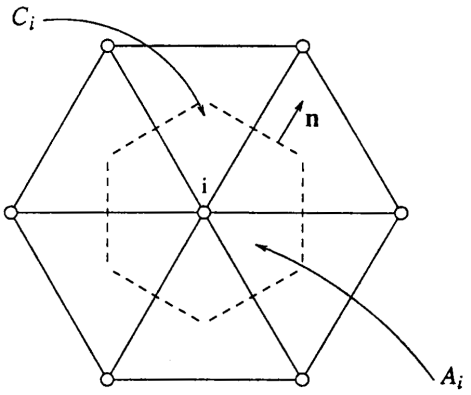

Fig. 3.5 Control area associated to node i for the application of Gauss's Law [11].

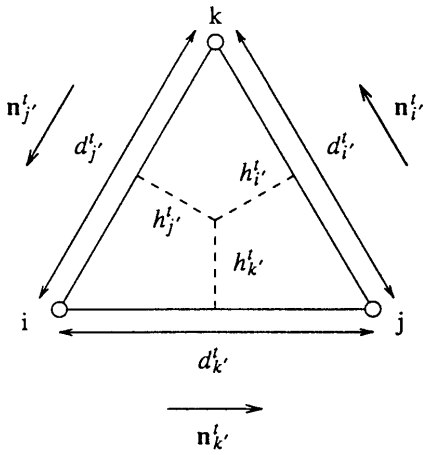

Fig. 3.6 Partitioning of a triangular subspace by perpedicular bisectors [11].

Consider the DD model of (2.16) in compact form:

$$\nabla \cdot \mathbf{F} = \frac{\partial f}{\partial t} + u \tag{3.3}$$

where $\mathbf{F}$ and f are the unknown vector and scalar functions, respectively, while u is the known scalar source term. Gauss's Law is applied to the control area A_i:

$$\int_{A_i} \nabla \cdot \mathbf{F} \, \mathrm{d}x \, \mathrm{d}y = \int_{C_i} \mathbf{F} \cdot \mathbf{n} \, dS = \frac{\partial}{\partial t} \int \int_{A_i} f \, \mathrm{d}x \, \mathrm{d}y + \int \int_{A_i} u \, \mathrm{d}x \, \mathrm{d}y \tag{3.4}$$

where A_i is the area associated to node i, known as the Vornoi area and delimited by the dashed bounding line C_i, while $\mathbf{n}$ is the unit normal vector to C_i (see Fig. 3.5). The bounding line C_i is obtained dividing each triangle t into three subregions defined by its perpendicular bisectors $h^t_{i'}$, $h^t_{j'}$ and $h^t_{k'}$, whose intersection point is the center of the *circumscribed circle* of the triangle (see Fig. 3.6). In case of a right-triangles grid structure, there are two perpendicular bisectors distributed as shown in Fig. 3.7 and their intersection leads to the formation of boxes, hence the name finite-boxes scheme. Notice that each triangle angle must be lower than 90° due to the fact that the circumscribed circle of obtuse triangles lies outside the triangle itself. Moreover, the area A_i should be as close as possible to node i and, for each node, it is possible to define the total area A_i as $A_i = \sum_t A^t_i$, where the term A^t_i is the area delimited by the perpendicular bisectors in a single triangle t and associated to node i.

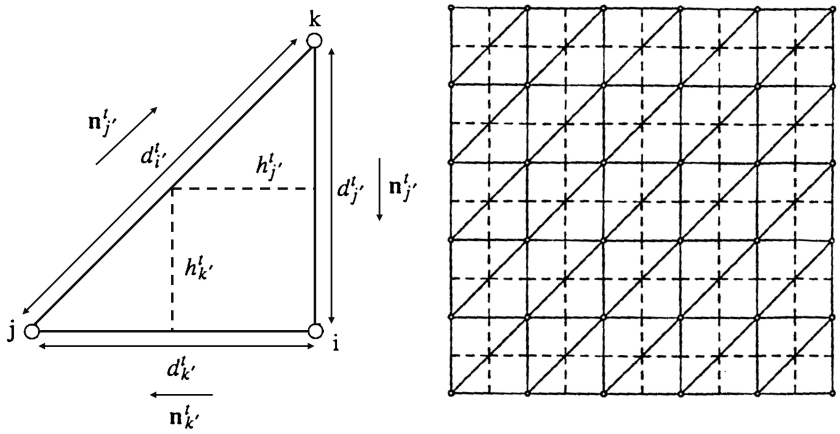

Fig. 3.7 Finite-boxes partitioning in a grid structure based on right triangles.

3.2.1 Discretization of the PDD model

Let us apply the finite-box discretization procedure to the PDD model. Each equation of the system, i.e. the Poisson equation and the continuity equations for electrons and holes, are defined on a 2D non-uniform grid structure of n_n nodes with triangular subspaces.

Poisson equation

Consider the Poisson equation (2.1a) and apply Gauss's Law at each triangle t:

$$\sum_t \left[\int_{C_i^t} \varepsilon \nabla\phi \cdot \mathbf{n} \, \mathrm{d}S^t + \int\int_{A_i^t} \rho \, \mathrm{d}A^t \right] \tag{3.5}$$

In the first integral, the product $\nabla\phi \cdot \mathbf{n}$ is expressed through finite differences, since the unit vectors $n^t_{j'}$, $n^t_{k'}$ and $n^t_{i'}$ are parallel to the edges $d^t_{j'}$, $d^t_{k'}$ and $d^t_{i'}$:

$$\nabla\phi \cdot \mathbf{n}^t_{j'} = \frac{\phi_i - \phi_k}{d^t_{j'}} \tag{3.6a}$$

$$\nabla\phi \cdot \mathbf{n}^t_{k'} = \frac{\phi_j - \phi_i}{d^t_{k'}} \tag{3.6b}$$

$$\nabla\phi \cdot \mathbf{n}^t_{i'} = \frac{\phi_k - \phi_j}{d^t_{i'}} \tag{3.6c}$$

where $d^t_{j'}$, $d^t_{k'}$ and $d^t_{i'}$ are the lengths of the edges j', k' and i', as shown in Fig. 3.6. Dielectric permittivity and electric field are assumed constant along each segment $h^t_{j'}$, $h^t_{k'}$ and $h^t_{i'}$, hence the first integral becomes:

$$\begin{aligned}\int_{C^t_i} \varepsilon^t \nabla\phi \cdot \mathbf{n}\, \mathrm{d}S^t &= \varepsilon^t_{k'}\, \nabla\phi \cdot \mathbf{n}^t_{k'}\, h^t_{k'} \;-\; \varepsilon^t_{j'}\, \nabla\phi \cdot \mathbf{n}^t_{j'}\, h^t_{j'} \;-\; \varepsilon^t_{i'}\, \nabla\phi \cdot \mathbf{n}^t_{i'}\, h^t_{i'} \\ &= \varepsilon^t_{k'}\, (\phi_j - \phi_i)\frac{h^t_{k'}}{d^t_{k'}} \;-\; \varepsilon^t_{j'}\, (\phi_i - \phi_k)\frac{h^t_{j'}}{d^t_{j'}} \;-\; \varepsilon^t_{i'}\, (\phi_k - \phi_j)\frac{h^t_{i'}}{d^t_{i'}}\end{aligned} \tag{3.7}$$

The second integral is now taken into account: since the space charge is constant on A^t_i, it is approximated by $\rho^t_i A^t_i$, where all the quantities involved in ρ^t_i are defined at node i for each triangle t. The final discretized form for Poisson equation is:

$$\begin{aligned}\sum_t \Bigg[&\varepsilon^t_{k'}(\phi_j - \phi_i)\frac{h^t_{k'}}{d^t_{k'}} + \varepsilon^t_{j'}(\phi_k - \phi_i)\frac{h^t_{j'}}{d^t_{j'}} + \varepsilon^t_{i'}(\phi_j - \phi_k)\frac{h^t_{i'}}{d^t_{i'}} \\ &+ [q \cdot (p_i - n_i + N_{\mathrm{D}_i} - N_{\mathrm{A}_i}) + \rho_{\mathrm{F}_i}]\; A^t_i = 0 \Bigg]\end{aligned} \tag{3.8}$$

which is a linear expression as a function of electrostatic potential and carrier concentrations. The fixed charge and the net doping concentration are independent from the solution unless the incomplete ionization of dopants is considered. In this case, $N_{\mathrm{D}_i} - N_{\mathrm{A}_i}$ are functions of n_i and p_i, respectively, as indicated in (2.50).

An interesting point is the discretization procedure adopted for the spontaneous and piezoelectric charge, characterizing nitride-based semiconductors, since it enters the space charge concentration. The in-house solver provides two possible implementations for the polarization charge, which can be treated as a *volumic* or a *surface* charge distribution. Consider the heterostructure AlGaN/GaN of Fig. 3.8: the volumic polarization charge q_{PE} is a vector defined for each mesh node i, with all zero elements except for the ones lying on the heterointerface (indicated in red). This implementation allows the user to *directly* define the amount of net polarization charge at the interface between the two materials, as shown in Fig. 3.9, where $q_{\mathrm{PE,int}} = 16$ C cm^{-3}. Therefore, the vector q_{PE} is added to the space charge density of the Poisson equation, as indicated in (2.66). On the other hand, the polarization charge $\mathbf{P}$ is a piecewise constant vector defined for each mesh node i, following the *simplified strain model* explained in Chapter 2. This implementation allows the user to define the amount of surface polarization charge of each material, as shown in Fig.

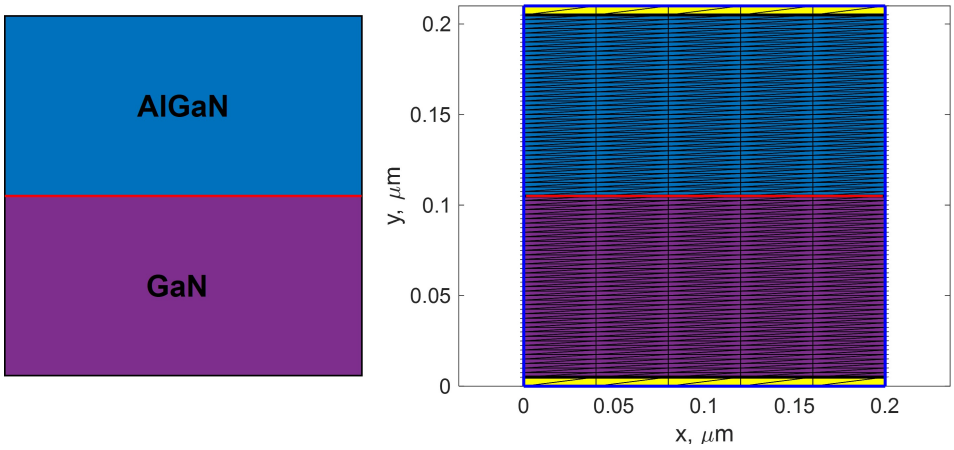

Fig. 3.8 Example of heterostructure AlGaN/GaN.

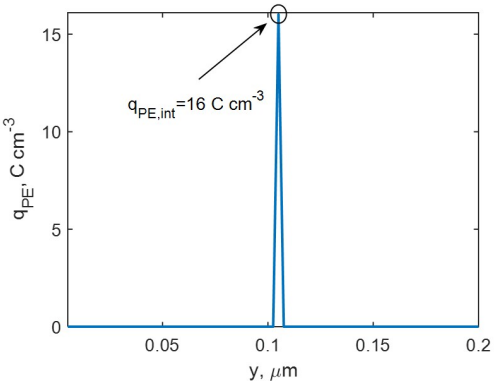

Fig. 3.9 Volumic polarization distribution.

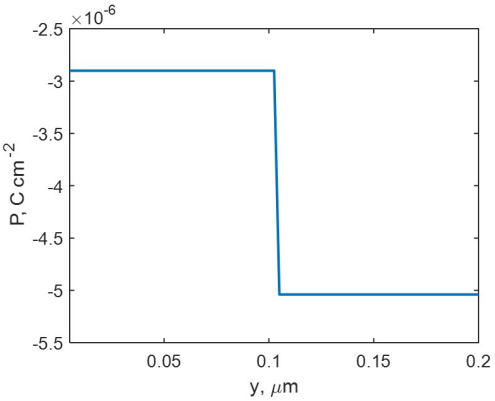

Fig. 3.10 Surface polarization distribution.

3.10, while the volumic vector q_{PE} is *indirectly* obtained using (2.67), hence adding the divergence of **P** to the Poisson equation. Fig. 3.11a shows the conduction band energy of the AlGaN/GaN heterojunction at thermodynamic equilibrium obtained for a grid structure of 500 nodes: due to the coarse mesh, both the results do not exhibit a great precision. Doubling the number of grid points, the conduction band presents the typical 2DEG channel, that characterizes nitride-based heterostructures, in both the implementations, as shown in Fig. 3.11b.

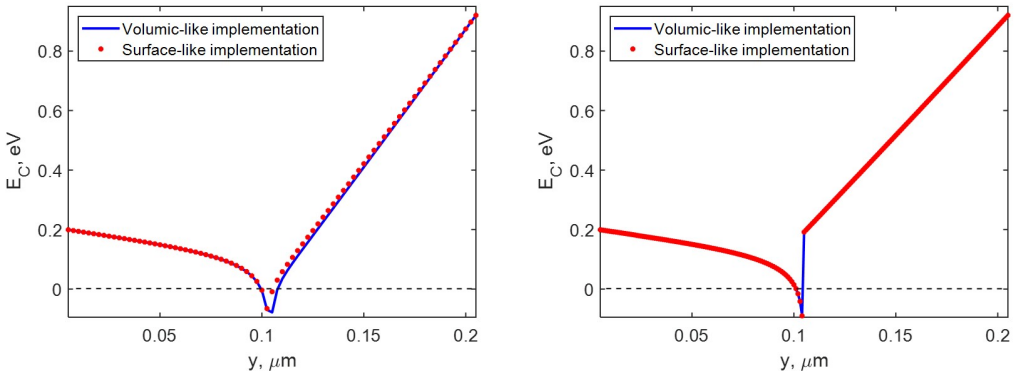

(a) Coarse grid structure.

(b) Fine grid structure.

Fig. 3.11 Comparison between the conduction band energy at thermodynamic equilibrium obtained in the AlGaN/GaN heterostructure with the two implementation methods.

Continuity equations

Consider the continuity equation for electrons (2.1b) and apply Gauss's Law at each triangle t:

$$\sum_t \left[\int_{C_i^t} \mathbf{J}_n \cdot \mathbf{n} \, \mathrm{d}S^t - \int\int_{A_i^t} \left(\frac{\partial n}{\partial t} + U_n \right) \mathrm{d}A^t \right] \tag{3.9}$$

Let us start from the second integral: since the integrand function is considered constant on A_i^t, it is approximated by:

$$\int\int_{A_i^t} \left(\frac{\partial n}{\partial t} + U_n \right) \mathrm{d}A^t \approx \left(\frac{\partial n_i}{\partial t} + U_{n_i}^t \right) A_i^t \tag{3.10}$$

Concerning the first integral, it is treated similarly to the Poisson equation, therefore the current density is considered constant along each segment $h_{j'}^t$, $h_{k'}^t$ and $h_{i'}^t$:

$$\int_{C_i^t} \mathbf{J}_n \cdot \mathbf{n} \, \mathrm{d}S^t = \mathbf{J}_n \cdot \mathbf{n}_{k'}^t \, h_{k'}^t \; - \; \mathbf{J}_n \cdot \mathbf{n}_{j'}^t \, h_{j'}^t \; - \; \mathbf{J}_n \cdot \mathbf{n}_{i'}^t \, h_{i'}^t \tag{3.11}$$

The application of a *pure* finite difference discretization scheme on (3.11) leads to numerical instability problems due to the fact that they include convective-diffusive terms. Therefore, the Scharfetter-Gummel approach [50] is introduced in order to provide a stable discretization of the drift-diffusion constitutive relations. Recalling

(2.5a), the term $\mathbf{J}_n \cdot \mathbf{n}^t_{k'}$ can be written along the edge k' going from node i to node j:

$$\mathbf{J}_n \cdot \mathbf{n}^t_{k'} = q\mu_n \left(-n\nabla\phi \cdot \mathbf{n}^t_{k'} + \frac{D_n}{\mu_n}\frac{dn}{dx} \right) \Longrightarrow \frac{\mathbf{J}_n \cdot \mathbf{n}^t_{k'}}{q\mu_{n_{k'}}} + n\,\nabla\phi \cdot \mathbf{n}^t_{k'} \tag{3.12}$$

where mobility, diffusivity and temperature are assumed constant along each edge. Integrating (3.12) between x_i and x_j and expressing $\nabla\phi$ through finite differences, one can obtain:

$$\mathbf{J}_n \cdot \mathbf{n}^t_{k'} = \frac{qD_{n_{k'}}}{d^t_{k'}} \left[n_j \mathrm{B}\left(\frac{\Delta\phi_{ij}}{V_\mathrm{T}} \right) - n_i \mathrm{B}\left(-\frac{\Delta\phi_{ij}}{V_\mathrm{T}} \right) \right] \tag{3.13}$$

where $\Delta\phi_{ij} = \phi_j - \phi_i$ and $\mathrm{B}(x)$ is the Bernoulli function, which is defined as:

$$\mathrm{B}(x) = \frac{x}{\exp(x) - 1} \tag{3.14}$$

The same procedure is repeated for $\mathbf{J}_n \cdot \mathbf{n}^t_{j'}$ and $\mathbf{J}_n \cdot \mathbf{n}^t_{i'}$, leading to the final discretized form of the electron continuity equation:

$$\sum_t \left[\frac{h^t_{k'}}{d^t_{k'}} I^t_{nk'} - \frac{h^t_{j'}}{d^t_{j'}} I^t_{nj'} - \frac{h^t_{i'}}{d^t_{i'}} I^t_{ni'} - \left(\frac{\partial n_i}{\partial t} + U^t_{n_i} \right) A^t_i \right] = 0 \tag{3.15}$$

where

$$I^t_{nk'} = qD_{n_{k'}} \left[n_j \mathrm{B}\left(\frac{\Delta\phi_{ij}}{V_\mathrm{T}} \right) - n_i \mathrm{B}\left(-\frac{\Delta\phi_{ij}}{V_\mathrm{T}} \right) \right] \tag{3.16a}$$

$$I^t_{nj'} = qD_{n_{j'}} \left[n_i \mathrm{B}\left(\frac{\Delta\phi_{ki}}{V_\mathrm{T}} \right) - n_k \mathrm{B}\left(-\frac{\Delta\phi_{ki}}{V_\mathrm{T}} \right) \right] \tag{3.16b}$$

$$I^t_{ni'} = qD_{n_{i'}} \left[n_k \mathrm{B}\left(\frac{\Delta\phi_{jk}}{V_\mathrm{T}} \right) - n_j \mathrm{B}\left(-\frac{\Delta\phi_{jk}}{V_\mathrm{T}} \right) \right] \tag{3.16c}$$

The Scharfetter-Gummel discretization procedure can be also applied to the hole continuity equation, whose discretized form is:

$$\sum_t \left[\frac{h^t_{k'}}{d^t_{k'}} I^t_{pk'} - \frac{h^t_{j'}}{d^t_{j'}} I^t_{pj'} - \frac{h^t_{i'}}{d^t_{i'}} I^t_{pi'} + \left(\frac{\partial p_i}{\partial t} + U^t_{p_i} \right) A^t_i \right] = 0 \tag{3.17}$$

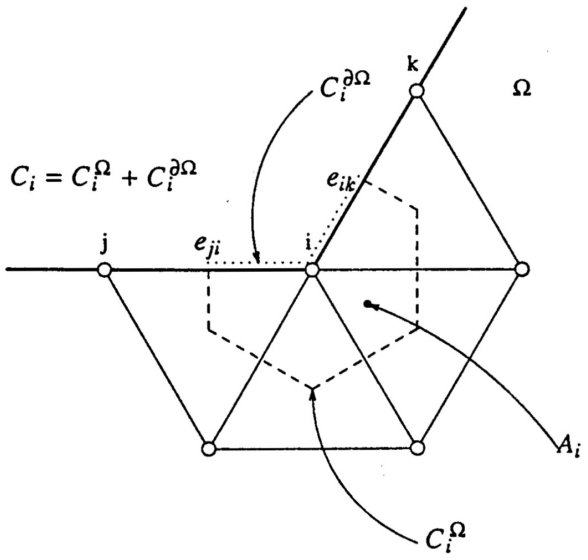

Fig. 3.12 Representation of a peripheral bonding line [11].

where

$$I^t_{pk'} = qD_{p_{k'}}\left[p_j \mathrm{B}\left(\frac{\Delta\phi_{ij}}{V_\mathrm{T}}\right) - p_i \mathrm{B}\left(-\frac{\Delta\phi_{ij}}{V_\mathrm{T}}\right)\right] \tag{3.18a}$$

$$I^t_{pj'} = qD_{p_{j'}}\left[p_i \mathrm{B}\left(\frac{\Delta\phi_{ki}}{V_\mathrm{T}}\right) - p_k \mathrm{B}\left(-\frac{\Delta\phi_{ki}}{V_\mathrm{T}}\right)\right] \tag{3.18b}$$

$$I^t_{pi'} = qD_{p_{i'}}\left[p_k \mathrm{B}\left(\frac{\Delta\phi_{jk}}{V_\mathrm{T}}\right) - n_j \mathrm{B}\left(-\frac{\Delta\phi_{jk}}{V_\mathrm{T}}\right)\right] \tag{3.18c}$$

Boundary conditions

The finite-boxes discretization can be applied to each mesh point included in the device domain, except for nodes lying on peripheral device edges or interfaces between two different materials (for example electrical contact nodes). Consider a bonding line C_i characterized by two components (see Fig. 3.12): C_i^{Ω} inside the device and $C_i^{\partial\Omega}$ on the boundary. Applying Gauss's Law to (3.3), one can obtain [11]:

$$\int_{C_i^{\Omega}} \mathbf{F}\cdot\mathbf{n}\,\mathrm{d}S = \int\int_{A_i} u\,\mathrm{d}x\,\mathrm{d}y = -\int_{C_i^{\partial\Omega}} \mathbf{F}\cdot\mathbf{n}\,\mathrm{d}S \tag{3.19}$$

where $\mathbf{F}$ is the flux, i.e. $\mathbf{E}$, $\mathbf{J}_n$ or $\mathbf{J}_p$. The left-hand side involves the mesh nodes inside the device, while the right-hand side only considers the grid points on the boundary.

Concerning the boundary nodes lying on peripheral device edges, homogeneous Neumann boundary conditions ($\mathbf{F}\cdot\mathbf{n}=0$) are enforced to (3.19), since no flux passes through the boundary edges. One can find that the discretized expressions for peripheral nodes are equal to (3.8), (3.15) and (3.17). Concerning the nodes lying on electrical terminals, the boundary condition depends on the type of contact. Dirichlet boundary conditions are enforced when the value of ϕ, n and p is fixed. They can be applied to ohmic contacts, leading to (2.23) and (2.24), whose discretized expressions are:

$$\phi_{i_c}-\left[v_k+\frac{k_\mathrm{B}T}{q}\mathrm{asinh}\left(\frac{N_\mathrm{D}-N_\mathrm{A}}{2n_i}\right)\right]=0 \tag{3.20a}$$

$$n_{i_c}-n_0=0 \tag{3.20b}$$

$$p_{i_c}-p_0=0 \tag{3.20c}$$

where i_c indicates the contact node. Dirichlet boundary conditions are also applied to "contacts on insulators", leading to (2.25) and (2.26), whose discretized form is:

$$\phi_{i_c}-(v_k-\phi_\mathrm{MS})=0 \tag{3.21a}$$

$$n_{i_c}=p_{i_c}=0 \tag{3.21b}$$

Non-homogeneous Neumann boundary conditions are instead enforced on Schottky contacts, when the external flux depends on internal quantities, such as potential or carrier concentration. Hence, (2.27) and (2.28) assume the following discretized expression:

$$\phi_{i_c}-\left[v_k-\phi_\mathrm{B}+\frac{k_\mathrm{B}T}{q}\ln\left(\frac{N_\mathrm{C}}{n_i}\right)\right]=0 \tag{3.22a}$$

$$\mathbf{J}_n\cdot\mathbf{n}-qv_{\mathrm{th},n}(n_{i_c}-n_0^\mathrm{B})d_{i'_c}=0 \tag{3.22b}$$

$$\mathbf{J}_p\cdot\mathbf{n}+qv_{\mathrm{th},p}(p_{i_c}-p_0^\mathrm{B})d_{i'_c}=0 \tag{3.22c}$$

where $\mathbf{J}_n\cdot\mathbf{n}$ and $\mathbf{J}_n\cdot\mathbf{n}$ are discretized as shown in (3.15) and (3.17).

3.2.2 Discretization of external circuit equations

In order to perform mixed-mode simulations, the PDD model can be coupled to external circuit equations, whose unknowns are expressed as follows:

$$v_k(t) \qquad i_k(t) \tag{3.23}$$

The voltage-controlled equation (2.31) involves time-varying quantities defined on each device terminal k, therefore no spatial discretization is needed. The current equation (2.33) involves the term i_k, which is defined on the k terminal, and the electron, hole and displacement current densities, following the finite-boxes discretization scheme, previously described.

3.3 Temporal discretization: the HB formulation

As anticipated in (3.1), the PDD model involves time-dependent unknowns, for instance the time derivative of the carrier concentrations $\frac{\partial n}{\partial t}$ and $\frac{\partial p}{\partial t}$. In static conditions, the time derivatives are equal to zero and the discretized model becomes a system of non-linear algebraic equations. In dynamic conditions, these are non-zero derivatives, which are treated in different ways according to the type of device operating condition. For example, the Small-Signal (SS) operation implies a small time-varying perturbation around the DC working point and the discretized PDD model can be linearized founding the solution directly in the frequency domain. Periodic or quasi-periodic[1] Large-Signal (LS) operating conditions are treated exploiting the Harmonic Balance (HB) technique [51, 29], suited for LS non-linear circuit simulations [28, 52]. Finally, transient conditions require time-stepping algorithms to be solved, but they are not implemented in the in-house solver, therefore their treatment is out of the scope of this work. Moreover, there are also less conventional type of analyses, namely the sensitivity [53, 54] and noise analysis [13]: the first one involves a small variation of a device parameter in DC, SS or LS conditions, while the second one can be a SS noise or a LS noise analysis. These are implemented in the in-house code, as explained in Chapter 4. As anticipated in Chapter 2, time-dependencies can be described in time-domain or frequency-domain regimes:

[1] A quasi-periodic function of time is the superposition of periodic waveforms, whose periods are incommensurate [28].

time-domain techniques do not perform efficiently, therefore frequency-domain approaches are preferred, whenever applicable, because they are easier and more efficient solutions especially for periodic or quasi-periodic operation regimes. As anticipated in Chapter 2, one of the most used frequency-domain techniques suited for non-linear networks is the HB method.

Purpose of this section is to apply the HB formalism, described in Appendix A, to the PDD model equations, restricting the treatment to the periodic LS regime, therefore only single-tone time-varying signals are taken into account. Recalling (3.1), the unknowns of the PDD model can be sampled, recalling (A.4), into $n_{\mathrm{H}} = 2N_{\mathrm{H}} + 1$ equispaced times:

$$\phi(t) \Longleftrightarrow [\phi(t_1), \phi(t_2), ..., \phi(t_{2N_{\mathrm{H}}+1})]^T = \phi^T \tag{3.24a}$$

$$n(t) \Longleftrightarrow [n(t_1), n(t_2), ..., n(t_{2N_{\mathrm{H}}+1})]^T = n^T \tag{3.24b}$$

$$p(t) \Longleftrightarrow [p(t_1), p(t_2), ..., p(t_{2N_{\mathrm{H}}+1})]^T = p^T \tag{3.24c}$$

The time-sampled vector can be translated in the frequency domain using the $\mathbf{\Gamma}$ matrix defined in (A.7) and (A.8), which implement a discretized Fourier transform:

$$\phi_{\mathrm{H}} = \mathbf{\Gamma} \cdot \phi \quad \text{where} \quad \phi_{\mathrm{H}}^T = [\phi_0, \phi_{c1}, \phi_{s1}, \phi_{c2}, \phi_{s2}, ..., \phi_{cN_{\mathrm{H}}}, \phi_{sN_{\mathrm{H}}}]^T \tag{3.25a}$$

$$n_{\mathrm{H}} = \mathbf{\Gamma} \cdot n \quad \text{where} \quad n_{\mathrm{H}}^T = [n_0, n_{c1}, n_{s1}, n_{c2}, n_{s2}, ..., n_{cN_{\mathrm{H}}}, n_{sN_{\mathrm{H}}}]^T \tag{3.25b}$$

$$p_{\mathrm{H}} = \mathbf{\Gamma} \cdot p \quad \text{where} \quad p_{\mathrm{H}}^T = [p_0, p_{c1}, p_{s1}, p_{c2}, p_{s2}, ..., p_{cN_{\mathrm{H}}}, p_{sN_{\mathrm{H}}}]^T \tag{3.25c}$$

Notice that, in case of single-tone time-dependent signals, the HB technique is applied in a real Fourier representation. Moreover, the PDD also involves the time derivatives of the carrier concentrations in the transport equations (2.5) and recalling (A.12), they can be written as:

$$\frac{\partial n(t)}{\partial t} \Longleftrightarrow n'_{\mathrm{H}} = \mathbf{\Omega} \cdot n_{\mathrm{H}} = \mathbf{\Omega} \cdot \mathbf{\Gamma} \cdot n \tag{3.26a}$$

$$\frac{\partial p(t)}{\partial t} \Longleftrightarrow p'_{\mathrm{H}} = \mathbf{\Omega} \cdot p_{\mathrm{H}} = \mathbf{\Omega} \cdot \mathbf{\Gamma} \cdot p \tag{3.26b}$$

Concerning the ECEs, time-varying unknowns are also treated following the HB technique, therefore the frequency-domain representation of terminal voltages and

currents reads:

$$v_{k\mathrm{H}} = \mathbf{\Gamma} \cdot v_k \quad \text{where} \quad v_{k\mathrm{H}}^T = [v_{k0}, v_{kc1}, v_{ks1}, v_{kc2}, v_{ks2}, ..., v_{kcN_\mathrm{H}}, v_{ksN_\mathrm{H}}]^T \tag{3.27a}$$

$$i_{k\mathrm{H}} = \mathbf{\Gamma} \cdot i_k \quad \text{where} \quad i_{k\mathrm{H}}^T = [i_{k0}, i_{kc1}, i_{ks1}, i_{kc2}, i_{ks2}, ..., i_{kcN_\mathrm{H}}, i_{ksN_\mathrm{H}}]^T \tag{3.27b}$$

The circuit impedance $\mathbf{Z}$ of the voltage-controlled equation (2.31) is already expressed in the phasor domain: each element of $\mathbf{Z}$ is expanded on n_H harmonics, hence its size increases up to $(K \cdot n_\mathrm{H}) \times (K \cdot n_\mathrm{H})$:

$$\mathbf{Z}_\mathrm{H} = \begin{pmatrix} Z_{11,\mathrm{H}} & \cdots & Z_{1K,\mathrm{H}} \\ \vdots & \ddots & \vdots \\ Z_{K1,\mathrm{H}} & \cdots & Z_{KK,\mathrm{H}} \end{pmatrix} \tag{3.28}$$

Moreover, the current equation (2.33) involves the time derivative of the electric field through the displacement current contribution of (2.34). Its HB representation follows (A.12).

3.4 Numerical implementation

The partial differential equations involved in the TCAD solver are non-linear, as a consequence their solution is not straightforward and requires the development of ad-hoc numerical methods, the one used in this case is Newton's method [55]. A generalized version of Newton's method is exploited in the in-house TCAD simulator. Consider the basic discretized PDD model equations in compact form:

$$\mathbf{F}^{(\alpha)}(u) = 0 \tag{3.29}$$

with $\alpha, u = (\phi, n, p)$, where the α index represents a specific equation of the system, for example $\alpha = \phi$ corresponds to the Poisson equation, and the u index refers the vector of unknown nodal samples, such as the electrostatic potential or the carrier concentrations [45]. The first-order Taylor expansion at the k-th iteration step is:

$$\underbrace{\mathbf{F}(u^k)}_{\mathrm{r}^k} + \underbrace{\mathbf{F}'(u^k)}_{\mathrm{J}^k} \underbrace{(u^{k+1} - u^k)}_{\Delta u^{k+1}} = 0 \Longrightarrow \mathrm{J}^k \cdot \Delta u^{k+1} = -\mathrm{r}^k \tag{3.30}$$

where J is the Jacobian matrix, containing the derivatives of each equation $\mathbf{F}^{(\phi)}$, $\mathbf{F}^{(n)}$ and $\mathbf{F}^{(p)}$ with respect to the unknowns ϕ, n and p, while Δu is the vector of unknown variations with respect to the previous step and r is the residual vector, containing the discretized physical equations of the system, which are the Poisson equation $\mathbf{F}^{(\phi)}$, the electron continuity equation $\mathbf{F}^{(n)}$ and the hole continuity equation $\mathbf{F}^{(p)}$. Therefore, at the $(k+1)$-step, the solution vector u can be updated to $u^{k+1} = u^k + \Delta u^{k+1}$. Notice that the Taylor expansion is a local approximation, since it is evaluated starting from an initial guess and it is very important to start from a reasonably good guess in order to reach convergence. This is the reason why the thermodynamic equilibrium simulation is the first step of the drift-diffusion solver, since it provides the initial guess necessary for the simulation of the full drift-diffusion model out of equilibrium. Equation (3.30) can be written as:

$$\begin{pmatrix} \mathrm{J}_{\phi\phi} & \mathrm{J}_{\phi n} & \mathrm{J}_{\phi p} \\ \mathrm{J}_{n\phi} & \mathrm{J}_{nn} & \mathrm{J}_{np} \\ \mathrm{J}_{p\phi} & \mathrm{J}_{pn} & \mathrm{J}_{pp} \end{pmatrix} \cdot \begin{pmatrix} \Delta\phi \\ \Delta n \\ \Delta p \end{pmatrix} = - \begin{pmatrix} \mathrm{r}_{\phi} \\ \mathrm{r}_{n} \\ \mathrm{r}_{p} \end{pmatrix} \tag{3.31}$$

while the residual vector is expressed as the sum of two parts:

$$\mathrm{r} = \mathrm{K} \cdot u + \mathrm{t} \Longrightarrow \begin{pmatrix} \mathrm{r}_{\phi} \\ \mathrm{r}_{n} \\ \mathrm{r}_{p} \end{pmatrix} = \begin{pmatrix} \mathrm{K}_{\phi\phi} & \mathrm{K}_{\phi n} & \mathrm{K}_{\phi p} \\ \mathrm{K}_{n\phi} & \mathrm{K}_{nn} & \mathrm{K}_{np} \\ \mathrm{K}_{p\phi} & \mathrm{K}_{pn} & \mathrm{K}_{pp} \end{pmatrix} \cdot \begin{pmatrix} \phi \\ n \\ p \end{pmatrix} + \begin{pmatrix} \mathrm{t}_{\phi} \\ \mathrm{t}_{n} \\ \mathrm{t}_{p} \end{pmatrix} \tag{3.32}$$

where matrix K and t are the linear and non-linear components, respectively, of the discretized physical equations.

Let us take into account the PDD model in *static conditions* and assume the incomplete ionization of dopants. Linear and non-linear components of the residual vector can be identified in the discretized PDD equations (3.8), (3.15) and (3.17), where time dependencies are neglected, and their boundary conditions in (3.20), (3.21) and (3.22). The residual vector and the Jacobian matrix can be written as:

$$\mathrm{r} = \mathrm{r}^{(0)} = \mathrm{K}^{(0)} \cdot u + \mathrm{t} \tag{3.33a}$$

$$\mathrm{J} = \mathrm{K}^{(0)} + \mathrm{J}^{(0)} \tag{3.33b}$$

where

$$\mathrm{K}^{(0)} = \begin{pmatrix} \mathrm{K}^{(0)}_{\phi\phi} & \mathrm{K}^{(0)}_{\phi n} & \mathrm{K}^{(0)}_{\phi p} \\ 0 & \mathrm{K}^{(0)}_{nn} & 0 \\ 0 & 0 & \mathrm{K}^{(0)}_{pp} \end{pmatrix}, \quad \mathrm{J}^{(0)} = \begin{pmatrix} 0 & \mathrm{J}^{(0)}_{\phi n} & \mathrm{J}^{(0)}_{\phi p} \\ \mathrm{J}^{(0)}_{n\phi} & \mathrm{J}^{(0)}_{nn} & \mathrm{J}^{(0)}_{np} \\ \mathrm{J}^{(0)}_{p\phi} & \mathrm{J}^{(0)}_{pn} & \mathrm{J}^{(0)}_{pp} \end{pmatrix}, \quad \mathrm{t} = \begin{pmatrix} \mathrm{t}_{\phi} \\ \mathrm{t}_{n} \\ \mathrm{t}_{p} \end{pmatrix} \tag{3.34}$$

where the superscritp (0) refers to the static components of the residual vector since time dependencies are not considered. Concerning the Jacobian matrix, it is the sum of two different parts: a *static linear part* $\mathrm{K}^{(0)}$ and a *static non-linear part* $\mathrm{J}^{(0)}$. The terms $\mathrm{J}^{(0)}_{\phi n}$ and $\mathrm{J}^{(0)}_{\phi p}$ come from the incomplete ionization of dopants (2.50), where N_{D} and N_{A} depend on the electron and hole concentrations, therefore the derivatives of t_{ϕ} with respect to the carrier concentrations must be added to the Jacobian matrix. Concerning the system's size, let us consider a device with a grid structure of n_n nodes, hence each equation of the PDD model is defined on a number of points equal to n_n. Since the system includes three equations, its dimension is $3n_n \times 3n_n$.

The analysis can be extended to the *dynamic case*, in particular to the periodic LS operating condition, where two aspects must be taken into account. First of all, time dependencies of the discretized PDD model add a *dynamic matrix component*, namely $\mathrm{K}^{(1)}$, to both the residual vector and the Jacobian matrix. This matrix represents the contribution of the time derivatives of electrons and holes in the continuity equations and it is expressed as follows:

$$\mathrm{K}^{(1)} = \begin{pmatrix} 0 & 0 & 0 \\ 0 & \mathrm{K}^{(1)}_{nn} & 0 \\ 0 & 0 & \mathrm{K}^{(1)}_{pp} \end{pmatrix} \tag{3.35}$$

Furthermore, all the matrices are assembled in the time-domain and then translated in the frequency-domain using the real notation of the HB formalism [29]. Defining a number of harmonics equal to $n_{\mathrm{H}} = 2N_{\mathrm{H}} + 1$, the system becomes:

$$\mathrm{r}_{\mathrm{H}} = \underbrace{(\mathrm{K}^{(0)}_{\mathrm{H}} + \mathrm{K}^{(1)}_{\mathrm{H}})}_{\mathrm{K}_{\mathrm{H}}} \Delta u_{\mathrm{H}} + \mathrm{t}_{\mathrm{H}} = \underbrace{\mathrm{K}^{(0)}_{\mathrm{H}}\, \Delta u_{\mathrm{H}} + \mathrm{t}_{\mathrm{H}}}_{\mathrm{r}^{(0)}_{\mathrm{H}}} + \underbrace{\mathrm{K}^{(1)}_{\mathrm{H}} \Delta u_{\mathrm{H}}}_{\mathrm{r}^{(1)}_{\mathrm{H}}} \tag{3.36a}$$

$$\mathrm{J}_{\mathrm{H}} = \mathrm{K}_{\mathrm{H}} + \mathrm{J}^{(0)}_{\mathrm{H}} \tag{3.36b}$$

where the terms Δu_{H}, t_{H}, $\mathrm{K}_{\mathrm{H}}^{(0)}$, $\mathrm{K}_{\mathrm{H}}^{(1)}$ and $\mathrm{J}_{\mathrm{H}}^{(1)}$ are converted in the frequency-domain through $\boldsymbol{\Gamma}$, $\boldsymbol{\Gamma}^{-1}$ and $\boldsymbol{\Omega}$. Each equation of the PDD model is discretized on a grid structure of n_n nodes: on each node i, a number of harmonics equal to n_{H} is defined. Therefore, taking as an example the electron continuity equation, the frequency-domain conversion is performed as follows:

$$\Delta n_{i_{\mathrm{H}}} = \boldsymbol{\Gamma}\, \Delta n_i, \qquad \mathrm{t}_{n_{i_{\mathrm{H}}}} = \boldsymbol{\Gamma}\, \mathrm{t}_{\phi_i} \tag{3.37a}$$

$$\mathrm{K}^{(0)}_{n_{i\mathrm{H}} n_{i\mathrm{H}}} = \boldsymbol{\Gamma}\, \mathrm{K}^{(0)}_{n_i n_i}\, \boldsymbol{\Gamma}^{-1}, \quad \mathrm{K}^{(1)}_{n_{i\mathrm{H}} n_{i\mathrm{H}}} = \boldsymbol{\Omega}\, \boldsymbol{\Gamma}\, \mathrm{K}^{(1)}_{n_i n_i}\, \boldsymbol{\Gamma}^{-1}, \quad \mathrm{J}^{(0)}_{n_{i\mathrm{H}} n_{i\mathrm{H}}} = \boldsymbol{\Gamma}\, \mathrm{J}^{(0)}_{n_i n_i}\, \boldsymbol{\Gamma}^{-1} \tag{3.37b}$$

In LS operating conditions the dimension of the system increases to $3N_n \times 3N_n$, where $N_n = n_n \cdot n_{\mathrm{H}}$.

If the PDD model is coupled to the ECEs, forming the PDD-ECE system, the residual vector and the Jacobian matrix are modified. In particular, in the voltage-controlled equation (2.31), one can identify two blocks: the right-hand side enters in vector t, while in the left-hand side the terminal voltage enters in $\mathrm{K}^{(0)}$ and the circuit impedance is an element of $\mathrm{K}_{\mathrm{H}}^{(2)}$. Concerning the current equation (2.33), in the left-hand side the terminal current contributes to $\mathrm{K}^{(0)}$, while the right-hand side enters in $\mathrm{K}^{(0)}$, $\mathrm{K}^{(1)}$ and $\mathrm{J}^{(0)}$, since it involves the electron, hole and displacement currents. The system becomes:

$$\mathrm{r}_{\mathrm{H}} = \mathrm{r}_{\mathrm{H}}^{(0)} + \mathrm{r}_{\mathrm{H}}^{(1)} + \mathrm{r}_{\mathrm{H}}^{(2)} \quad \text{where} \quad \mathrm{r}_{\mathrm{H}}^{(2)} = \mathrm{K}_{\mathrm{H}}^{(2)} \Delta u_{\mathrm{H}} \tag{3.38a}$$

$$\mathrm{J}_{\mathrm{H}} = \mathrm{K}_{\mathrm{H}} + \mathrm{J}_{\mathrm{H}}^{(0)} \quad \text{where} \quad \mathrm{K}_{\mathrm{H}} = \mathrm{K}_{\mathrm{H}}^{(0)} + \mathrm{K}_{\mathrm{H}}^{(1)} + \mathrm{K}_{\mathrm{H}}^{(2)} \tag{3.38b}$$

In this case, the size of the system increases: each equation is defined on n_c active terminals (not grounded) and n_{H} harmonics. Since $N_c = n_c \cdot n_{\mathrm{H}}$, the dimension of the system becomes $(3N_n + 2N_c) \times (3N_n + 2N_c)$.

3.5 Treatment of self-heating

As anticipated in Chapter 2, one of the main advanced capabilities of the in-house TCAD solver is the possibility to evaluate the heat dissipation through the device, exploiting the self-heating equation. This section is focused on the spatial and temporal discretization of the SH equation (2.36) and its numerical implementation

into the SHS system (2.38). To this purpose, (2.36) is re-written as follows:

$$Y_{\text{th}}(T - T_0) = P_{\text{diss}} \tag{3.39}$$

where the left-hand side is characterized by the lattice temperature T and the thermal admittance Y_{th}, while the right-hand side term corresponds to the FFT of the dissipated power.

Let us start from the spatial discretization procedure: the SH equation is defined on a 2D non-uniform grid structure of n_n nodes with triangular subspaces. The dissipated power in (2.37) is given by the product of time-varying voltages and currents, which are only defined on the device terminals, therefore the spatial discretization only concerns the lattice temperature $T(x,y,t)$. This term assumes the same value in all the grid nodes, providing a *uniform heat dissipation* inside the device. Nevertheless, it is not treated as a parameter, but rather as a vector defined on each node i. This choice has no obvious immediate advantages in the current code, but it will allow for an easier implementation of the heat-flow equation, when more accurate and advanced device analyses will be required. As a consequence, the discretized form of the SH equation is:

$$\sum_t \Big[(T_i - T_0) \Big] Y_{\text{th}} - P_{\text{diss}} = 0 \tag{3.40}$$

Concerning the temporal discretization, let us apply the HB formalism to the involved time-domain quantities, i.e. the lattice temperature and the dissipated power, which are divided into $n_{\text{H}} = 2N_{\text{H}} + 1$ equispaced times:

$$T(t) \Longleftrightarrow [T(t_1), T(t_2), ..., T(t_{2N_{\text{H}}+1})]^T = T^T \tag{3.41a}$$

$$p_{\text{diss}}(t) \Longleftrightarrow [p_{\text{diss}}(t_1), p_{\text{diss}}(t_2), ..., p_{\text{diss}}(t_{2N_{\text{H}}+1})]^T = p_{\text{diss}}^T \tag{3.41b}$$

The time-sampled vectors are translated in the frequency domain using the $\mathbf{\Gamma}$ matrix defined in (A.7) and (A.8), which implement a discretized Fourier transform:

$$T_{\text{H}} = \mathbf{\Gamma} \cdot T \quad \text{where} \quad T_{\text{H}}^T = [T_0, T_{c1}, T_{s1}, T_{c2}, T_{s2}, ..., T_{cN_{\text{H}}}, T_{sN_{\text{H}}}]^T \tag{3.42a}$$

$$P_{\text{diss}_{\text{H}}} = \mathbf{\Gamma} \cdot p_{\text{diss}} \ \text{ where } \ P_{\text{diss}_{\text{H}}}^T = [P_{\text{diss}_0}, P_{\text{diss}_{c1}}, ..., P_{\text{diss}_{cN_{\text{H}}}}, P_{\text{diss}_{sN_{\text{H}}}}]^T \tag{3.42b}$$

Moreover, the SH equation involves the thermal admittance Y_{th}, which is already designed in the phasor domain as an RC thermal circuit (see Fig. 2.5). The HB representation follows (A.12):

$$Y_{\text{th}} = \frac{1}{R_{\text{th}}} + \mathbf{\Omega}\, C_{\text{th}} \tag{3.43}$$

The numerical implementation of the SHS system consists of applying Newton's method to (3.40): the left-hand side involves the term Y_{th}, which enters into the matrix $\mathrm{K}_{\mathrm{H}}^{(2)}$, while the dissipated power on the right-hand side contributes to $\mathrm{J}^{(0)}$. In conclusion, the SH discretized equation is defined on $N_n = n_n \cdot n_{\text{H}}$ elements, where n_n is the number of grid nodes and n_{HJ} the number of harmonics. As a consequence, the size of the SHS system increases from $(3N_n + 2N_c) \times (3N_n + 2N_c)$ to $(4N_n + 2N_c) \times (4N_n + 2N_c)$.

3.6 Treatment of the trap rate equation

Another advanced capability of the in-house TCAD simulator is the possibility to simulate trapping and de-trapping mechanisms, coupling the PDD-ECE system to the trap rate equation. This section is focused on the spatial and temporal discretization of the TRE equation (2.42) and its numerical implementation into the PDD-ECE-TRE system (2.46).

Let us start from the spatial discretization and consider the TRE equation defined on a grid structure of n_n nodes. The involved physical quantities of (2.42), i.e. electrons $n(x,y,t)$, holes $p(x,y,t)$ and traps concentrations $n_t(x,y,t)$ depend on the grid structure, hence:

$$\sum_t \left[\frac{\partial n_{t_i}}{\partial t} - (U_{n_i} - U_{p_i}) \right] = 0 \tag{3.44}$$

where n_{t_i} is the occupied trap concentration at each node i, while U_{n_i} and U_{p_i} are functions of n_i and p_i, respectively. As a consequence, the space charge involved in the discretized Poisson equation is modified as follows:

$$\rho_i^t = q \cdot (p_i - n_i + N_{\text{D}_i} - N_{\text{A}_i} - n_{\text{t}_i}) \tag{3.45}$$

Concerning the temporal discretization, let us apply the HB formalism on the involved time-domain quantities, i.e. electrons, holes and traps concentrations, which are divided into $n_{\mathrm{H}} = 2N_{\mathrm{H}} + 1$ equispaced times:

$$n(t) \Longleftrightarrow [n(t_1), n(t_2), ..., n(t_{2N_{\mathrm{H}}+1})]^T = n^T \tag{3.46a}$$

$$p(t) \Longleftrightarrow [p(t_1), p(t_2), ..., p(t_{2N_{\mathrm{H}}+1})]^T = p^T \tag{3.46b}$$

$$n_{\mathrm{t}}(t) \Longleftrightarrow [n_{\mathrm{t}}(t_1), n_{\mathrm{t}}(t_2), ..., n_{\mathrm{t}}(t_{2N_{\mathrm{H}}+1})]^T = n_{\mathrm{t}}^T \tag{3.46c}$$

The time-sampled vectors are translated in the frequency domain using the $\mathbf{\Gamma}$ matrix:

$$n_{\mathrm{H}} = \mathbf{\Gamma} \cdot n \quad \text{where} \quad n_{\mathrm{H}}^T = [n_0, n_{c1}, n_{s1}, n_{c2}, n_{s2}, ..., n_{cN_{\mathrm{H}}}, n_{sN_{\mathrm{H}}}]^T \tag{3.47a}$$

$$p_{\mathrm{H}} = \mathbf{\Gamma} \cdot p \quad \text{where} \quad p_{\mathrm{H}}^T = [p_0, p_{c1}, p_{s1}, p_{c2}, p_{s2}, ..., p_{cN_{\mathrm{H}}}, p_{sN_{\mathrm{H}}}]^T \tag{3.47b}$$

$$n_{\mathrm{t_H}} = \mathbf{\Gamma} \cdot n_{\mathrm{t}} \quad \text{where} \quad n_{\mathrm{t_H}}^T = [n_{\mathrm{t}_0}, n_{\mathrm{t}_{c1}}, n_{\mathrm{t}_{s1}}, n_{\mathrm{t}_{c2}}, n_{\mathrm{t}_{s2}}, ..., n_{\mathrm{t}_{cN_{\mathrm{H}}}}, n_{\mathrm{t}_{sN_{\mathrm{H}}}}]^T \tag{3.47c}$$

Since the TRE also involves the time derivative of the occupied trap concentration, the latter is translated in the frequency-domain representation exploiting (A.12):

$$\frac{\partial n_{\mathrm{t}}(t)}{\partial t} \Longleftrightarrow n'_{\mathrm{t_H}} = \mathbf{\Omega} \cdot n_{\mathrm{t_H}} = \mathbf{\Omega} \cdot \mathbf{\Gamma} \cdot n_{\mathrm{t}} \tag{3.48}$$

The numerical implementation of the PDD-ECE-TRE system consists of applying Newton's method to (3.44): the time derivative of the trap concentration on the left-hand side is an element of the $\mathrm{K}^{(1)}$ matrix, while the right-hand side adds new elements to the t vector and the $\mathrm{J}^{(0)}$ matrix. The size of the PDD-ECE-TRE system increases, since the discretized TRE is defined on a grid structure of $N_n = n_n \cdot N_{\mathrm{H}}$ elements, where n_n is the number of grid points and n_{H} the number of harmonics. Moreover, the trap rate equation is solved for each trap type included in the final system, therefore it is overall defined on $N_{\mathrm{traps}} = n_{\mathrm{traps}} \cdot N_n$ elements, where n_{traps} is the number of traps included. As a consequence, the system's size increases from $(3N_n + 2N_c) \times (3N_n + 2N_c)$ to $(N_{\mathrm{traps}} + 3N_n + 2N_c) \times (N_{\mathrm{traps}} + 3N_n + 2N_c)$.

Chapter 4

Device modeling capabilities based on the Green's Function approach

4.1 Introduction

Nowadays, device variability has a central role in the fabrication process, not only in aggressively scaled technologies, such as FinFETs, UTB-SOI, but also in non-mature ones, such as GaN-based HEMTs. As explained in Chapter 1, there are different phenomena affecting the overall uncertainty of the device performance, such as process variations, related to gate length or gate thickness, the inherent spread of physical parameters, such as mobility or work function, the crystal strain and the thermal stress. The thermal management is another important consequence of extremely scaled technologies, especially in non-planar structures where heat dissipation through the substrate is a critical issue. Therefore, the electron device performances are heavily affected by the significant technological variability and the difficult thermal management, especially in analog RF and microwave applications. An efficient way to account for device performance spread is the *sensitivity analysis*, which can be performed, from the TCAD standpoint, through the linearization of the device model equations around a nominal parameter value. The proposed modeling approach is based on the so-called *Green's Function technique* (GF), well known for device noise [19, 56–58] and parametric variability analysis [17, 59], and aimed at assessing the device response to the (small) deterministic or random variation of a technological or physical parameter. In order to describe the GF approach, it is

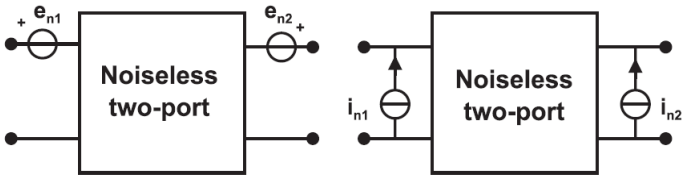

Fig. 4.1 Equivalent voltage and current noise generators applied to the terminals of a two-port noiseless device [12].

necessary to understand how the Green's functions are evaluated. The numerical estimation of the GFs is available in some commercial TCAD simulators (e.g. [26]) when the operating condition is time-invariant (DC), hence allowing only for a small-signal noise or DC variability analysis. On the other hand, the GF-based analysis in the LS dynamic case is not yet available at the commercial level, but can be performed in the in-house solver, where the numerical implementation is based on the so-called Generalized Adjoint Method.

This chapter presents the Green's Functions technique through a discussion on linear and non-linear noise analyses. In particular, the numerical implementation adopted in the in-house solver, to efficiently calculate the relevant GFs, is reported. Finally, a discussion on how the GF-based approach is applied to sensitivity analysis in both static and dynamic conditions is presented.

4.2 Linear noise analysis

Physics-based noise analysis consists of exciting the device through the so-called microscopic noise sources, representing the physical processes responsible for electronic noise. They are expressed in terms of fluctuations of carrier velocity, called diffusion noise, and carrier number, corresponding to GR noise [57, 60]. Microscopic noise sources occur inside the device, propagate to the contacts and produce current and voltage fluctuations to the device ports, which can not be neglected in circuit operation. At circuit level the overall effect of noise sources can be represented by external noise voltage or current generators applied to the terminals of a noiseless device, as shown in Fig. 4.1. They introduce fluctuations with respect to a nominal DC steady-state (small-signal noise) or with respect to a LS steady-state (large-signal noise). This section is focused on the small-signal noise analysis only. If a micro-

scopic noise fluctuation is sufficiently small, it is considered as a small perturbation around the DC working point. In this case, the device acts in linearity and the noise analysis can be carried out through the linearization of the device operation around the DC bias point, hence the name *linear noise analysis*. Since the SS noise analysis is a kind of small-signal analysis in presence of random excitation, a brief review of the TCAD approach to SS analysis is hereafter presented.

4.2.1 Small-signal analysis

Consider the compact form of of the PDD system:

$$\mathbf{F}^{(\alpha)}(\beta,\dot{\beta}) = 0 \tag{4.1}$$

with $\alpha,\beta = (\phi,n,p)$, where the α index represents a specific equation of the system, for example $\alpha = \phi$ corresponds to the Poisson equation, the β index refers the vector of unknown nodal samples, such as the electrostatic potential or the carrier concentrations, and the term $\dot{\beta}$ is the time derivative of β (it is null in memory-less equations, such as Poisson equation $\alpha = \varphi$). The external voltage source vector $\mathbf{s}_{\text{ext}}$ sets the operating regime of the device, either static or dynamic. If the device operates in small-signal conditions, an external source with small amplitude $\mathbf{s}^{ss}_{\text{ext}}(t)$ is added to a DC working point $\mathbf{s}_{\text{ext,0}}$, and the input source becomes $\mathbf{s}_{\text{ext}}(t) = \mathbf{s}_{\text{ext,0}} + \mathbf{s}^{ss}_{\text{ext}}(t)$. Therefore, the unknowns are expressed as $\beta(t) = \beta_0 + \beta^{ss}(t)$. Due to the small amplitude of the input signal, the device equations can be linearized around the DC working point. The linearized expression can be directly evaluated in the frequency domain, where no harmonics are generated, since the signal amplitude is small enough to have a linear response:

$$\beta^{ss}(t) = \tilde{\beta}^{ss}\exp(\mathrm{j}\omega t) \tag{4.2}$$

where $\tilde{\beta}^{ss}$ are the peak amplitude of the time-domain (sinusoidal) signals. The frequency-domain linearized equation is:

$$\left.\frac{\partial \mathbf{F}}{\partial \phi}\right|_0 \tilde{\phi}^{ss} + \left.\frac{\partial \mathbf{F}}{\partial n}\right|_0 \tilde{n}^{ss} + \left.\frac{\partial \mathbf{F}}{\partial p}\right|_0 \tilde{p}^{ss} + \mathrm{j}\omega \left.\frac{\partial \mathbf{F}}{\partial \dot{n}}\right|_0 \tilde{n}^{ss} + \mathrm{j}\omega \left.\frac{\partial \mathbf{F}}{\partial \dot{p}}\right|_0 \tilde{p}^{ss} = 0 \tag{4.3}$$

Applying the discretization procedure to the system of equations (4.3) on a grid structure of n_n nodes, one obtains the following frequency-domain system:

$$\mathrm{J_H} \cdot \tilde{u}^{ss} = \mathbf{s}^{ss}_{\mathrm{ext}} \tag{4.4}$$

where $\tilde{u}^{ss} = (\tilde{\phi}^{ss}, \tilde{n}^{ss}, \tilde{p}^{ss})^T$. The Jacobian matrix, as explained in Chapter 3, is equal to:

$$\mathrm{J_H} = \mathrm{K_H^{(0)}} + \mathrm{K_H^{(1)}} + \mathrm{J_H^{(0)}} = \mathrm{K^{(0)}} + j\omega\ \mathrm{K^{(1)}} + \mathrm{J^{(0)}} \tag{4.5}$$

This expression is valid since, in case of linear response, no harmonics are generated ($N_{\mathrm{H}} = 0$ and $n_{\mathrm{H}} = 1$), hence $\mathbf{\Gamma}$ and $\mathbf{\Gamma}^{-1}$ are equal to 1 and the frequency dependence is only given by the term $j\omega$. Matrices are expressed as if they were in static conditions [61], in particular $\mathrm{K^{(0)}}$ and $\mathrm{J^{(0)}}$ assume the form of (3.34) and $\mathrm{K^{(1)}}$ is equal to (3.35). As a consequence, the size of the system is $3n_n \times 3n_n$.

4.2.2 Small-signal noise analysis: the Langevin approach

Physics-based modeling of linear noise analysis consists of adding microscopic noise sources to the PDEs of the noiseless device in DC steady-state condition and obtaining Langevin equation [62]. Consider the compact form of the PDD model and apply the noise sources $\mathbf{s}$ to the right-hand side of the system, producing a perturbation of the DC solution:

$$\mathbf{F}^{(\alpha)}(\beta, \dot{\beta}) = \mathbf{s} \tag{4.6}$$

where the source $\mathbf{s}$ is not added to the boundary conditions. If the noise sources are sufficiently small, the device is in small-signal noise conditions and the system of PDEs can be linearized around a DC noiseless steady-state, leading to:

$$\left.\frac{\partial \mathbf{F}}{\partial \phi}\right|_0 \delta\phi + \left.\frac{\partial \mathbf{F}}{\partial n}\right|_0 \delta n + \left.\frac{\partial \mathbf{F}}{\partial p}\right|_0 \delta p + \left.\frac{\partial \mathbf{F}}{\partial \dot{n}}\right|_0 \delta \dot{n} + \left.\frac{\partial \mathbf{F}}{\partial \dot{p}}\right|_0 \delta \dot{p} = \mathbf{s} \tag{4.7}$$

(4.7) is the Langevin equation, which can be solved exploiting the Green's Function (GF) approach. One can define the Green's function as $G_{\alpha,\beta}(\mathbf{r}, \mathbf{r}_1; t, t_1)$ ($\alpha, \beta = \phi, n, p$) for equation α and input variable β as the response in α to a unit source $\delta(\mathbf{r} - \mathbf{r}_1)\delta(t - t_1)$ injected in β. The Green's theorem calculates the fluctuation $\delta\alpha$

induced by the source **s**:

$$\delta\alpha(\mathbf{r},t) = \sum_{\beta=\phi,n,p} \int_{\Omega} \int_{-\infty}^{t} G_{\alpha,\beta}(\mathbf{r},\mathbf{r}_1;t,t_1) s_{\beta}(\mathbf{r}_1,t_1) \mathrm{d}t_1 \mathrm{d}\mathbf{r}_1 \tag{4.8}$$

where Ω is the device volume. The device working point is a DC steady-state, therefore $G_{\alpha,\beta}(\mathbf{r},\mathbf{r}_1;t,t_1) = G_{\alpha,\beta}(\mathbf{r},\mathbf{r}_1;t-t_1)$. Since this is a time-invariant linear system, a frequency-domain analysis is possible and, through the Fourier transform, (4.8) becomes:

$$\delta\tilde{\alpha}(\mathbf{r},\omega) = \sum_{\beta=\phi,n,p} \int_{\Omega} \tilde{G}_{\alpha,\beta}(\mathbf{r},\mathbf{r}_1;\omega) \tilde{s}_{\beta}(\mathbf{r}_1,\omega) \mathrm{d}\mathbf{r}_1 \tag{4.9}$$

Notice that, in the following sections, the spatial convolution integral of (4.9) will be translated and applied in discrete form. In order to apply the GF approach to the PDD model, let us consider a noiseless device with $n_c + 1$ contacts (n_c not grounded, one grounded), where n_c active terminals are connected to external noise generators, which can be short-circuit (s.c.) noise current sources or open-circuit (o.c.) noise voltage sources. External noise sources are translated into extra equations to be added as boundary conditions of (4.7): the small-signal short-circuit condition and the small-signal open-circuit condition. (4.10a) is satisfied if a noise current generator is applied to the terminal i, therefore no potential fluctuations are allowed. This corresponds to couple the linearized PDD model to the voltage-controlled equation (2.31) in s.c. conditions. Equation (4.10b) corresponds to put a noise voltage generator to the terminal k, hence there are no current fluctuations ($\delta\tilde{\mathbf{i}}$ includes electron, hole and displacement currents). This corresponds to couple the linearized PDD model to the current equation (2.33) in o.c. conditions.

$$\delta\tilde{\mathbf{v}} = 0 \tag{4.10a}$$

$$\delta\tilde{\mathbf{i}} = 0 \tag{4.10b}$$

In conclusion, there are $n_c + 1$ boundary conditions: n_c equations correspond to the s.c. or the o.c. conditions applied to the active contacts and the last equation enforce one terminal to be grounded. In this discussion, (4.10a) is enforced on the linearized PDD system in order to evaluate the s.c. Green's Functions. With the aim of numerically evaluating them, the linearized PDD model can be discretized on a

grid structure of n_n mesh nodes, obtaining the following frequency-domain system:

$$\mathrm{J_H} \cdot \delta\tilde{u} = \mathbf{s} \tag{4.11}$$

Since the system response is linear, no harmonics are generated ($n_\mathrm{H} = 1$), the Jacobian matrix assumes the same form of the SS analysis and the size of the system is $3n_n \times 3n_n$. One way to solve this system is the so-called *direct approach*, aimed at evaluating the o.c. potential fluctuations due to a unit current injection into each internal device node. This approach is computationally inefficient since the unit source is injected on one mesh node (observation node) at a time. This procedure implies to solve $2n_n$ complex linear systems (since the analysis is in the frequency-domain) of dimension $3n_n \times 3n_n$, even though the relevant unknowns are on the contacts, hence $2n_c$. In order to efficiently evaluate the Green's functions, there are several techniques. The most general one is Branin's method [63]: originally developed for network small-change sensitivity and noise analysis, this approach can be applied to systems of discretized equations for physics-based noise analysis and represents a generalization of the Adjoint method [64, 65]. An approach suitable for any kind of discretized DD model is called *Generalized Adjoint Approach* (GAA) and was developed by Bonani et al. in 1995 [57, 66, 67].

4.2.3 The Generalized Adjoint Approach

The Generalized Adjoint Approach has different formulations according to the numerical implementation. The one adopted in the in-house TCAD code is aimed at evaluating the s.c. Green's functions concurrent with the small-signal admittance matrix [12].

Consider the linearized PDD system and the s.c. boundary condition (4.10a). The discretization procedure on a grid structure of n_n nodes leads to:

$$\begin{bmatrix} \mathbf{J}_c & \mathbf{B}_x & \mathbf{0} \\ \mathbf{0} & \mathbf{I} & \mathbf{0} \\ \mathbf{A}_x^T & \mathbf{D}_x & -\mathbf{I} \end{bmatrix} \begin{bmatrix} \mathbf{x} \\ \mathbf{v} \\ \mathbf{i} \end{bmatrix} = \begin{bmatrix} \mathbf{s}_i \\ \mathbf{s}_c \\ \mathbf{0} \end{bmatrix} \tag{4.12}$$

where $\mathbf{x}$, $\mathbf{v}$ and $\mathbf{i}$ are vectors of unknowns, where $\mathbf{x}$ corresponds to potential, electron and hole concentrations fluctuations in all the nodes, while $\mathbf{v}$ and $\mathbf{i}$ are the terminal voltages and currents, respectively. Then, there are several matrices: $\mathbf{J}_c$ is the

Jacobian matrix ($3n_n \times 3n_n$), $\mathbf{B}_x$ is a part of the Jacobian to be multiplied times $\mathbf{v}$ ($3n_n \times n_c$), $\mathbf{I}$ is the identity matrix to be multiplied times $\mathbf{i}$ ($n_c \times n_c$) and, to conclude, $\mathbf{A}_x^T$ and $\mathbf{D}_x$ are parts of the linearization to be multiplied times $\mathbf{x}$ and $\mathbf{v}$ and with dimensions $n_c \times 3n_n$ and $n_c \times n_c$, respectively.

The unit source terms are $\mathbf{s}_i$ and $\mathbf{s}_c$: $\mathbf{s}_i$ is a vector of dimension $3n_n$ with all the elements equal to zero except for the *i-th* node, which is equal to one. This source term corresponds to a unit charge density for the Poisson equation and to a unit current for the continuity equations; $\mathbf{s}_c$ is the contact voltages vector of dimension n_c with all zero elements except for the k-th contact, which is equal to 1 V. Therefore, two possible source terms are involved in the system of equations (4.12), but only one at a time can be considered in order to solve it. As a consequence, two different cases can also be distinguished in the formulation of the s.c. Green's functions. When the unit source $\mathbf{s}_i$ is applied to the internal nodes, the term $\mathbf{s}_c$ is necessarily equal to zero, hence the second set of equations becomes $\mathbf{v} = 0$ and the solution of the system leads to the calculation of the *s.c. noise contact currents* due to a unit source injection at the internal nodes. On the other side, if no internal fluctuations are considered, the source term $\mathbf{s}_i$ is equal to zero, while the vector of unit contact voltages $\mathbf{s}_c$ is involved in the system. In this case, the solution corresponds to the ratio between terminal current and voltage fluctuations, or in other words, to the *small-signal admittance matrix* $\mathbf{Y}_{SS}$.

To efficiently evaluate both the s.c Green's functions and the small-signal admittance matrix, it is convenient to solve the *transposed system*:

$$\mathbf{J}_{ex}^T \, \mathbf{y} = \mathbf{A}_{ex} \tag{4.13}$$

where

$$\mathbf{J}_{ex} = \begin{bmatrix} \mathbf{J}_c & \mathbf{B}_x \\ \mathbf{0} & \mathbf{I} \end{bmatrix}, \quad \mathbf{A}_{ex} = \begin{bmatrix} \mathbf{A}_x^T \\ \mathbf{D}_x \end{bmatrix} \tag{4.14}$$

Equation (4.13) represents the final system implemented in the in-house TCAD solver, whose solution, shown in (4.15), includes the term $\mathbf{y}_0$, corresponding to the s.c. Green's functions and the term $\mathbf{y}_1$, corresponding to the SS admittance matrix.

$$\mathbf{y} = \begin{bmatrix} \mathbf{y}_0 \\ \mathbf{y}_1 \end{bmatrix} = \begin{bmatrix} \mathbf{A}_x^T \, \mathbf{J}_c^{-1} \\ \mathbf{D}_x \, - \, \mathbf{y}_0^T \, \mathbf{B}_x \end{bmatrix} \tag{4.15}$$

The transposed system of size $(3n_n + n_c) \times (3n_n + n_c)$ is slightly bigger than (4.11), but needs to be solved n_c times instead of $2n_n$, in order to simultaneously provide *small-signal and linear noise analysis*, leading to a strong advantage in terms of computational cost.

Treatment of self-heating

In the previous sections the numerical implementation based on the GAA approach has been applied to the linearized PDD model providing the s.c. Green's Functions of the Poisson equation and the continuity equations for electrons and holes, namely respectively $\mathbf{G}_k^{(\phi)}$, $\mathbf{G}_k^{(n)}$ and $\mathbf{G}_k^{(p)}$. If the PDD model is also coupled to the SH equation, the device temperature T becomes a new unknown of (4.12) and, since it is defined on a number of mesh nodes equal to n_n, the size of the system is modified. In particular, the vector of unknowns $\mathbf{x}$ is composed of potential fluctuations, electron and hole concentrations fluctuations and temperature fluctuations in all the nodes n_n, hence its dimension increases from $3n_n$ to $4n_n$. As a consequence, the size of $\mathbf{J}_c$, $\mathbf{B}_x$ and $\mathbf{A}_x^T$ increases, respectively, to $4n_n \times 4n_n$, $4n_n \times n_c$ and $n_c \times 4n_n$. The solution of the new system provides an additional information, i.e. the Green's Function of the self-heating equation, namely $\mathbf{G}_k^{(T)}$.

Treatment of the trap rate equation

A similar treatment can be repeated if the PDD model is coupled to the TRE equation: the occupied trap concentration n_{t} becomes a new unknown of (4.12) and, since each trap is defined on a number of mesh nodes equal to n_n, the size of the system is modified. In particular, the vector of unknowns $\mathbf{x}$ is composed of potential fluctuations and electron, hole and traps concentrations fluctuations in all the nodes n_n. Its dimension increases from $3n_n$ to $n_{\mathrm{traps}} \cdot n_n + 3n_n$, where n_{traps} is the number of involved traps. As a consequence, the size of $\mathbf{J}_c$, $\mathbf{B}_x$ and $\mathbf{A}_x^T$ becomes, respectively, $(n_{\mathrm{traps}} \cdot n_n + 3n_n) \times (n_{\mathrm{traps}} \cdot n_n + 3n_n)$, $(n_{\mathrm{traps}} \cdot n_n + 3n_n) \times (n_c)$ and $(n_c) \times (n_{\mathrm{traps}} \cdot n_n + 3n_n)$. The solution of the new system provides an additional information, i.e. the Green's Function of the trap rate equation, namely $\mathbf{G}_k^{(n_{\mathrm{t}})}$.

4.3 Non-linear noise analysis

The large-signal noise analysis is described as a small microscopic perturbation, expressed in terms of diffusion noise and GR noise, around the LS steady-state. Since the perturbation is small, the linearization of the device operation around the LS steady-state working point can be carried out. The LS noise analysis can be viewed as a kind of Small-Signal-Large-Signal (SSLS) analysis, which is a particular case of the two-tone LS analysis, in presence of microscopic excitations. Therefore, a review of SSLS operating condition is hereafter presented.

4.3.1 Small-Signal-Large-Signal analysis

LS periodic or quasi-periodic operation is a device condition in which the peak-amplitude of time-varying signals is large enough to generate harmonic components or tones. Therefore, the device linearization around a DC working point is no longer valid and a complete time-varying device analysis is required. Large-signal inputs can be composed of one or two tones plus a DC working point. The input signal is strictly *periodic* when it is characterized by a *single-tone* at fundamental frequency ω_0 and all the generated harmonic frequencies are expressed as follows:

$$\omega_n = n\omega_0 \qquad n = 0, \pm 1, \pm 2, ...; \tag{4.16}$$

On the other hand, a *two-tone* LS excitation is characterized by two frequencies ω_1 and ω_2, related as follows:

$$\omega_{nm} = n\omega_1 + m\omega_2 \qquad n, m = 0, \pm 1, \pm 2, ...; \; nm = |n| + |m| \tag{4.17}$$

The operation regime is called *quasi-periodic*, when the input frequencies are incommensurate, i.e. their ratio is not a rational number. One particular case of (4.17) is the Small-Signal-Large-Signal (SSLS) regime [28], characterized by a generic LS excitation $x(t)$ (strong signal) at fundamental frequency ω_0 and a small-amplitude tone $x^{ss}(t)$ (weak signal) at $\tilde{\omega}$, which is further applied to the LS input and acts as a linear perturbation of the LS steady-state. In SSLS operating condition, the analysis is performed in two steps: first, the LS operating point $x(t)$ is calculated in order to understand the non-linear behavior of the strong signal only, then, the weak signal $x^{ss}(t)$ is added to the LS input and the non-linear system can be linearized around

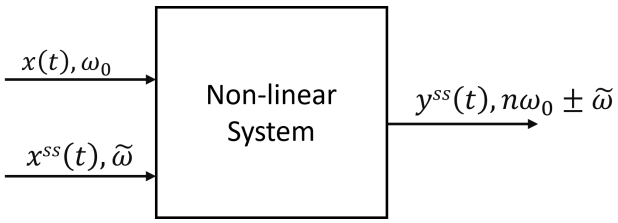

Fig. 4.2 Frequency conversion in a non-linear system characterized by a single-tone LS excitation plus a small-amplitude signal.

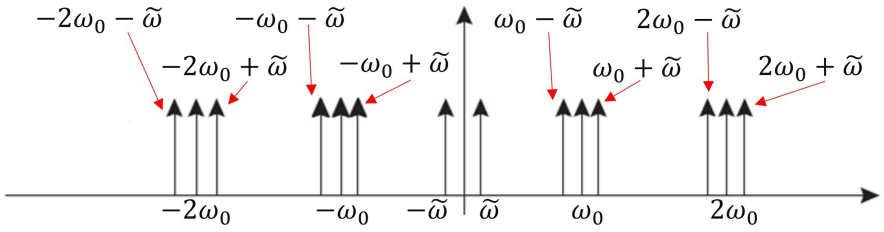

Fig. 4.3 Output spectrum of a non-linear system characterized by an input SSLS excitation.

the periodic LS steady-state. The final frequency spectrum can be written as follows:

$$\tilde{\omega}_n^{\pm} = n\omega_0 \pm \tilde{\omega} = \omega_n \pm \tilde{\omega} \qquad n = 0, \pm 1, \pm 2, \ldots \tag{4.18}$$

where ω_n is the LS tone and $\tilde{\omega}$ is the displacement frequency. Looking at Fig. 4.2, the input displacement frequency $\tilde{\omega}$ is converted into a set of output frequencies $n\omega_0 + \tilde{\omega}$ and $n\omega_0 - \tilde{\omega}$, called *sideband frequencies*, represented in Fig. 4.3. The strong signal of the SSLS input is expressed in the frequency domain using the HB formalism with the real Fourier notation (using the $\mathbf{\Gamma}$ matrix, implementing the discrete Fourier transform), therefore the spectral content is represented by (A.1). On the contrary, the weak signal is expressed through the HB technique with the more convenient complex Fourier representation (using the $\tilde{\mathbf{\Gamma}}$ matrix) [52, 28, 68, 69], reviewed in Appendix A. One can notice that in the complex notation, (4.18) is redundant and the only upper sideband frequencies are sufficient to describe the whole spectrum:

$$\tilde{\omega}_n^{+} = n\omega_0 + \tilde{\omega} \qquad n = 0, \pm 1, \pm 2, \ldots \tag{4.19}$$

Recalling (A.13), the frequency-domain expression of $x^{ss}(t)$ becomes:

$$x^{ss}(t) = \sum_{n=-N_H}^{N_H} \tilde{X}_n^{ss,+} \exp(\mathrm{j}\tilde{\omega}_n^{+} t) \tag{4.20}$$

where $\tilde{X}_n^{ss,+}$ is the complex amplitude of the upper sideband phasor, such that $\tilde{X}_{-n}^{ss,-} = (\tilde{X}_n^{ss,+})^*$ and $\tilde{X}_n^{ss,-} = (\tilde{X}_{-n}^{ss,+})^*$ for any n. Let us recall the non-linear system of Fig. 4.2: thanks to linearity, there is a linear relationship between input and output sideband amplitudes, corresponding to the so-called *conversion matrix* [28]. Since there is frequency conversion between input and output sidebands, this matrix is not diagonal. Therefore, exploiting the complex HB notation just described, one can write:

$$\tilde{Y}^{ss,+} = C(\tilde{\omega}) \cdot \tilde{X}^{ss,+} \tag{4.21}$$

where $C(\tilde{\omega})$ is the conversion matrix of the upper sideband complex amplitudes[1].

In order to introduce the numerical implementation of the SSLS analysis in the TCAD simulations, let us consider the compact form of the PDD system (4.1): each model unknown can be expressed by $x(t) = x_0(t) + x^{ss}(t)$, where $x_0(t)$ is the unperturbed LS steady-state solution and $x^{ss}(t)$ is a small perturbation. First, the discretized PDD model is solved in LS conditions following (3.36) and (3.37), as already explained in Chapter 3. Then, the linearization of the resulting system is performed around the LS steady-state leading to a generalization of (4.3) and, consequently, the discretization procedure on a grid structure of n_n mesh nodes gives system (4.4). The difference with respect to the SS system lies in the generation of harmonics: each unknown of $\tilde{u}^{ss}$ is expanded in the complex frequency domain following (4.20) and each submatrix of the Jacobian is expressed following (4.21) and leading to a conversion matrix formulation:

$$C_{\mathrm{J}} \cdot \tilde{U}^{ss,+} = \tilde{\mathbf{S}}_{\mathrm{ext}}^{ss,+} \tag{4.22}$$

For example, the submatrix $\mathrm{J}_{\phi\phi}$ is converted as follows:

$$\left(C_{\mathrm{J}_{\phi\phi}}\right)_{q,n} = \left(\mathrm{J}_{\phi\phi}\right)_{q-n} \tag{4.23}$$

where q, n are the sideband indices and $C_{\mathrm{J}_{\phi\phi}}$ becomes a matrix of matrices, as shown in Fig. 4.4. Equation (4.23) implies that the conversion matrix is arranged as a *Toeplitz matrix* [12]. Moreover, the elements of the Jacobian matrix involving time derivatives, previously expressed as $j\omega$, are now treated following (A.25). The

[1] A similar expression can be written for the lower sideband amplitudes: $\tilde{Y}^{ss,-} = C^{-}(\tilde{\omega}) \cdot \tilde{X}^{ss,-}$, where $C^{-}(\tilde{\omega}) = C(-\tilde{\omega})$.

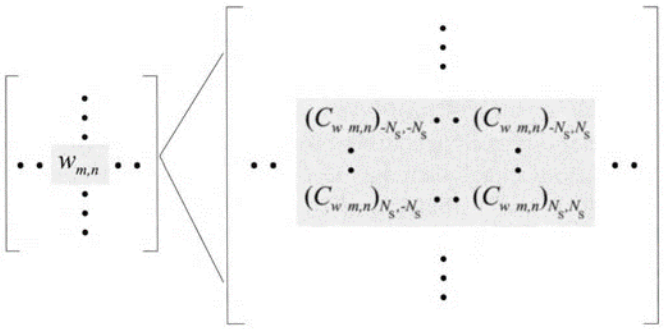

Fig. 4.4 Representation of matrix expansion in frequency-domain [13].

system's size of the SSLS system is $3N_n \times 3N_n$, hence the one found for the SS analysis multiplied by a factor $n_{\mathrm{H}} = 2N_{\mathrm{H}} + 1$. In fact $N_n = n_{\mathrm{H}} \cdot n_n$ and $N_c = n_{\mathrm{H}} \cdot n_c$.

4.3.2 Large-Signal noise analysis

LS noise analysis or non-linear analysis consists of exciting the noiseless device through microscopic fluctuations, expressed in terms of carrier number or carrier velocity, when it operates in LS conditions. The adopted approach is an extension of the linear noise analysis, described in the previous section, to the frequency-domain and implies the application of the conversion matrix formalism, introduced for the SSLS noiseless analysis.

The efficient numerical implementation based on the GAA and formulated for the linear noise analysis, can be extended to the non-linear case. To this purpose, the solution of the *transposed system* allows to simultaneously perform both *SSLS and non-linear noise analysis*: when a unit source is injected into the internal nodes, the *s.c. Conversion Green's functions* are calculated, while when a unit voltage source is applied to the terminals, the *small-signal-large-signal admittance matrix* $\mathbf{Y}_{SSLS}$ is obtained. In order to evaluate these quantities, the transposed system (4.13) is extended to the non-linear case: each unknown is expanded with the complex HB notation following (4.20) and each submatrix of the Jacobian is treated as shown in (4.23). The resulting system is:

$$C_{\mathbf{J}_{ex}^T} = \tilde{\mathbf{Y}}^{ss,+}\, C_{\mathbf{A}_{ex}} \Longrightarrow \begin{bmatrix} C_{\mathbf{J}_c} & \mathbf{0} \\ C_{\mathbf{B}_x} & \mathbf{I} \end{bmatrix} = \begin{bmatrix} \tilde{\mathbf{Y}}_0{}^{ss,+} \\ \tilde{\mathbf{Y}}_1{}^{ss,+} \end{bmatrix} \begin{bmatrix} C_{\mathbf{A}_x^T} \\ C_{\mathbf{D}_x} \end{bmatrix} \tag{4.24}$$

whose solution is:

$$\mathbf{y} = \begin{bmatrix} \tilde{\mathbf{Y}}_0^{ss,+} \\ \tilde{\mathbf{Y}}_1^{ss,+} \end{bmatrix} = \begin{bmatrix} C_{\mathbf{A}_x^T} \, C_{\mathbf{J}_c^{-1}} \\ C_{\mathbf{D}_x} - \tilde{\mathbf{Y}}_0^{ss,+} \, C_{\mathbf{B}_x} \end{bmatrix} \tag{4.25}$$

where $\tilde{\mathbf{Y}}_0^{ss,+}$ corresponds to the s.c. Conversion Green's functions and $\tilde{\mathbf{Y}}_1^{ss,+}$ corresponds to the small-signal-large signal admittance matrix. The system's size becomes $(3N_n + N_c) \times (3N_n + N_c)$ where $N_n = n_{\mathrm{H}} \cdot n_n$ and $N_c = n_{\mathrm{H}} \cdot n_c$, and the number of back-substitutions (i.e. the number of times the transposed system must be solved) becomes $2N_c$.

Treatment of self-heating

The SSLS and non-linear noise analysis applied to the linearized PDD model provides the s.c. Conversion Green's Functions of the Poisson equation and the continuity equations for electrons and holes, namely respectively $\tilde{\mathbf{G}}_k^{(\phi)}$, $\tilde{\mathbf{G}}_k^{(n)}$ and $\tilde{\mathbf{G}}_k^{(p)}$. Coupling the PDD model to the SH equation, the device temperature T becomes a new unknown of (4.24) and, since it is defined on n_n mesh nodes and n_{H} harmonics, its dimension is equal to $N_n = n_{\mathrm{H}} \cdot n_n$. As a consequence, the size of each vector/matrix involved in the system increases: the vector of unknowns $\mathbf{x}$ has dimension $4N_n$, while the size of $\mathbf{J}_c$, $\mathbf{B}_x$ and $\mathbf{A}_x^T$ increases, respectively, to $4N_n \times 4N_n$, $4N_n \times N_c$ and $N_c \times 4N_n$. The solution of the new system provides an additional information, i.e. the Conversion Green's Function of the self-heating equation, namely $\tilde{\mathbf{G}}_k^{(T)}$.

Treatment of the trap rate equation

If the PDD model is coupled to the TRE equation, the occupied trap concentration n_{t} becomes a new unknown of (4.24): each trap is defined on n_n grid points and n_{H} harmonics, vector n_{t} has dimension $n_{\mathrm{traps}} \cdot N_n$, where n_{traps} is the number of involved traps. Therefore, the size of the system is modified: the vector of unknowns $\mathbf{x}$, composed of potential fluctuations and electron, hole and traps concentrations fluctuations, increases from $3N_n$ to $n_{\mathrm{traps}} \cdot N_n + 3N_n$, while the size of $\mathbf{J}_c$, $\mathbf{B}_x$ and $\mathbf{A}_x^T$ becomes, respectively, $(n_{\mathrm{traps}} \cdot N_n + 3N_n) \times (n_{\mathrm{traps}} \cdot N_n + 3N_n)$, $(n_{\mathrm{traps}} \cdot N_n + 3N_n) \times (N_c)$ and $(N_c) \times (n_{\mathrm{traps}} \cdot N_n + 3N_n)$. The solution of the new system provides the Conversion Green's Function of the trap rate equation, namely $\tilde{\mathbf{G}}_k^{(n_{\mathrm{t}})}$.

4.4 GF approach to sensitivity analysis

The GF technique, largely used for device noise analysis, can be exploited to calculate the parametric sensitivity, i.e. the device response to a (small) variation of physical or technological parameters from a nominal condition. The approach allows to calculate the current variation at terminals and, consequently, to extract the *local sensitivity*, showing the parts of the device where the varied physical/technological parameter influences most the device behavior and contributes more to the final terminal current variation. Another important characteristic of the GF technique is the possibility to calculate those terminal currents without repeated simulations, leading to an important advantage from the computational point of view.

In this thesis, the GF-based sensitivity analysis has been implemented, exploiting the in-house TCAD solver, in both static and dynamic regimes, in particular in DC, AC and LS conditions. The parametric sensitivity has been performed to account for temperature variations [70]: T is considered a model parameter, in case of parametric temperature variations, and a model unknown, in case of heat dissipation due to the presence of a thermal impedance. The latter case implies the solution of the SHS system, where the device is coupled to an external thermal circuit for self-heating. Furthermore, the GF technique is also exploited to compute the sensitivity of trap physical parameters, e.g. the trap concentration, trap energy and trap cross section.

The following sections report a detailed discussion of the parametric sensitivity analysis in different operating conditions. Concerning the temperature, the T-dependent analysis is presented in DC and LS conditions, while the self-heating analysis is, at present, introduced in DC conditions. Regarding the sensitivity analysis in presence of traps, it is presented in both DC and AC regimes.

4.4.1 T-dependent sensitivity analysis

The T-dependent sensitivity analysis is presented in both static (DC) and LS conditions, exploiting the GF-based technique. In this discussion, T is assumed to be uniform at the device and equal to the lattice temperature (see Fig. 2.4). Hence, T is not a model unknown, but rather a model parameter.

DC analysis

Let us consider a bipolar device physics-based model expressed and re-write the discretized PDE system (4.1) in the following way:

$$\mathbf{F}^{(\alpha)}(\beta, \mathbf{v}_{\text{ext}}; T) = \mathbf{D}^{(\alpha)}\dot{\beta}. \tag{4.26}$$

with $\alpha, \beta = (\phi, n, p, n_{\text{t}})$. The term α represents a specific equation of the system, while β the vector of unknown nodal samples. For each discretized equation α, one can distinguish a time-invariant part $\mathbf{F}^{(\alpha)}(\beta, \mathbf{v}_{\text{ext}}; T)$ and a time-varying (memory) part, proportional to $\dot{\beta}$ (the time derivative of β) through the block diagonal matrix $\mathbf{D}^{(\alpha)}$ (notice that $\mathbf{D}^{(\alpha)}$ is null for memory-less equations, such as Poisson equation $\alpha = \varphi$). The external voltage source[2] vector $\mathbf{v}_{\text{ext}}$ sets the operating regime of the device, either static or dynamic.

In the static case the external voltage is constant (DC bias), and thus $\mathbf{D}^{(\alpha)} = \mathbf{0}$. The "cold" solution β_0 is found solving (4.26) for each DC bias at the nominal lattice temperature T_0. When the temperature undergoes a variation $\Delta T = T - T_0$ with fixed electrical excitation, (4.26) is linearized around the nominal solution, yielding for the perturbation $\Delta\beta = \beta - \beta_0$:

$$\mathbf{J}^{(\alpha)}(\beta_0, \mathbf{v}_{\text{ext}}; T_0)\Delta\beta + \left.\frac{\partial \mathbf{F}^{(\alpha)}}{\partial T}\right|_{(\beta_0, \mathbf{v}_{\text{ext}}; T_0)} \Delta T = 0 \tag{4.27}$$

where $\mathbf{J}^{(\alpha)}$ is the Jacobian matrix of $\mathbf{F}^{(\alpha)}$ evaluated at the nominal solution $(\beta_0, \mathbf{v}_{\text{ext}}; T_0)$. Let us define the equivalent source:

$$\mathbf{s}_0^{(\alpha)}(\beta_0, \mathbf{v}_{\text{ext}}; T_0, T) = -\left.\frac{\partial \mathbf{F}^{(\alpha)}}{\partial T}\right|_{(\beta_0, \mathbf{v}_{\text{ext}}; T_0)} \Delta T \tag{4.28}$$

which depends on both the nominal and varied temperature and represents a *distributed perturbation* for the linearized equation α, depending on the position inside the device through β_0 and T. Therefore, (4.27) can be re-written as:

$$\mathbf{J}^{(\alpha)}(\beta_0, \mathbf{v}_{\text{ext}}; T_0)\Delta\beta - \mathbf{s}_0^{(\alpha)}(\beta_0, \mathbf{v}_{\text{ext}}; T_0, T) = 0 \tag{4.29}$$

[2]Here the case of a voltage-driven device is considered. The extension to current driven terminals is obvious.

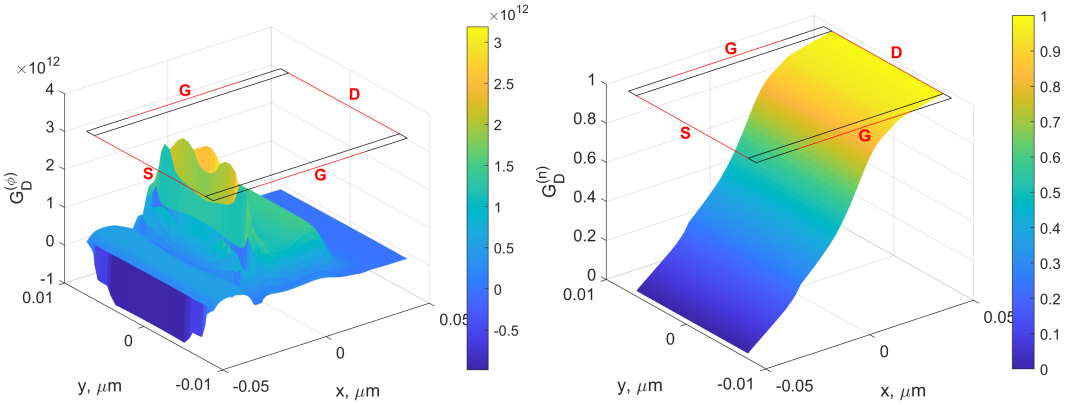

(a) GF of the Poisson equation.

(b) GF of the electron continuity equation.

Fig. 4.5 Green's Function at drain contact at $V_{\mathrm{D}} = 1$ V and $V_{\mathrm{G}} = 1$ V.

The equivalent source gives rise to a current variation $\Delta i_k^T = i_k(T) - i_k(T_0)$ at the k-th terminal that can be efficiently computed via the GF approach by the discretized spatial convolution integral obtained from (4.9):

$$\Delta i_k^T = \sum_{\alpha} \mathbf{G}_k^{(\alpha)}(\beta_0, \mathbf{v}_{\mathrm{ext}}; T_0)\, \mathbf{s}_0^{(\alpha)}(\beta_0, \mathbf{v}_{\mathrm{ext}}; T_0, T)\, \boldsymbol{\Omega} \tag{4.30}$$

where the row vector of the Green's Function nodal values $\mathbf{G}_k^{(\alpha)}(\beta_0, \mathbf{v}_{\mathrm{ext}}; T_0)$ relates the observation variable i_k^T to a unit source in each mesh node of equation α, while $\boldsymbol{\Omega}$ is a diagonal matrix containing the nodal Vornoi volumes. Fig. 4.5 shows two examples of Green's function distributions at drain contact associated to electrostatic potential (Fig. 4.5a) and electron concentration (Fig. 4.5b). GFs are evaluated from DC simulations performed at $T_0 = 300$ K on a 54 nm Si FinFET device at $V_{\mathrm{D}} = 1$ V and $V_{\mathrm{G}} = 1$ V.

The estimation of the source term (4.28) requires to compute the derivatives of the discretized physical equations with respect to T. This procedure is quite complicated, as lattice temperature enters essentially in the analytical formulation of every physical model parameter and in the Bernoulli functions of the Scharfetter-Gummel discretization scheme of the current continuity equations, as already seen in Chapter 2 and 3. Therefore, the analytical Jacobian in (4.28) is approximated through finite differences as:

$$\mathbf{s}_0^{(\alpha)}(\beta_0, \mathbf{v}_{\mathrm{ext}}; T_0, T) \simeq -\mathbf{F}^{(\alpha)}(\beta_0, \mathbf{v}_{\mathrm{ext}}; T) + \cancelto{0}{\mathbf{F}^{(\alpha)}(\beta_0, \mathbf{v}_{\mathrm{ext}}; T_0)} \tag{4.31}$$

where the last term is null in the nominal solution. This corresponds to evaluate the residual function $\mathbf{F}^{(\alpha)}$ at the varied temperature T. The computation is very fast, no matrix storage is required and the accuracy is good if T is not too far from T_0.

The GF approach opens the way to device optimization through the analysis of the so-called *local variations* and of the device *thermal sensitivity*. The nodal local variation source allows to identify which regions of the device are most affected by the equivalent source and corresponds to the integrand function of (4.30), associated to equation α at the k-th terminal, and

$$\mathrm{LS}_k^{(\alpha)} = \mathbf{G}_k^{(\alpha)}(\beta_0, \mathbf{v}_{\mathrm{ext}}; T_0)\, \mathbf{s}_0^{(\alpha)}(\beta_0, \mathbf{v}_{\mathrm{ext}}; T_0, T) \tag{4.32}$$

In addition, the device thermal sensitivity in the DC case is defined as:

$$S_{i_k}^T = \frac{\partial i_k^T}{\partial T} \approx \Delta i_k^T\big|_{T=T_0+1\ \mathrm{K}} \tag{4.33}$$

Dynamic, periodically time-varying analysis

In the dynamic case, time derivatives in (4.26) must be taken into account, thus making (4.26) a dynamical system. Consider a periodic or quasi-periodic external source $\mathbf{v}_{\mathrm{ext}}(t)$, so that the system steady-state becomes periodically time-varying and treated exploiting the HB technique. Let us denote with $\tilde{\beta}$ and $\tilde{\mathbf{F}}^{(\alpha)}$ the vector of the Fourier (harmonic) amplitudes of the time-varying functions β and $\mathbf{F}^{(\alpha)}$, truncated to the harmonic order n_{H}. The Fourier-transformed system (4.26) reads [19]:

$$\tilde{\mathbf{F}}^{(\alpha)}(\tilde{\beta}, \tilde{\mathbf{v}}_{\mathrm{ext}}; T) = \boldsymbol{\Omega}^{(\alpha)}\tilde{\beta}. \tag{4.34}$$

where $\boldsymbol{\Omega}^{(\alpha)}$ is a block-diagonal matrix of (A.12) including the dependence on the fundamental frequency ω_0 and on its harmonics $\omega_n = n\omega_0$ ($n = 1, 2, \ldots, n_{\mathrm{H}}$) and $\tilde{\mathbf{v}}_{\mathrm{ext}}$ is the Fourier transform of $\mathbf{v}_{\mathrm{ext}}(t)$. The solution of the above algebraic system yields the Fourier coefficients $\tilde{\beta}_0$ of the LS steady-state periodic solution β_0, with nominal temperature T_0.

When the temperature undergoes a variation, (4.26) must be linearized around $(\beta_0, \mathbf{v}_{\mathrm{ext}}; T_0)$, giving rise to a linear periodically time-varying (LPTV) system. LPTV systems can be analyzed in the frequency domain with the sideband frequency conversion analysis [28]: the variation is in general characterized by a set of *sidebands*

of the LS harmonics $\tilde{\omega}_n = \omega_n \pm \tilde{\omega}$, as discussed in Section 4.3, but in the particular case of a time-invariant perturbation the sidebands collapse onto the unperturbed frequencies, therefore $\tilde{\omega} = 0$ and $\tilde{\omega}_n = \omega_n$. In this case the lattice temperature is, thus, considered a static perturbation of the LS state, hence it is characterized by the same set of frequencies as the unperturbed solution. With this assumption, the frequency-domain linearized system is [19]:

$$\tilde{\mathbf{J}}^{(\alpha)}(\tilde{\beta}_0, \tilde{\mathbf{v}}_{\text{ext}}; T_0)\Delta\tilde{\beta} - \mathbf{\Omega}^{(\alpha)}\Delta\tilde{\beta} = \tilde{\mathbf{s}}_0^{(\alpha)}(\tilde{\beta}_0, \tilde{\mathbf{v}}_{\text{ext}}; T_0, T) \tag{4.35}$$

where: $\Delta\tilde{\beta} = \tilde{\beta} - \tilde{\beta}_0$ is the effect of the temperature variation ΔT; $\tilde{\mathbf{J}}^{(\alpha)}$ is the Jacobian conversion matrix, built with the Fourier coefficients of the time-periodic function $\mathbf{J}^{(\alpha)}(\beta_0, \mathbf{v}_{\text{ext}}; T_0) = \partial\mathbf{F}^{(\alpha)}/\partial\beta$ calculated in the periodic solution β_0 and at T_0. The source term $\tilde{\mathbf{s}}_0^{(\alpha)}$ collects the Fourier coefficients of:

$$\mathbf{s}_0^{(\alpha)}(\beta_0, \mathbf{v}_{\text{ext}}; T_0, T) = -\frac{\partial\mathbf{F}^{(\alpha)}(\beta, \mathbf{v}_{\text{ext}}; T)}{\partial T}\Delta T \tag{4.36}$$

extending (4.28) to the periodic case. As in the static case, a finite difference approximation avoids the explicit calculation of the temperature derivatives:

$$\tilde{\mathbf{s}}_0^{(\alpha)}(\tilde{\beta}_0, \tilde{\mathbf{v}}_{\text{ext}}; T_0, T) \simeq -\tilde{\mathbf{F}}^{(\alpha)}(\tilde{\beta}_0, \tilde{\mathbf{v}}_{\text{ext}}; T) \tag{4.37}$$

The temperature variation ΔT induces a perturbation of the terminal current at each device contact k, with spectral amplitudes $\Delta\tilde{\mathbf{I}}_k^T = \tilde{\mathbf{I}}_k(T) - \tilde{\mathbf{I}}_k(T_0)$. The Conversion Green's Functions of the linearized system (4.35), matrices denoted as $\tilde{\mathbf{G}}_k^{(\alpha)}(\tilde{\beta}_0, \tilde{\mathbf{v}}_{\text{ext}}; T_0)$, allow to compute such current variations extending (4.30) to the large-signal case:

$$\Delta\tilde{\mathbf{I}}_k^T = \sum_{\alpha} \tilde{\mathbf{G}}_k^{(\alpha)}(\tilde{\beta}_0, \tilde{\mathbf{v}}_{\text{ext}}; T_0)\,\tilde{\mathbf{s}}_0^{(\alpha)}(\tilde{\beta}_0, \tilde{\mathbf{v}}_{\text{ext}}; T_0, T)\tilde{\mathbf{\Omega}} \tag{4.38}$$

where $\tilde{\mathbf{\Omega}}$ is a block diagonal matrix containing the Vornoi volumes. Figs. 4.6 and 4.7 show two examples of Conversion Green's function distributions at drain contact associated to the third harmonic of electrostatic potential and electron concentration, respectively. CGFs are calculated from LS simulations performed at $T_0 = 300$ K on a 54 nm Si FinFET Class A power amplifier with 70 GHz operating frequency, $N_{\text{H}} = 10$ harmonics and $P_{\text{av}} = -3$ dBm available power. Furthermore, the integrand function of (4.38) defines the nodal *local variation source* of equation α at the k-th

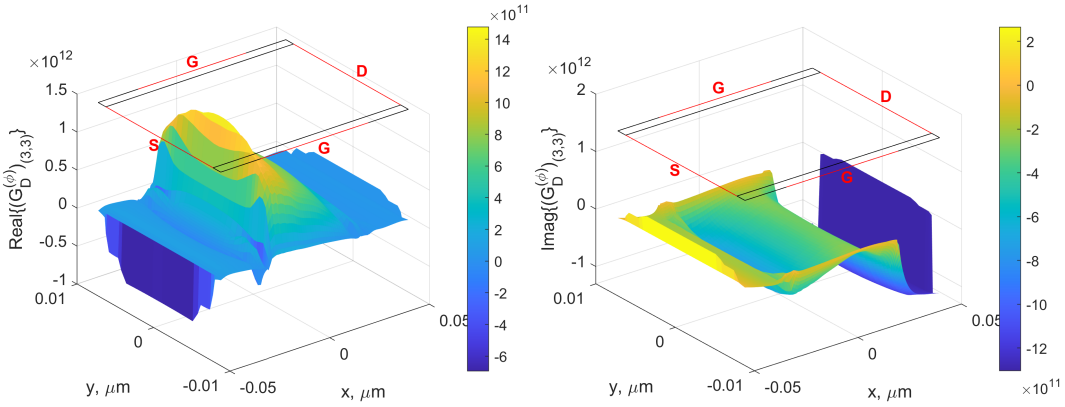

(a) Real part of $(\tilde{\mathbf{G}}_{\mathrm{D}}^{(\phi)})_{(3,3)}$. (b) Imaginary part of $(\tilde{\mathbf{G}}_{\mathrm{D}}^{(\phi)})_{(3,3)}$.

Fig. 4.6 Green's Function of the Poisson equation for the drain contact at the third harmonic input/output in a 54 nm Si FinFET power amplifier. DC bias: $V_{\mathrm{D}} = 0.6$ V and $V_{\mathrm{G}} = 0.675$ V.

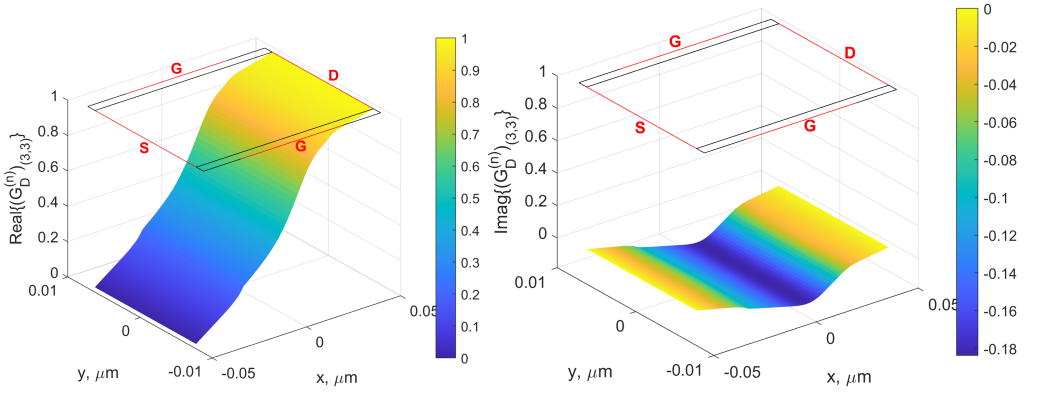

(a) Real part of $(\tilde{\mathbf{G}}_{\mathrm{D}}^{(n)})_{(3,3)}$. (b) Imaginary part of $(\tilde{\mathbf{G}}_{\mathrm{D}}^{(n)})_{(3,3)}$.

Fig. 4.7 Green's Function of the electron continuity equation for the drain contact at the third harmonic input/output in a 54 nm Si FinFET power amplifier. DC bias: $V_{\mathrm{D}} = 0.6$ V and $V_{\mathrm{G}} = 0.675$ V.

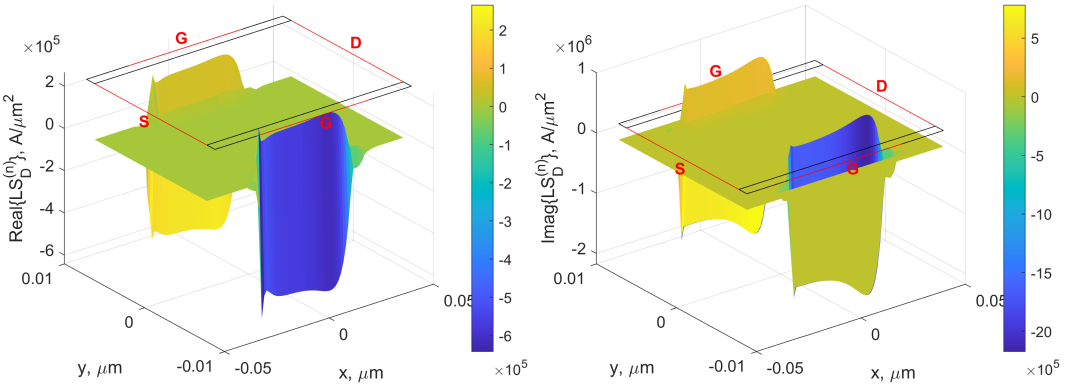

(a) Real part of $\tilde{\mathrm{LS}}_{\mathrm{D}}^{(n)}$. (b) Imaginary part of $\tilde{\mathrm{LS}}_{\mathrm{D}}^{(n)}$.

Fig. 4.8 Distributed local variation source of the third harmonic of the electron continuity equation at drain contact in a 54 nm Si FinFET power amplifier. DC bias: $V_{\mathrm{D}} = 0.6$ V and $V_{\mathrm{G}} = 0.675$ V.

terminal:

$$\tilde{\mathrm{LS}}_k^{(\alpha)} = \tilde{\mathbf{G}}_k^{(\alpha)}(\tilde{\beta}_0, \tilde{\mathbf{v}}_{\mathrm{ext}}; T_0)\, \tilde{\mathbf{s}}_0^{(\alpha)}(\tilde{\beta}_0, \tilde{\mathbf{v}}_{\mathrm{ext}}; T_0, T) \tag{4.39}$$

Fig. 4.8 shows an example of real and imaginary parts of the distributed local source calculated for a temperature variation of 5 K ($T_0 = 300$ K and $T = 305$ K) on the Si FinFET power amplifier simulated in the same conditions.

In conclusion, the device *thermal sensitivity* is a generalization of (4.33) using (4.38).

4.4.2 Self-heating sensitivity analysis

Let us now consider the device embedded into an external structure, through which heat is dissipated towards a heat sink at temperature T_0 [71]. The lattice temperature T is considered a model unknown and, as explained in Chapter 2, the device is isothermal and the heat dissipation process can be represented by a lumped thermal impedance (see Fig. 2.5).

The self-heating sensitivity analysis is aimed at evaluating the device temperature increase through the same GFs exploited for the T-dependent analysis. In this discussion, let us consider the static case only: the thermal capacitance is null and only the effect of the thermal resistance R_{th} is taken into account.

DC analysis

With a DC external voltage $v_{0,k}$ at terminal k, the device self-heating leads to a temperature increase ΔT, which can be expressed re-writing (2.36):

$$\Delta T = T - T_0 = R_{\text{th}}\, P_{\text{diss}} = R_{\text{th}} \sum_k i_k(T_0, T) v_{0,k} \tag{4.40}$$

where the k-th terminal current is dependent on both T_0 and T and can be approximated by a first order Taylor expansion around the "cold" condition ($T = T_0$, $R_{\text{th}} = 0$, $i_k = i_{0,k}$):

$$i_k\,(T_0, T) = i_k\,(T_0, T_0 + \Delta T) \simeq i_{0,k}(T_0) + S^T_{i_k}\,(T - T_0) \tag{4.41}$$

where $S^T_{i_k}$ is the thermal sensitivity (4.33). Plugging this expression into (2.36):

$$i_k\,(T_0, T) \approx i_{0,k}(T_0) + S^T_{i_k} R_{\text{th}} \sum_j i_j\,(T_0, T)\, v_{0,j} \tag{4.42}$$

which represents a linear system of equations allowing to extract i_k at all terminals. In the simpler case where $v_{0,j} = 0$ or $i_{0,j} = 0$ for $j \neq k$ (a relevant example is the case of FETs where, neglecting gate leakage, the only dissipation is through the drain), the current $i_k\,(T_0, T)$ becomes:

$$i_k\,(T_0, T) = \frac{i_{0,k}(T_0)}{1 - S^T_{i_k} R_{\text{th}} v_{0,k}} \tag{4.43}$$

If T_0 is not simply the heat sink temperature, but rather a reference temperature conveniently selected to evaluate the thermal resistance (e.g., the temperature of the foot of the fin in a FinFET device), it can be in turn subject to fluctuations, either deterministic or statistical. To account for a variation ΔT_0, the "cold" current $i_{0,k}$ is further linearized with respect to T_0, exploiting again the thermal sensitivity (4.33):

$$i_{0,k}(T_0 + \Delta T_0) \simeq i_{0,k}(T_0) + S^T_{i_k} \Delta T_0 \tag{4.44}$$

Substituting into (4.43), the final expression is:

$$i_k\,(T_0 + \Delta T_0, T) = \frac{i_{0,k}(T_0)}{1 - S^T_{i_k} R_{\text{th}} v_{0,k}} + \frac{S^T_{i_k} \Delta T_0}{1 - S^T_{i_k} R_{\text{th}} v_{0,k}} \tag{4.45}$$

Therefore, both self-heating and reference T variations only require the computation of the device currents and of their thermal sensitivities at the "cold" temperature T_0.

4.4.3 Trap-based sensitivity analysis

The GF-based sensitivity analysis in presence of traps consists of varying a trap model parameter σ, such as trap energy, cross section, total concentration. In this discussion, let us consider both the DC and the AC regimes.

DC analysis

Consider the discretized PDD-TRE system in compact form:

$$\mathbf{F}^{(\alpha)}(\beta, \mathbf{v}_{\text{ext}}; \sigma) = \mathbf{D}^{(\alpha)}\dot{\beta}. \tag{4.46}$$

with $\alpha, \beta = (\phi, n, p, n_{\text{t}})$. The term α represents a specific equation of the system, while β the vector of unknown nodal samples. For each discretized equation α, one can distinguish a time-invariant part $\mathbf{F}^{(\alpha)}(\beta, \mathbf{v}_{\text{ext}}; \sigma)$ and a memory part, proportional to $\dot{\beta}$ through the block diagonal matrix $\mathbf{D}^{(\alpha)}$. The discretized model equations depend explicitly on the external voltage $\mathbf{v}_{\text{ext}}$ and the static trap model parameter σ.

In case of DC external voltage $\mathbf{v}_{\text{ext}}$, $\mathbf{D}^{(\alpha)} = \mathbf{0}$ and the nominal solution β_0 is found solving (4.46) for each DC bias at σ_0. When σ undergoes a time-independent variation $\Delta\sigma = \sigma - \sigma_0$, (4.46) is linearized around the nominal solution, yielding for the perturbation $\Delta\beta = \beta - \beta_0$:

$$\mathbf{J}^{(\alpha)}(\beta_0, \mathbf{v}_{\text{ext}}; \sigma_0)\Delta\beta = \mathbf{s}_0^{(\alpha)}(\beta_0, \mathbf{v}_{\text{ext}}; \sigma_0, \sigma) \tag{4.47}$$

where $\mathbf{J}^{(\alpha)} = \partial\mathbf{F}^{(\alpha)}/\partial\beta$ is the Jacobian matrix of $\mathbf{F}^{(\alpha)}$ evaluated at the nominal solution $(\beta_0, \mathbf{v}_{\text{ext}}; \sigma_0)$. Let us define the equivalent source:

$$\mathbf{s}_0^{(\alpha)}(\beta_0, \mathbf{v}_{\text{ext}}; \sigma_0, \sigma) = -\left.\frac{\partial\mathbf{F}^{(\alpha)}}{\partial\sigma}\right|_{(\beta_0, \mathbf{v}_{\text{ext}}; \sigma_0)} \Delta\sigma \tag{4.48}$$

which depends on both the nominal and varied trap model parameter and represents a *distributed perturbation* for the linearized equation α, depending on the position inside the device through β_0 and σ. As for the T-dependent sensitivity analysis, a

finite difference approximation avoids the explicit calculation of the σ derivatives:

$$\mathbf{s}_0^{(\alpha)}(\beta_0, \mathbf{v}_{\text{ext}}; \sigma_0, \sigma) \simeq -\mathbf{F}^{(\alpha)}(\beta_0, \mathbf{v}_{\text{ext}}; \sigma) \tag{4.49}$$

The equivalent source gives rise to a current variation $\Delta i_k^\sigma = i_k(\sigma) - i_k(\sigma_0)$ at the k-th terminal that can be efficiently computed via the GF approach by the discretized spatial convolution integral obtained from (4.9):

$$\Delta i_k^\sigma = \sum_\alpha \mathbf{G}_k^{(\alpha)}(\beta_0, \mathbf{v}_{\text{ext}}; \sigma_0)\, \mathbf{s}_0^{(\alpha)}(\beta_0, \mathbf{v}_{\text{ext}}; \sigma_0, \sigma)\, \boldsymbol{\Omega} \tag{4.50}$$

where the row vector of the Green's Function nodal values $\mathbf{G}_k^{(\alpha)}(\beta_0, \mathbf{v}_{\text{ext}}; \sigma_0)$ relates the observation variable i_k^σ to a unit source in each mesh node of equation α, while $\boldsymbol{\Omega}$ is a diagonal matrix containing the nodal Vornoi volumes.

AC analysis

Consider the discretized PDD-TRE system in compact Fourier-transformed form:

$$\tilde{\mathbf{F}}^{(\alpha)}(\tilde{\beta}, \tilde{\mathbf{v}}_{\text{ext}}; \sigma) = \boldsymbol{\Omega}^{(\alpha)} \tilde{\beta}. \tag{4.51}$$

with $\alpha, \beta = (\phi, n, p, n_{\text{t}})$. As previously explained, $\tilde{\beta}$ and $\tilde{\mathbf{F}}^{(\alpha)}$ are the vectors of the Fourier (harmonic) amplitudes of the time-varying functions β and $\mathbf{F}^{(\alpha)}$, truncated to the harmonic order N_{H}. There is an explicit dependence of the collection of external sources $\tilde{\mathbf{v}}_{\text{ext}}$, corresponding to the Fourier transform of $\mathbf{v}_{\text{ext}}(t)$, which is the sum of a DC component and a single-tone time-varying amplitude of fundamental frequency ω_0. In this treatment, the input amplitude is small enough to have a linear response of the device, so that the Fourier expansion of each involved quantity can be truncated at $N_{\text{H}} = 1$, hence the only harmonic is $\omega_1 = \omega_0$. The external source is recursively applied to each terminal r, therefore the solution of (4.51) can be found without any linearization procedure, yielding the current $\tilde{\mathbf{I}}_k$ at the q terminal, whose DC component is $\tilde{\mathbf{I}}_{0,k}$ and the unique harmonic is $\tilde{\mathbf{I}}_{1,k}$. This allows to build the AC admittance matrix:

$$\mathrm{Y}_{k,r} = \frac{\tilde{\mathbf{I}}_{1,k}}{\tilde{\mathbf{V}}_{1,r}} \tag{4.52}$$

This procedure has the advantage of enabling the evaluation of the variability of the AC parameters as a consequence of a (time-independent) perturbation $\Delta\sigma = \sigma - \sigma_0$

by means of the numerically efficient GF technique. In fact, when the trap parameter undergoes a variation, (4.51) can be linearized around $(\beta_0, \mathbf{v}_{\text{ext}}; \sigma_0)$, giving rise to a LPTV system. Performing the analysis in the frequency domain, one obtains $\tilde{\omega}_1 = \omega_1 \pm \tilde{\omega} = \omega_1$, where $\tilde{\omega} = 0$ since the trap model parameter is time-independent. With these assumptions, the linearized system becomes:

$$\tilde{\mathbf{J}}^{(\alpha)}(\tilde{\beta}_0, \tilde{\mathbf{v}}_{\text{ext}}; \sigma_0)\Delta\tilde{\beta} - \mathbf{\Omega}^{(\alpha)}\Delta\tilde{\beta} = \tilde{\mathbf{s}}_0^{(\alpha)}(\tilde{\beta}_0, \tilde{\mathbf{v}}_{\text{ext}}; \sigma_0, \sigma) \tag{4.53}$$

where $\mathbf{J}^{(\alpha)}(\beta_0, \mathbf{v}_{\text{ext}}; \sigma_0) = \partial\mathbf{F}^{(\alpha)}/\partial\beta$ is calculated in the periodic solution β_0 and at σ_0, while the source term is approximated by finite differences. The CGFs of the linearized system, denoted as $\tilde{\mathbf{G}}_k^{(\alpha)}(\tilde{\beta}_0, \tilde{\mathbf{v}}_{\text{ext}}; \sigma_0)$, allow to compute the DC and the harmonic current variation at terminal k due to $\Delta\sigma$:

$$\Delta\tilde{\mathbf{I}}_{0,k}^{\sigma} = \sum_{\alpha} \left(\tilde{\mathbf{G}}_k^{(\alpha)}(\tilde{\beta}_0, \tilde{\mathbf{v}}_{\text{ext}}; \sigma_0)\right)_{(0,0)} \tilde{\mathbf{s}}_0^{(\alpha)}(\tilde{\beta}_0, \tilde{\mathbf{v}}_{\text{ext}}; \sigma_0, \sigma)\tilde{\mathbf{\Omega}} \tag{4.54a}$$

$$\Delta\tilde{\mathbf{I}}_{1,k}^{\sigma} = \sum_{\alpha} \left(\tilde{\mathbf{G}}_k^{(\alpha)}(\tilde{\beta}_0, \tilde{\mathbf{v}}_{\text{ext}}; \sigma_0)\right)_{(1,1)} \tilde{\mathbf{s}}_0^{(\alpha)}(\tilde{\beta}_0, \tilde{\mathbf{v}}_{\text{ext}}; \sigma_0, \sigma)\tilde{\mathbf{\Omega}} \tag{4.54b}$$

where $\tilde{\mathbf{\Omega}}$ is a block diagonal matrix containing the Vornoi volumes. The subscripts (0,0) and (1,1) denote the portion of the CGF linking, respectively, the DC and the first harmonic of the distributed source $\tilde{\mathbf{s}}_0^{(\alpha)}(\tilde{\beta}_0, \tilde{\mathbf{v}}_{\text{ext}}; \sigma_0, \sigma)$. Fig. 4.9 reports the Conversion Green's function distributions at drain contact associated to the occupied trap concentration of the fundamental frequency. In this case, CGFs are calculated from AC simulations performed on a 0.15 μm AlGaN/GaN HEMT device with Fe-doped buffer traps with 2 kHz operating frequency, $N_{\text{H}} = 1$ harmonic and an input tone of 1 mV applied to the drain contact. The *local variation source*, defined as the integrand function of (4.54b), reads:

$$\tilde{\text{LS}}_k^{(\alpha)} = \left(\tilde{\mathbf{G}}_k^{(\alpha)}(\tilde{\beta}_0, \tilde{\mathbf{v}}_{\text{ext}}; \sigma_0)\right)_{(1,1)} \tilde{\mathbf{s}}_0^{(\alpha)}(\tilde{\beta}_0, \tilde{\mathbf{v}}_{\text{ext}}; \sigma_0, \sigma) \tag{4.55}$$

From (4.52) and (4.54b), the AC admittance matrix due $\Delta\sigma$ can be calculated:

$$\text{Y}_{k,r}^{\sigma} = \text{Y}_{k,r} + \Delta\text{Y}_{k,r}^{\sigma} = \text{Y}_{k,r} + \frac{\Delta\tilde{\mathbf{I}}_{1,k}^{\sigma}}{\tilde{\mathbf{V}}_{1,r}} \tag{4.56}$$

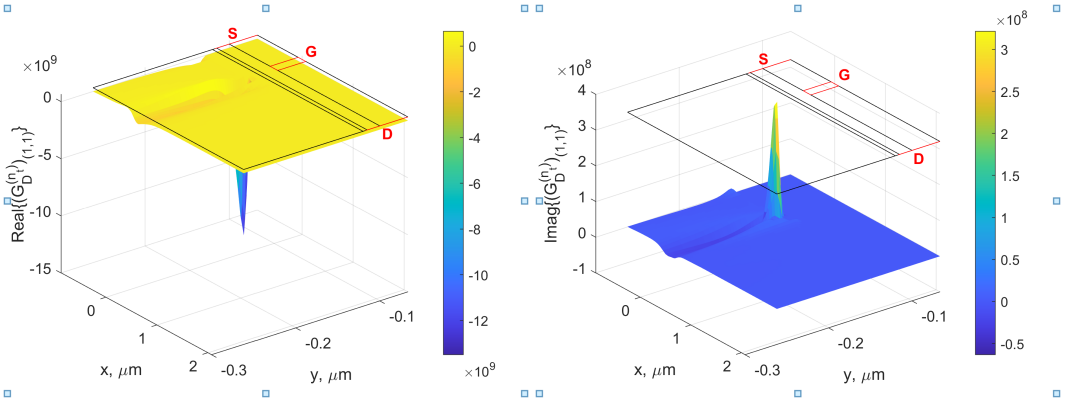

(a) Real part of $(\tilde{\mathbf{G}}_{\mathrm{D}}^{(n_{\mathrm{t}})})_{(1,1)}$.

(b) Imaginary part of $(\tilde{\mathbf{G}}_{\mathrm{D}}^{(n_{\mathrm{t}})})_{(1,1)}$.

Fig. 4.9 Green's Function of the electron continuity equation for the drain contact at the first harmonic input/output in a 0.15 μm GaN HEMT device. DC bias: $V_{\mathrm{D}} = 10$ V and $V_{\mathrm{G}} = -2.22$ V.

4.4.4 Advantages of the GF approach

The sensitivity analysis, addressed by the GF-based approach in both static and dynamic conditions, allows to calculate the terminal current variations through a convolution integral, involving the microscopic source of variation and the GFs themselves. Both these quantities allow for a simple and direct way to inspect the response of each harmonic, including DC component, to a structure, material or technological parameter variation with respect to a nominal value. Therefore, the GF approach gives a unique insight into the device operating conditions, highlighting which parts of the device are most affected by the parameter variations or contribute more to the terminal variations. Moreover, the linearized technique provides a computational advantage over repeated T-dependent or σ-dependent analyses. In fact, the Generalized Adjoint Approach enables the estimation of the relevant GFs with a negligible overhead with respect to the computation of the nominal solution. Thus, the simulation time is reduced roughly by a factor $n_{(\mathrm{T},\sigma)}$ compared to $n_{(\mathrm{T},\sigma)}$ repeated simulations. This advantage is especially appealing when the numerical burden of each individual solution is very high, such as for 3D simulations or in the LS analysis, where the number of equations to be solved is increased with respect to DC by a factor $2N_{\mathrm{H}}+1$ (usually $N_{\mathrm{H}} \geq 10$ for highly nonlinear RF applications). Another advantage of the proposed method is its compatibility with other simulations exploiting the same GFs. For example, it is possible to carry out, with virtually no extra numerical burden, *concurrent* temperature and variability analyses. The latter

involves technological and physical parameters, nevertheless also load variations represent an important source of variability in nonlinear stages [72], as it will be shown in Chapter 5.

Chapter 5

Efficient TCAD thermal analysis of a FinFET power amplifier

5.1 Introduction

In the previous chapter, a comprehensive framework to efficiently calculate the device response to temperature variations with respect to a nominal ("cold") thermal status has been presented. The modeling approach, based on the linearization of the physical model around the "cold" temperature, exploits the Green's Functions technique, which can be calculated efficiently from the numerical standpoint. The GF-based approach is, thus, based on TCAD physical simulations, which are by far the best environment to link the electrical characteristics to the technological process and accurately describe the active device T-dependent material properties and transport parameters. The numerical burden of TCAD simulations is very high, in particular for non-linear device modeling, nevertheless the proposed technique only requires one simulation at nominal temperature and the computational advantage scales with the number of temperatures or thermal resistances to be analyzed.

This chapter is aimed at demonstrating the advantage of GF-based approach in T-dependent device simulations, including the self-heating analysis in varying embedding thermal circuits [70]. Furthermore, concurrent temperature and variability analyses can be carried out with virtually no extra numerical burden [73, 74]. As a testbed to demonstrate the TCAD capability, the FinFET technology is targeted for possible applications in medium power stages where temperature becomes critical.

All the simulations, fully based on the proposed efficient TCAD analysis, are, thus, performed on a FinFET-based RF medium power amplifier.

FinFET technology, primarly developed for digital applications, is being actively investigated for its possible applications in analog stages thanks to FinFETs excellent performance in terms of cutoff and maximum oscillation frequencies, inherited by the nanometric size. Although limited to a few milliwatts of power, they are promising in view of millimeter-wave (mmW) phased arrays for 5G/6G, being the natural evolution of the RF CMOS technology [75, 76]. However the peculiar structure of FinFETs also brings along several issues that must be addressed to make the technology a viable candidate for telecommunication systems, where successful integration of RF and digital circuits could represent a disruptive advantage. The FinFET 3D geometry, together with the need of resorting to multi-finger or stacked structures to achieve the required output power [77, 78], leads to higher parasitic effects, more pronounced impact of technological variability and a very difficult thermal management due to the presence of low-thermal-conductivity materials [79]. As a consequence, accurate device electro-thermal modeling is required for an effective design of RF circuits, such as power amplifiers (PAs), where device self-heating must be carefully described.

5.2 Thermal DC analysis

For the validation of the proposed thermal analysis in the static case, a 54 nm Silicon FinFET structure with fin height of 25 nm, whose 2D cross section is shown in Fig. 5.1, is considered [70]. First, the in-house TCAD solver, including the Poisson equation and the continuity equations for electrons and holes, is exploited to perform a DC analysis at different temperatures in the range $T \in [310-350]$ K in order to find a *reference solution* (incremental method, INC). The INC solution is used to validate the GF-based analysis: GFs are extracted in DC conditions at $T_0 = 300$ K and exploited to calculate the drain current variation with temperature according to (4.30). Fig. 5.2 shows that the GF approach has an excellent agreement against the reference solution, which is especially evident above the threshold voltage, where there is higher thermal sensitivity due to mobility degradation. For analog applications, unlike the digital case, both the saturation current and knee voltage,

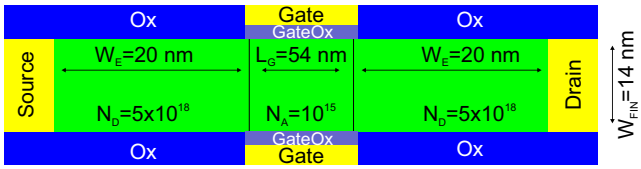

Fig. 5.1 Double Gate structure used for the validation of the in-house code for T-dependent static and dynamic analysis and DC self-heating analysis.

which characterize the device behavior above threshold, have more relevance with respect to the subthreshold behavior.

Then, the in-house simulator is exploited to perform a DC self-heating analysis with different thermal resistances $R_{\rm th} = 0.3$ K/μW and $R_{\rm th} = 1$ K/μW. The estimation of the thermal resistances follows the calculations of Fig. 5.3, based on the fin shape and the silicon thermal conductivity. The SHS system (2.38) is self-consistently solved in order to find a *reference solution* (incremental method, INC). The drain current obtained from the INC method is used to validate the GF-based self-heating approach: GFs are extracted at $T_0 = 300$ K with $R_{\rm th} = 0$, as for the T-dependent DC analysis, and exploited to calculate the drain current due to self-heating, following (4.45). Fig. 5.4 reports the device output characteristics when the heat sink temperature is $T_0 = 300$ K, showing a reduction of the current up to 17% due to self-heating. The effect of temperature increase can be traced in the negative slope of the saturation current, which is more pronounced with a higher thermal resistance. The analysis is repeated with T_0 raised to 320 K as shown in Fig. 5.5: the higher knee voltage and the negative slope of the saturation current are due to the presence of the thermal resistance and to the increase of the heat sink temperature. With $T_0 = 320$ K and $R_{\rm th} = 1$ K/μW, the device temperature is as high as 390 K for the largest dissipation (see Fig. 5.6). All simulations demonstrate that the GF approach, requiring a single simulation of the "cold" device with $T_0 = 300$ K and $R_{\rm th} = 0$, compares very well with the reference simulations, that require instead multiple solutions with varying $R_{\rm th}$ and T_0.

5.3 Temperature-dependent LS analysis

The GF-based technique is now validated in dynamic conditions [70]. The in-house code, solving the PDD-ECE system (2.35), is used to perform a T-dependent LS

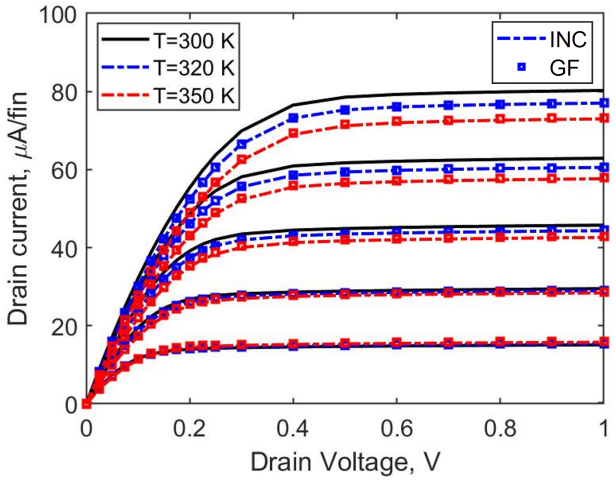

Fig. 5.2 FinFET output characteristics with V_G = [0.6, 0.7, 0.8, 0.9, 1] V with varying T.

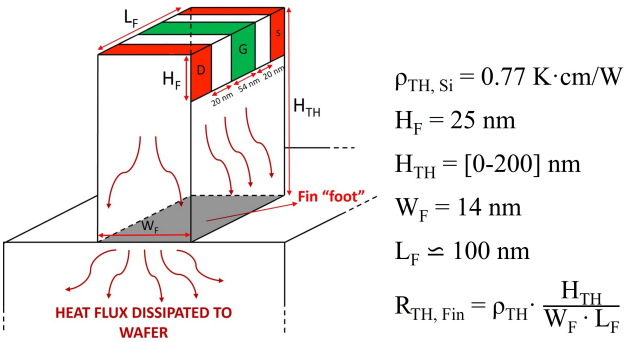

Fig. 5.3 FinFET structure used for the fin thermal resistance calculation: $\rho_{TH,Si}$ is the silicon thermal conductivity.

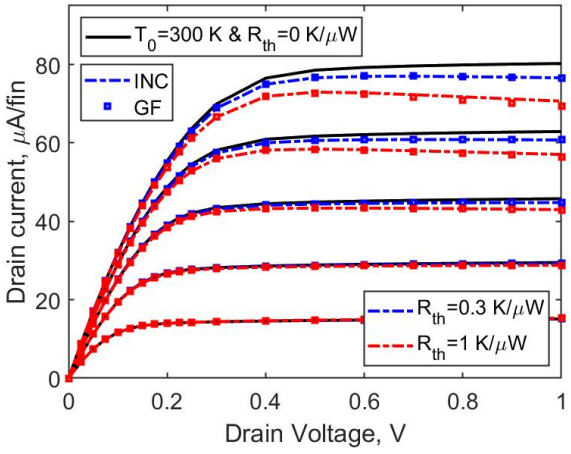

Fig. 5.4 FinFET output characteristics with V_G = [0.6, 0.7, 0.8, 0.9, 1] V with varying R_{th}.

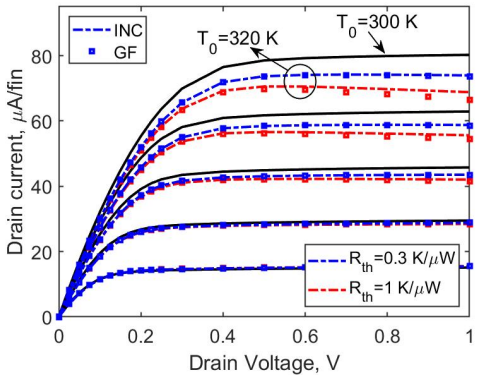

Fig. 5.5 FinFET output characteristics with V_G = [0.6, 0.7, 0.8, 0.9, 1] V at T_0 = 320 K.

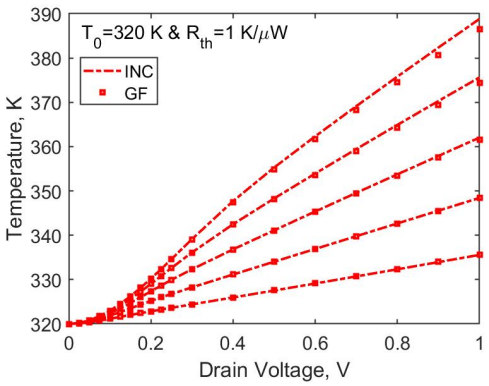

Fig. 5.6 Device temperature with T_0 = 320 K and R_{th} = 1 K/μW.

analysis on the same FinFET structure of Fig. 5.1, with fin height of 25 nm. The device is simulated as a Class A power amplifier (PA) operating at a frequency of 70 GHz and assuming a multifinger structure (see Fig. 5.7), composed of 10 fingers of 30 fins each and corresponding to a total gate periphery of 15 μm. Since this is a 2D analysis, the only two lateral channels for each fin are considered, but this is not a severe limit since the third channel current is much lower. The DC bias of the Class A PA is selected at $V_G = 0.675$ V and $V_D = 0.6$ V. The real part of the optimum load has been calculated according to the load-line approach [80], while the imaginary part tunes out the output admittance at the bias point and at the nominal temperature $T_0 = 300$ K. The optimum load turns out to be $Z_{opt} = 53 + j6\ \Omega$, while the drain current harmonics are shunted by ideal tuners. The input port has been left unmatched and terminated with a 50 Ω/mm impedance. The LS analysis has been carried out with $N_H = 10$ harmonics, increasing the input power driving the amplifier from back-off to approximately 2 dB gain compression. At each input power, the CGFs are calculated at $T_0 = 300$ K and the variation of the drain current harmonics with T is evaluated according to (4.38) for 5 temperatures ($T \in [310 - 350]$ K). GF results are compared to repeated LS analyses with temperature varying in the same range (INC method), always obtaining an excellent agreement between the two methods. Notice that the simulation time for each power sweep is roughly 4 hours, hence the GF method time saving is of about 20 hours computation time. Fig. 5.8 shows the dynamic load lines (DLL) in the output characteristics plane both in back-off and compression conditions. With increasing temperature, the drain current exhibits a reduced swing with respect to the "cold" device, especially evident

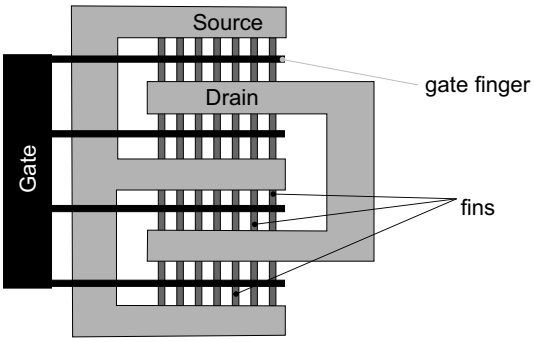

Fig. 5.7 Schematic representation of a multifinger FinFET PA layout.

at 2 dB gain compression (see Fig. 5.8b). This effect is essentially due to mobility degradation and the consequent increase of the knee voltage, suggesting that the output power is decreasing with T. Figs. 5.9a and 5.9b show the output power and gain of the power cell with increasing temperature. The power performance exhibits a noticeable degradation, with up to 1 dB less output power and gain at $T = 350$ K. The thermal sensitivity is higher in back-off and limited in compression: in fact, the variation of the output power above the 1 dB compression point is dominated by the knee voltage walk-out with temperature, which is in any case quite limited (see also Fig. 5.8b). Fig. 5.10 shows the stage efficiency and its variation with respect to the "cold" case as a function of the input power. The thermal sensitivity depends again on the input power having a maximum value at 1 dB compression, but a significant efficiency reduction is found in a wide range of output power, roughly from -10 dBm to saturation. This needs to be taken carefully into account in the design of quasi-linear stages, often operated with modulated signals whose average value is well in back-off. While the temperature sensitivity of the fundamental tone decreases at higher power, the harmonics are instead sharply increasing. Harmonics are also found to be affected by the highest variation with T, see Fig. 5.11. The harmonic variations can be up to 10% with just 20 K of temperature increase. Notice that the linearized GF approach is always delivering a fast and accurate thermal analysis of the power stage.

5.4 T-dependent, load-dependent LS analysis

A T-dependent LS analysis with concurrent load variations is now performed to show the accuracy of the GF approach with an additional variability source due to the

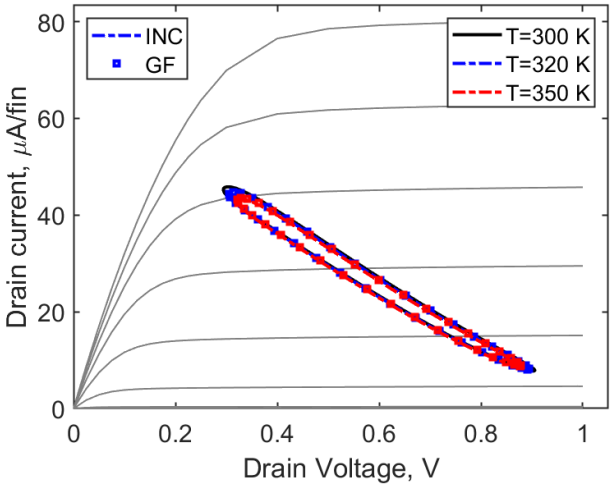

(a) Back-off conditions ($P_{\text{av}} = -8$ dBm).

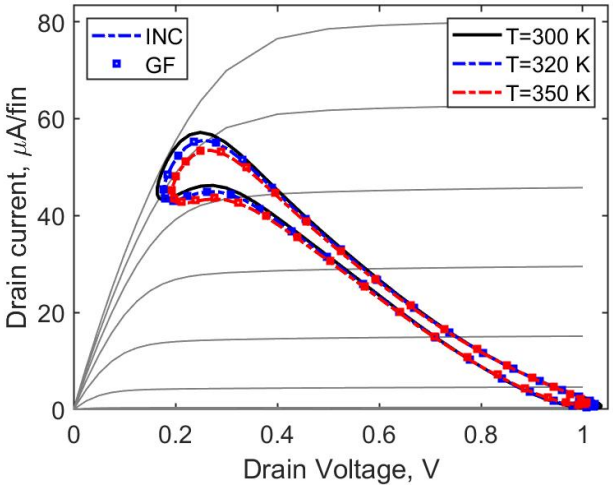

(b) Compression conditions ($P_{\text{av}} = -3$ dBm).

Fig. 5.8 Dynamic load lines as a function of T.

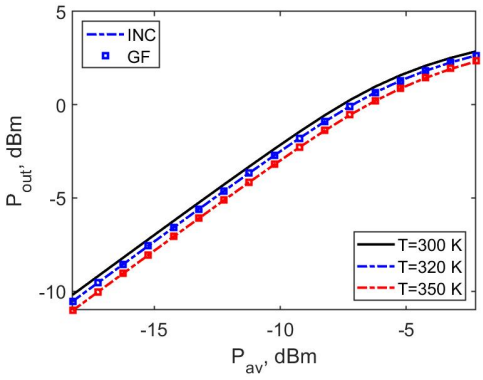

(a) Output power of the Class A PA.

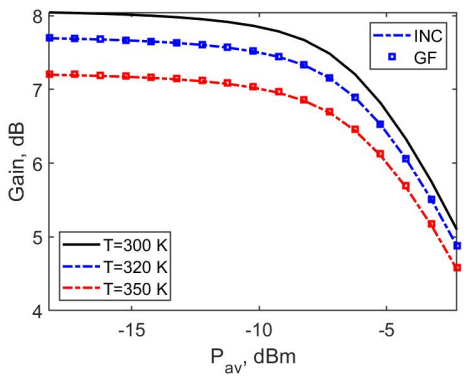

(b) Trasduction gain of the Class A PA.

Fig. 5.9 Output power and gain of the FinFET PA as a function of temperature.

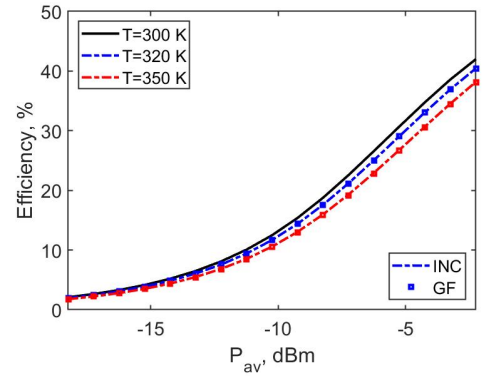

(a) Efficiency of the Class A PA.

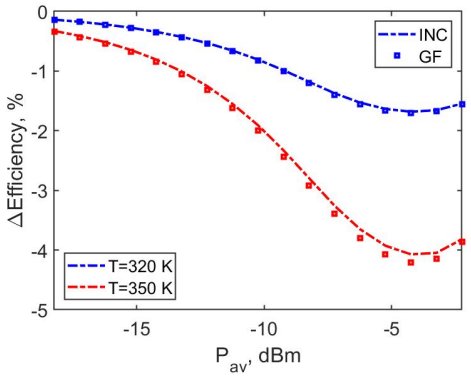

(b) Efficiency variation of the Class A PA.

Fig. 5.10 Efficiency and its variation of the FinFET PA as a function of temperature.

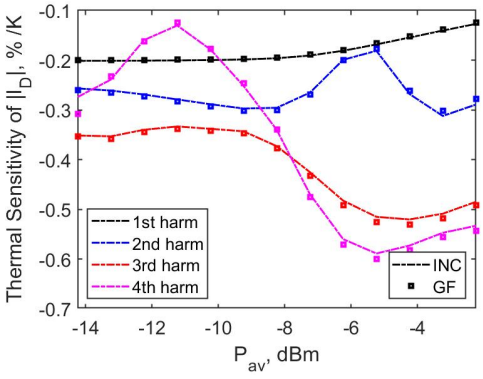

(a) Magnitude thermal sensitivity of the class A PA harmonics.

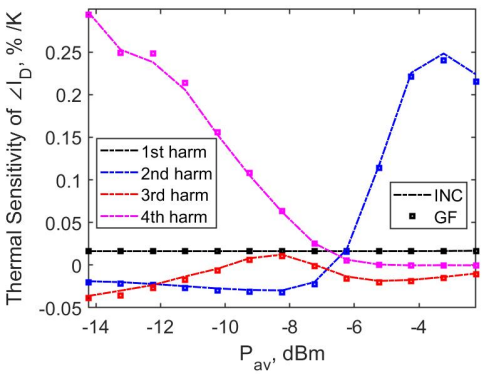

(b) Phase thermal sensitivity of the class A PA harmonics.

Fig. 5.11 Percentage variation per unit temperature of the magnitude and phase of the class A PA harmonics vs. input drive.

external circuit. The aim is to assess the overall power stage robustness against the concurrent variations of temperature and load termination (e.g. due to the variability of the matching network, see [72]). To this aim, the GF-based approach discussed in Section 4.4.1 needs to be extended, since it only takes into account temperature variations [73].

Consider an active device with N-ports connected to an N-port external load, as shown in Fig. 5.12 (left). The discretized PDD model is coupled to the ECEs, here represented by the equivalent load and power sources [81]. The device and circuit constitutive equations form a coupled system:

$$i_{\mathrm{D}} = f(v_{\mathrm{D}}, T) \tag{5.1a}$$

$$v_{\mathrm{L}} = \mathbf{Z}_{\mathrm{L}} i_{\mathrm{L}} + v_{\mathrm{Z}} \tag{5.1b}$$

where (D) stand for the device and (L) for the circuit (load) terminal variables. All variables of system (5.1) are described in the frequency domain by the corresponding set of harmonic amplitudes (phasors), one for each of the harmonics included in the LS simulation (including the DC component). The nominal solution of (5.1), corresponding to the PA LS working point, is found by the TCAD solver in mixed-mode configuration, hence solving the PDD-ECE system at nominal "cold" temperature T_0 and nominal load $\mathbf{Z}_{\mathrm{L}}$. The system is linearized around the LS steady-state to account for a temperature variation ΔT in the physical model concurrent with a load variation $\Delta\mathbf{Z}_{\mathrm{L}}$, yielding:

$$\Delta i_{\mathrm{D}} = \left.\frac{\partial f(v_{\mathrm{D}}, T)}{\partial v_{\mathrm{D}}}\right|_0 \Delta v_{\mathrm{D}} + \left.\frac{\partial f(v_{\mathrm{D}}, T)}{\partial T}\right|_0 \Delta T = \mathbf{Y}_{\mathrm{SSLS}}\, \Delta v_{\mathrm{D}} + \Delta i_{\mathrm{T}} \tag{5.2a}$$

$$\Delta v_{\mathrm{L}} = \mathbf{Z}_{\mathrm{L}}\, \Delta i_{\mathrm{L}} + \Delta\mathbf{Z}_{\mathrm{L}}\ i_{\mathrm{L}}|_0 = \mathbf{Z}_{\mathrm{L}}\, \Delta i_{\mathrm{L}} + \Delta v_{\mathrm{Z}} \tag{5.2b}$$

The subscript '0' refers to the LS working point, while $\mathbf{Y}_{\mathrm{SSLS}}$ is the SSLS device admittance matrix, efficiently computed from SSLS TCAD analysis [82] concurrently with CGFs, solving system (4.24). As explained in Section 4.4.1, the lattice temperature is considered a time-invariant perturbation, hence the sideband frequency $\tilde{\omega}$ collapses onto the unperturbed frequencies ω_n and both the admittance matrix and the CGFs are calculated at $\tilde{\omega}_n = \omega_n$. Equation (5.2) is a linear system where the impressed generators Δi_{T} and Δv_{Z} collectively represent the equivalent terminal effect of ΔT and $\Delta\mathbf{Z}_{\mathrm{L}}$. The linearized model allows for the representation in Fig. 5.12

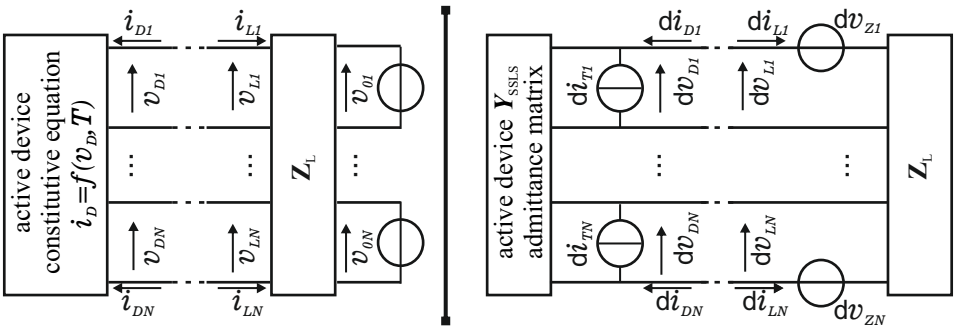

Fig. 5.12 Schematic representation of the linearized device including temperature induced and load-induced variations.

(right) and with $\Delta v_{\mathrm{L}} = \Delta v_{\mathrm{D}}$ and $\Delta i_{\mathrm{L}} = -\Delta i_{\mathrm{D}}$, (5.2) leads to:

$$\Delta i_{\mathrm{D}} = \left(\mathbf{I} + \mathbf{Y}_{\mathrm{SSLS}}\mathbf{Z}_{\mathrm{L}}\right)^{-1}\left(\Delta i_{\mathrm{T}} + \mathbf{Y}_{\mathrm{SSLS}}\Delta v_{\mathrm{Z}}\right) \tag{5.3}$$

where Δi_{D} is the total current due concurrent temperature and load variations. Generators Δv_{Z} are directly computed from the nominal LS solution using (5.2b), while impressed generators Δi_{T}, only due to temperature, are computed exploiting the GF approach following (4.38).

For comparison, a TCAD analysis of the same FinFET-based power amplifier (PA) is carried out in LS conditions as a function of both temperature and load variations. Repeated simulations are performed solving system (2.35) at 5 temperatures ($T \in [310-350]$ K) and for 2 load variations (± 5 % of the real part of the load) in order to find a reference solution (incremental method, INC). On the other hand, the CGFs are calculated at $T_0 = 300$ K and the variation of the drain current harmonics with T and $\mathbf{Z}_{\mathrm{L}}$ is evaluated according to (5.3). For example, varying the real part of the optimum load by ± 5 % with respect to the nominal case, doubles the simulation time for the INC approach, while the GF analysis following (5.3) requires a negligible time overhead.

Fig. 5.13 shows the dynamic load lines of the FinFET PA, assuming the multifinger structure of Fig. 5.7, both in back-off and compression conditions. The accuracy of the DLL shows that the harmonics are also well reproduced by the proposed GF T-dependent LS analysis. Moreover, Fig. 5.13b shows that, at 2 dB gain compression, the device is driven more harshly into compression by the increasing load, whereas the compression is lower in the opposite case, but the output swing is in any case reduced by the T-induced knee voltage increase. Figs. 5.14 and 5.15 show that,

with a higher value of $\mathbf{Z}_{\mathrm{L}}$, both the output power and PAE degrade with increasing temperature, retaining a good agreement between INC and GF solution. Moreover, Fig. 5.16 highlights the different P_{out} trend for two values of the available power: at $P_{\mathrm{av}} = -8$ dBm the output power increases with the load, while it decreases with an increasing $\mathbf{Z}_{\mathrm{L}}$ at $P_{\mathrm{av}} = -3$ dBm. This confirms the behavior of the DLL of Fig. 5.13b, where the device is more compressed by an increasing load. Turning to the relative importance of the two variations, Fig. 5.17 reports the P_{out} and PAE variation with respect to their *nominal value* (i.e., $T_0 = 300$ K and nominal load). In this figure, lines represent the variations due to temperature only, while the error bars represent the extra spread expected because of the $\pm 5\%$ load variations. Noticeably, the detailed variations depend on the input power: for example, at each T, with larger load ($+5\%$), P_{out} increases in back-off, while in compression conditions it exhibits an opposite behavior, confirming the trend of Fig. 5.16. Furthermore the load sensitivity is lower in compression, again due to the reduced effect of the load termination at the knee. PAE has the highest load sensitivity close to the onset of gain compression (here around -7 dBm), but variations with temperature are in any case dominating, leading to a significant PAE reduction in a wide range of output power, roughly from -10 dBm to saturation. All these intermixed effects are correctly reproduced by the GF analysis. Overall, the stage exhibits a spread of roughly 1 dB for P_{out} and 5 percentage points for PAE.

5.5 T-dependent, doping-dependent LS analysis

Purpose of this section is to assess how the PA performance will be affected by the concurrent effect of heating and doping variability: the attention is focused on the variations of the source and drain doping, especially affecting the device parasitic resistance and, as a result, the PA efficiency. Here, deterministic doping variations are considered, to selectively understand their effect concurrently with the temperature in a LS analysis. As in the previous section, the GF-based technique accounts for temperature variations only, therefore it needs to be extended [74].

Consider an active device with N-ports connected to an N-port external load, as in Fig. 5.18 (left), where the device constitutive equations $f(v_{\mathrm{D}}, T, \sigma)$ collectively represent a discretized physics-based model, in this case the PDD-ECE system. Symbols T and σ are two parameters influencing the active device operation: respectively,

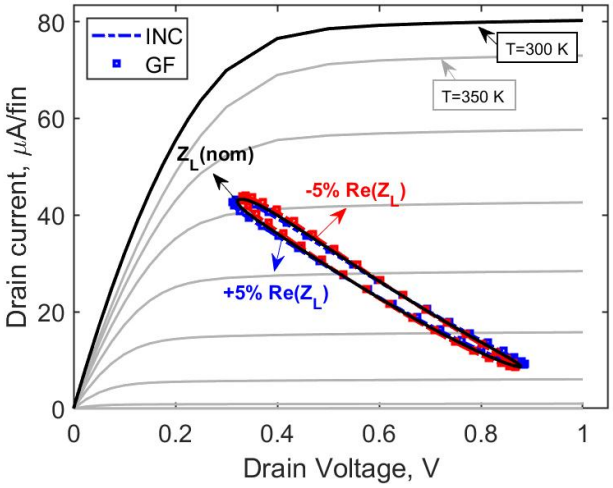

(a) Back-off conditions ($P_{\text{av}} = -8$ dBm).

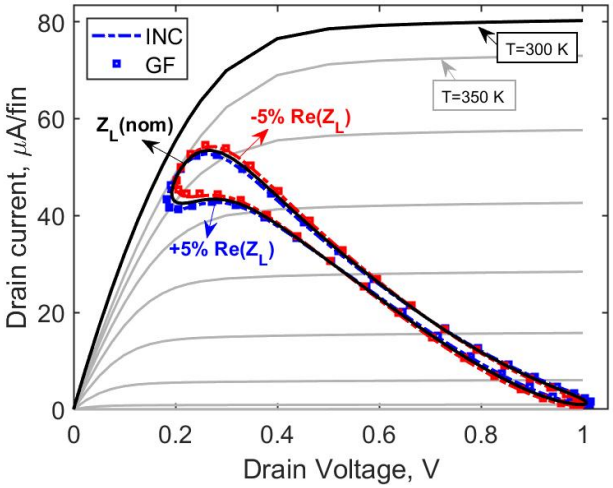

(b) Compression conditions ($P_{\text{av}} = -3$ dBm).

Fig. 5.13 Dynamic load lines T = 350 K and varying the load condition.

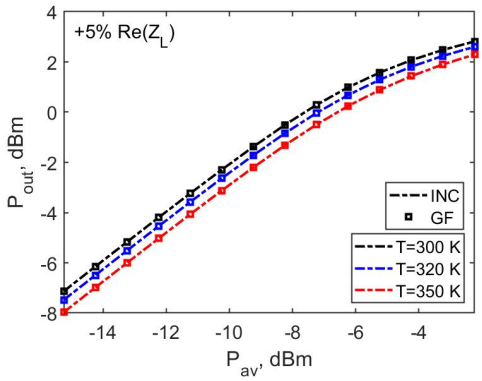

Fig. 5.14 P_{out} with varied load at different T.

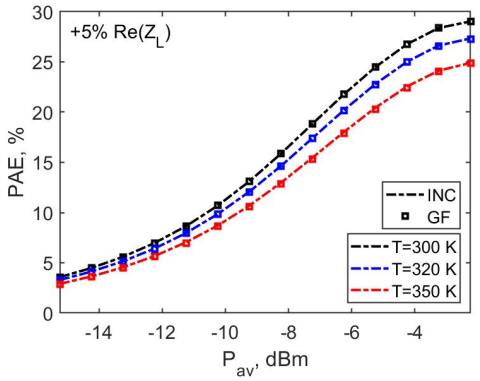

Fig. 5.15 PAE with varied load at different T.

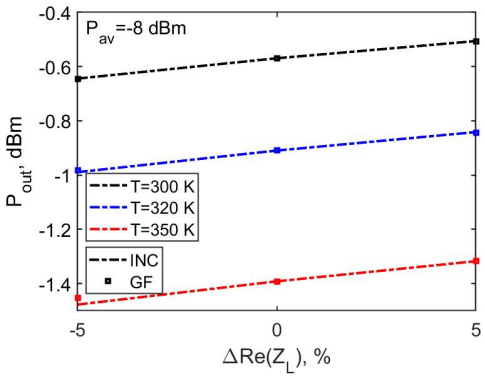

(a) Output power in back-off region.

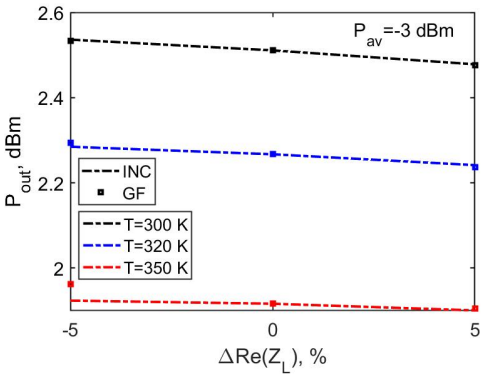

(b) Output power in compression region.

Fig. 5.16 Output power as a function of the load variation at different temperatures.

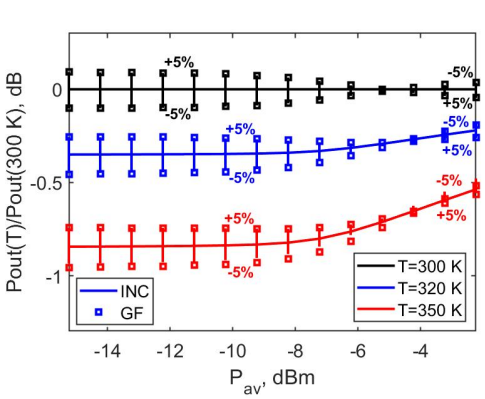

(a) Output power variation.

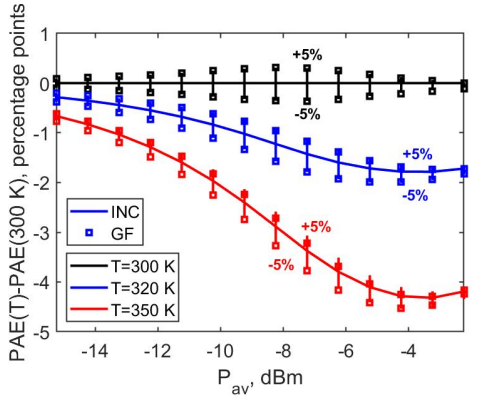

(b) PAE variation.

Fig. 5.17 Expected spread of P_{out} and PAE due to ± 5 variation of $Re(Z_L)$ with concurrent T variations. Error bars: INC analysis; symbols: GF analysis.

temperature, and one physical parameter, in this case the doping. The device and circuit equations form a coupled system:

$$i_{\mathrm{D}} = f(v_{\mathrm{D}}, T, \sigma) \tag{5.4a}$$

$$v_{\mathrm{L}} = \mathbf{Z}_{\mathrm{L}} i_{\mathrm{L}} + v_0 \tag{5.4b}$$

where (D) stand for the device and (L) for the circuit (load) terminal variables evaluated in the PA LS working point. To efficiently account for a temperature variation ΔT and any parameter variation $\Delta\sigma$, the system is then linearized around the LS steady-state (nominal value σ_0 of the parameter and at nominal "cold" temperature T_0). Imposing the constitutive equations $i_{\mathrm{D}} = -i_{\mathrm{L}}$ and $v_{\mathrm{D}} = v_{\mathrm{L}}$ and assuming the two variations in first place uncorrelated, one obtains:

$$\begin{aligned}\Delta i_{\mathrm{D}} = &\left.\frac{\partial f(v_{\mathrm{D}}, T, \sigma)}{\partial v_{\mathrm{D}}}\right|_0 \Delta v_{\mathrm{D}} + \left.\frac{\partial f(v_{\mathrm{D}}, T, \sigma)}{\partial T}\right|_0 \Delta T \\ &+ \left.\frac{\partial f(v_{\mathrm{D}}, T, \sigma)}{\partial \sigma}\right|_0 \Delta\sigma = \mathbf{Y}_{\mathrm{SSLS}}\, \Delta v_{\mathrm{D}} + \Delta i_{\mathrm{T}} + \Delta i_{\sigma}\end{aligned} \tag{5.5a}$$

$$\Delta v_{\mathrm{D}} = -\mathbf{Z}_{\mathrm{L}}\, \Delta i_{\mathrm{D}} \tag{5.5b}$$

The subscript '0' refers to the LS working point, while $\mathbf{Y}_{\mathrm{SSLS}}$ is the SSLS device admittance matrix, efficiently computed from SSLS TCAD analysis concurrently with CGFs, solving system (4.24). As in the previous case, since the lattice temperature is considered a time-invariant perturbation, the sideband frequency collapses into the unperturbed frequencies, hence $\tilde{\omega} = 0$ and $\tilde{\omega}_n = \omega_n$. Moreover, Δi_{T} and Δi_{σ} are interpreted as impressed generators, collectively representing the equivalent terminal effect of ΔT and $\Delta\sigma$, see Fig. 5.18 (right). The impressed generator Δi_{σ} is computed using the in-house TCAD simulator by means of the CGF, with negligible numerical overhead with respect to the computation of the nominal device LS working point [17]. Using linear superposition, the effect of concurrent T and σ variations is extracted inverting the perturbed system (5.5):

$$\Delta i_{\mathrm{D}} = \left(\mathbf{I} + \mathbf{Y}_{\mathrm{SSLS}} \mathbf{Z}_{\mathrm{L}}\right)^{-1} \left(\Delta i_{\mathrm{T}} + \Delta i_{\sigma}\right) \tag{5.6}$$

where Δi_{D} is the total current due concurrent temperature and doping variations. Impressed generators Δi_{T} only due to temperature are computed exploiting the GF approach following (4.38). Notice that the extension of the GF technique to the

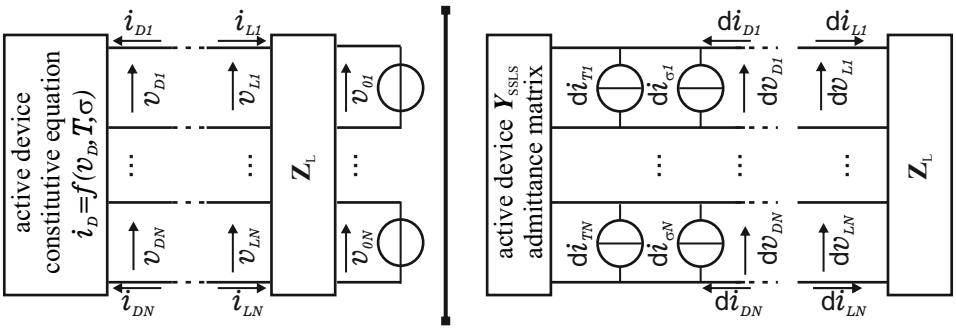

Fig. 5.18 Schematic representation of the linearized device including temperature and parameter variations (e.g. doping).

analysis of concurrent multiple parameters and temperature variations is obvious, because superposition applies in the linearized approach.

Let us apply this technique to the analysis of a FinFET-based power amplifier as a function of both temperature and doping variations. The device under analysis, shown in Fig 5.19, is slightly different from the previous one, but simulated in the same operating conditions. Repeated simulations are carried out, solving the PDD-ECE system (2.35), at 5 temperatures ($T \in [310-350]$ K) with a concurrent ± 15 % doping spread, in the source/drain regions, in order to find the reference solution (incremental method, INC). On the other hand, the CGFs are calculated at $T_0 = 300$ K and the variation of the drain current harmonics with T and σ is evaluated according to (5.6). Fig. 5.20 shows the output power of the PA cell with increasing T. The gain with concurrent 20 K T increase and $\pm 15\%$ doping spread is reported in Fig. 5.21. The power performance exhibits more than 1 dB output power loss with 50 K temperature increase. In fact, with increasing temperature, the output power degradation is driven by the mobility reduction and increased source/drain parasitic resistance. The doping variations further affect the same resistances both through mobility degradation and the carrier density spread: hence with higher doping the PA degradation with temperature is milder. The impact of doping is especially significant when the device enters compression: Fig. 5.21 shows a 1 dB gain compression point at $P_{\text{av}} = -7.24$ dBm at $T = 320$ K and nominal doping. At this input power, gain has around 0.3 dB spread due to doping variations. The 1 dB compression point, instead, exhibits about 1 dB P_{av} spread with doping, with respect to the $T = 320$ K case. The variation of the output power and gain above the 1 dB compression point is mainly due to the knee voltage walk-out with T and doping [83], see the dynamic load lines of Fig. 5.22 with concurrent T and doping spread.

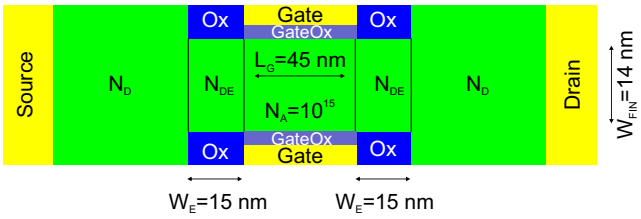

Fig. 5.19 Double Gate structure cross-section of each fin of the PA. $N_D = 10^{20}$ cm^{-3}; $N_{DE} = 7.5 \cdot 10^{18}$ cm^{-3}; oxide equivalent thickness 1 nm.

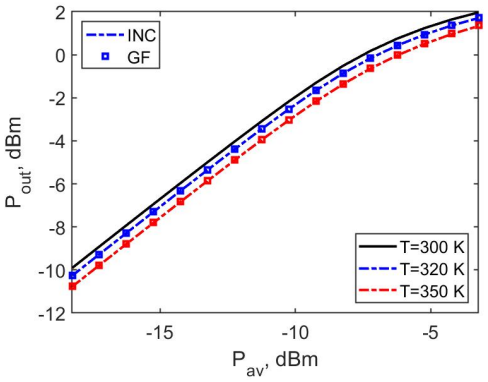

Fig. 5.20 Output power for the Class A PA at different temperatures.

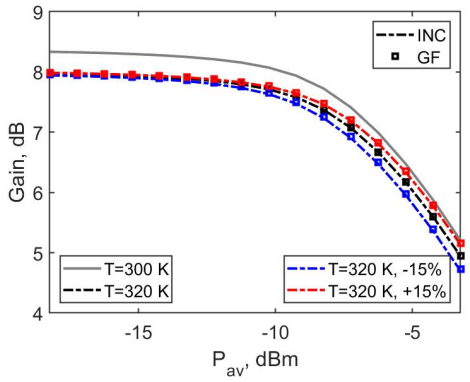

Fig. 5.21 Transduction Gain for the class A PA vs. concurrent T and doping variations.

Notice that the lower the doping, the more the device undergoes early compression, corresponding to lower gain and output power. Both T and the resistive loss in the source and drain regions affect the stage efficiency considerably. Fig. 5.23a shows the PA efficiency as a function of the input power: with increasing temperature the efficiency is always less than in the "cold" device due to the combined effect of T degradation and larger parasitic resistances. Doping variations affect efficiency in a more limited way. To highlight their effect, Fig. 5.23b reports the efficiency variation with respect to the reference solution (i.e., the $T_0 = 300$ K case and nominal doping): at moderate compression (i.e. with $[-14, -8]$ dBm input power), the stage with lower doping is pushed more into compression (see again Fig. 5.22) and exhibits a higher efficiency with respect to the device with higher doping, which is still in back-off. With increasing compression, though, the stage with lower doping eventually shows an even worse efficiency than the stage with nominal doping due to the higher parasitic resistance.

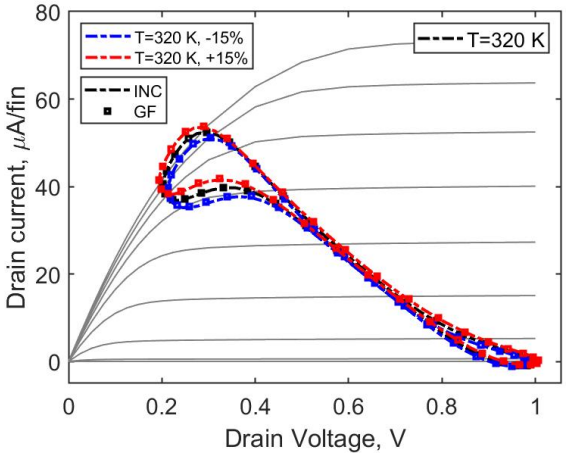

Fig. 5.22 DLL as a function of T at 2 dB gain compression ($P_{\text{av}} = -3$ dBm). Concurrent T and doping variations from reference T_0 = 300 K solution. DC curves are at T = 320 K.

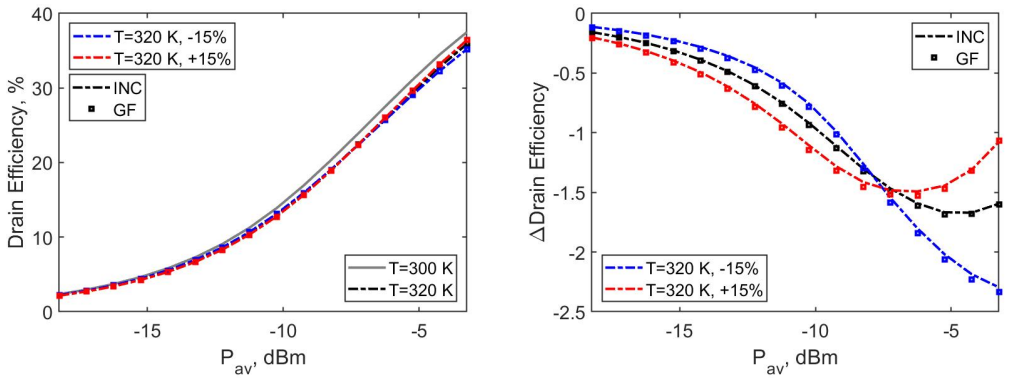

(a) Efficiency for the class A PA.

(b) Efficiency variation for the class A PA.

Fig. 5.23 Efficiency and its variation for the PA vs. concurrent T and doping variations.

5.6 Conclusions

In this chapter, a novel TCAD approach for an efficient T-dependent sensitivity analysis, based on the GF-based approach, is validated in a FinFET-based power amplifier in both the DC regime, including self-heating, and LS conditions. The GF approach is capable to accurately reproduce the device behavior in all operating conditions up to 50 K temperature increase, showing a large advantage in terms of computational cost. The DC drain current exhibits a strong degradation with increasing temperature, especially in presence of a thermal resistance. Moreover, the LS stage is characterized by an overall thermal degradation, leading to more than 1 dB output power loss and PAE reduction from 28% to 23%. The proposed technique extends, with negligible numerical overhead, the GF-based approach to concurrent temperature and physical/technological parameter variations. In fact, the LS T-dependent analysis is performed with concurrent load variations, showing that, despite thermal sensitivity dominates over load sensitivity, the latter is stronger in back-off conditions. Furthermore, the LS device response is also evaluated with concurrent temperature and doping variations of the channel contact regions. Doping variations further affect the PA 1 dB compression point with a 1 dB input power spread. In conclusion, the GF-based technique demonstrates that LS TCAD analysis is mature enough for the assessment of nonlinear circuits and represents a first step towards the development of physically sound, temperature dependent, LS circuit models.

Chapter 6

Thermal modeling of a FinFET power amplifier through X-parameters

6.1 Introduction

The previous chapter is aimed at demonstrating that the in-house TCAD simulator, implementing both the LS and SSLS analyses with the HB technique [82], represents a flexible platform to simulate the active device in the operating conditions typical of actual microwave applications, e.g. class B power amplifiers or mixers [76]. Despite TCAD physical simulations accurately describe the device behavior in terms of material properties and transport parameters, their numerical burden is very high. This problem is especially relevant in non-linear device modeling, where LS simulations through the HB technique require a large number of harmonics. The TCAD computational cost suggests that it cannot be used routinely for circuit design but it is likely prone to be the basis to extract accurate, computationally efficient circuit-level device models. Behavioral models, usually derived from measurements, have been recently proposed as the ideal framework to translate TCAD simulations (that can be regarded as *virtual device measurements*) into EDA tools for circuit design [84]. As demonstrated in [85], X-parameters (Xpars) [86] are an effective behavioral model that can be used to retain the accuracy of TCAD analysis and the link to the fabrication process (e.g. device doping or temperature). Moreover, they can be directly extracted from the in-house TCAD simulator, as fully explained in [85, 87]. The Xpar model can be extended, including an explicit dependence

on the device lattice temperature, leading to a T-dependent Xpar model (T-Xpar). The T-Xpar model assumes the lattice temperature uniform throughout the device and hence identified with its junction temperature. It can be directly included into Keysight ADS [88] using a dedicated port for the junction temperature that allows for the device simulation with varying ambient temperature, but also to couple an external thermal impedance to model device self-heating in dynamic LS conditions. Therefore, while the Xpar electrical model does not include any thermal memory effect, the T-Xpar model can be regarded as a first step towards the development of a nonlinear dynamic electro-thermal behavioral model [14, 21].

In this chapter, the T-Xpar model of a 54 nm Si FinFET presented in Chapter 5 is extracted from the in-house TCAD solver and exploited to implement a complete dynamic electro-thermal device model into Keysight ADS. First, a brief explanation of X-parameters is reported, following there is a description of how the T-Xpar model is extracted and implemented in ADS, showing both T-dependent and self-heating simulations in LS conditions [89, 90]. Finally, to demonstrate the importance of the dynamic self-heating analysis, the Xpar-based technique is applied to a FinFET PA under pulsed operation, sweeping the bias conditions from class A to class B [91].

6.2 T-dependent X-parameter model

The Xpar model extends the concept of multiport S-parameters to the nonlinear case. The reflected wave b_{pk} at port p and harmonic k resulting from the incident waves a_{ql} can be expressed as [86]:

$$b_{pk}(|a_{11}|,\omega) = X^{\mathrm{F}}_{pk}(|a_{11}|,\omega,T) \quad + \sum_{q} \sum_{l=1,\dots N} X^{\mathrm{S}}_{pq,kl}(|a_{11}|,\omega,T) P^{k-l} a_{ql}$$
$$+ \sum_{q} \sum_{l=1,\dots N} X^{\mathrm{T}}_{pq,kl}(|a_{11}|,\omega,T) P^{k-l} a^{*}_{ql} \tag{6.1}$$

Functions X^{F}, X^{S} and X^{T}, depending on the input large signal incident wave $|a_{11}|$, fully identify the model: X^{F} relates to the AM-AM/AM-PM curves with a perfectly matched port impedance (typically 50 Ω), while X^{S} and X^{T} are sensitivity terms accounting for the device response to a (small) load mismatch. Sampling the Xpar model over a prescribed input power interval, a look up table model (black box

model) suited for circuit level analysis is generated. In this work, the proprietary ADS *.xnp* file format is adopted with the corresponding Xpar schematic component [88]. Equation (6.1) explicitly assumes that the Xpar model is extracted at any given temperature [92]: from the modeling standpoint this means that the model can be regarded as parametrically dependent on the (constant) device lattice temperature T. Therefore, the *.xnp* file must also be parametrized in terms of T and the schematic component must reflect this temperature dependency.

To demonstrate the procedure, in-house TCAD simulations, implementing the Harmonic Balance LS and SSLS analyses, are used to extract the T-Xpar model, namely X^{F} from the LS working point and X^{S} and X^{T} from the admittance conversion matrix. The active device under analysis is a 54 nm Si FinFET with fin height of 25 nm, corresponding to the same case study analyzed in Chapter 5, simulated as a multifinger unit cell (see Fig. 5.7). The two gates are considered as a unique gate contact making the FinFET globally a 2-port. First, the FinFET TCAD LS analysis has been carried out exploiting the in-house TCAD device simulator with $N_{\mathrm{H}} = 10$ harmonics and increasing input power from back-off to approximately 2 dB gain compression. The device is terminated on 50 Ω load. At each input power, T-Xpars have been then extracted, with a 50 Ω reference port impedance, at three *extraction temperatures*, i.e. $T = 300$ K, 340 K, 380 K, and collected into a single *.xnp* file. The Xpar schematic component has an extra DC port, as shown in Fig. 6.1, with null current and a fictitious voltage used to select the device operating temperature spanning the data stored in the *.xnp* file. ADS interpolates among the available data in the *.xnp* file, allowing for simulations with continuously varying T. A certain degree of extrapolation beyond the interval of the extraction temperatures is also allowed by cubic spline interpolation. Fig. 6.2 shows an example of X^{S} and X^{T} obtained from TCAD analysis. The selected parameters account for the mismatch of the output load with respect to 50 Ω. While $\left|X^{\mathrm{S}}\right|$ shows a significant temperature spread with increasing input power, $\left|X^{\mathrm{T}}\right|$ is nearly constant, consistently with the results in [88]. A non monotonous behavior is observed for the phase, with up to 10° variation of the X^{T} phase with temperature.

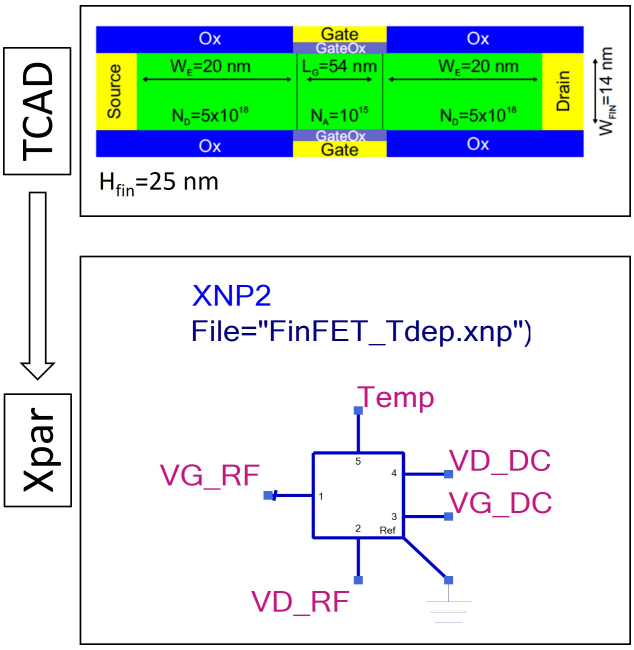

Fig. 6.1 Top: cross-section of the single fin double gate device used for the TCAD simulations. Bottom: Xpar model used in ADS, showing the extra temperature port.

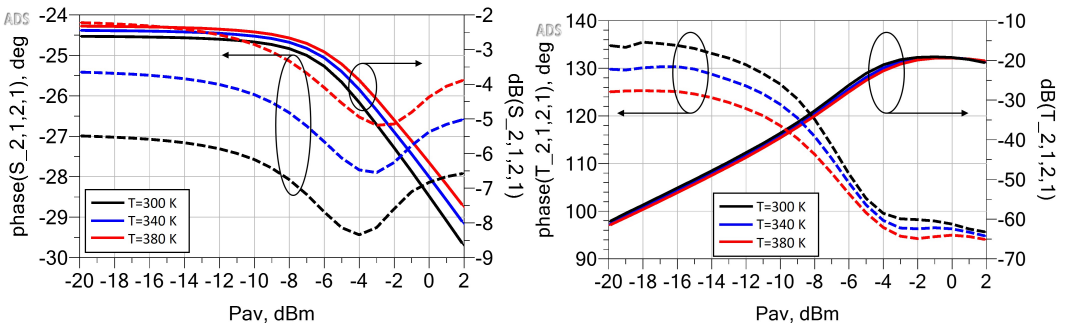

(a) Magnitude and phase of $X^{S}_{22,11}$.

(b) Magnitude and phase of $X^{T}_{22,11}$.

Fig. 6.2 Temperature dependency of X^{S} and X^{T} extracted from TCAD analysis.

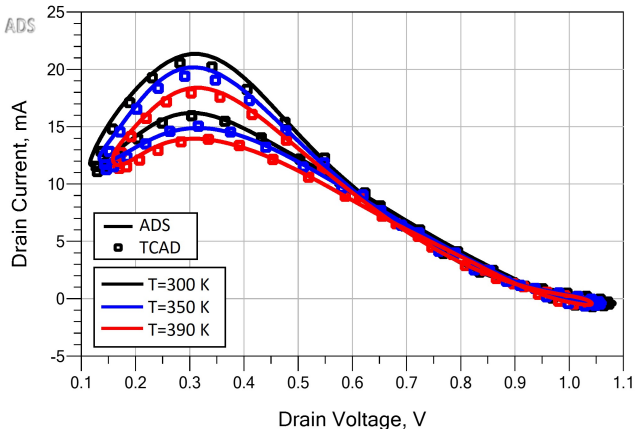

Fig. 6.3 Dynamic load lines at 2 dB gain compression and varying temperatures.

6.3 T-dependent LS analysis through T-Xpars

A temperature-dependent analysis of a low-power Class A FinFET PA operating at 70 GHz is performed with $N_{\mathrm{H}} = 10$ harmonics. The DC bias is $V_{\mathrm{G}} = 0.675$ V and $V_{\mathrm{D}} = 0.6$ V, the input port is here unmatched and terminated with the same 50 Ω impedance used to extract the Xpars, the drain port is loaded with $Z_{\mathrm{opt}} = 53 + \mathrm{j}\,6\ \Omega$, which differs from the 50 Ω used for the Xpar extraction, and harmonics are shunted by ideal tuners, hence they also differ from the termination used for the Xpar extraction. The T-Xpar model in ADS is validated against TCAD simulations for a set of temperatures different from the ones used for the model extraction in the range [310-390] K [89].

Fig. 6.3 shows the DLLs on Z_{opt} at $T = 300$ K, 350 K and 390 K. The agreement between TCAD and ADS simulations is always satisfactory, despite the operating condition differs from the model extraction condition both for the load and the temperature. The DLLs show a significant thermal knee walk-out, which is in line with the results of Chapter 5. Moreover, a global reduction of the overall drain current is reported due to the mobility degradation, hence the optimum load extracted at room temperature will be sub-optimal at higher temperatures. Fig. 6.4 shows that the output power diminishes as a function of T. The stage non-linearity is clearly reflected by the different behavior in back-off and at saturation: there is a mild reduction of thermal sensitivity at higher input power due to the knee voltage walk-out and an opposite behavior at lower input power (see Fig. 6.4b). In Fig. 6.5, the available gain confirms these considerations. Moreover, as shown in Fig. 6.6,

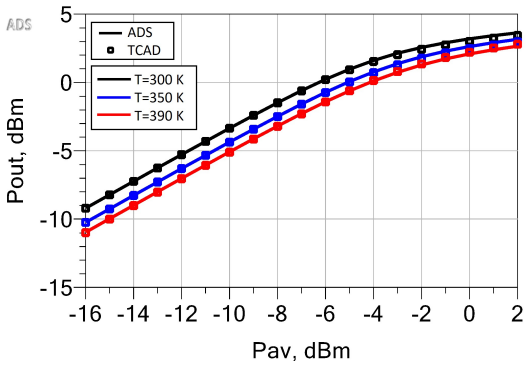

(a) P_{out} vs. available power at different T.

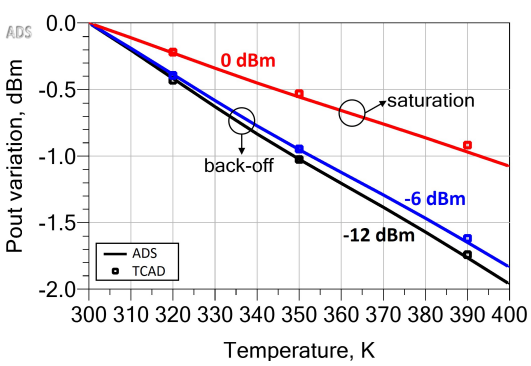

(b) P_{out} variation vs. T at different P_{av}.

Fig. 6.4 Output power and its variation for the Class A PA.

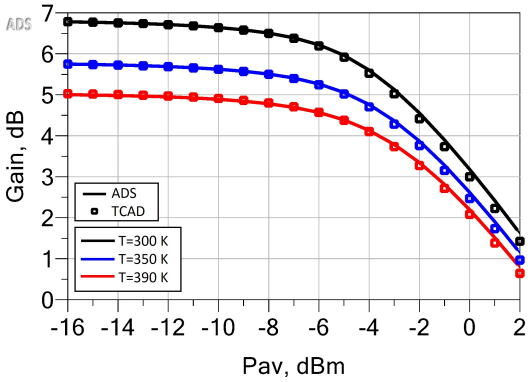

Fig. 6.5 Gain at different T.

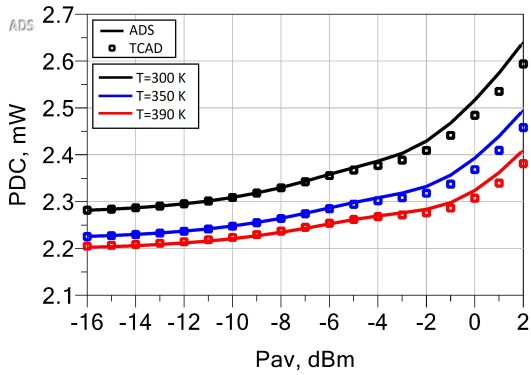

Fig. 6.6 DC consumption at different T.

the DC power consumption decreases with T, but increases in compression due to the drain current waveform clipping. Once the T-Xpar model is validated with TCAD simulations over selected conditions, it can be exploited to provide the global trend of several quantities, i.e. output power, efficiency, PAE. For example, the PAE behavior is quite complex: Fig. 6.7 shows an overall reduction of efficiency with increasing T. Interestingly, the most significant spread occurs around 4 dB to 6 dB of output power back-off, where it is close to 10 percentage points, while in compression it is more limited (around 5 points). Finally, the T-Xpar model allows also to evaluate the device input impedance reported in Fig. 6.8: it turns out to strongly depend on T in back-off and less in compression, opening the way to the identification of drive/back-off conditions where the PA input matching is less sensitive to self-heating.

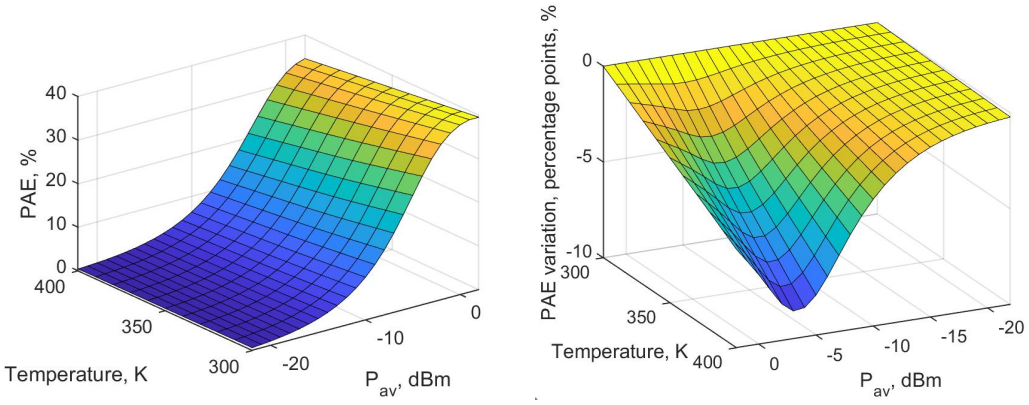

(a) PAE of the Class A PA.

(b) PAE variation of the Class A PA.

Fig. 6.7 PAE and its variation as a function of temperature and available power.

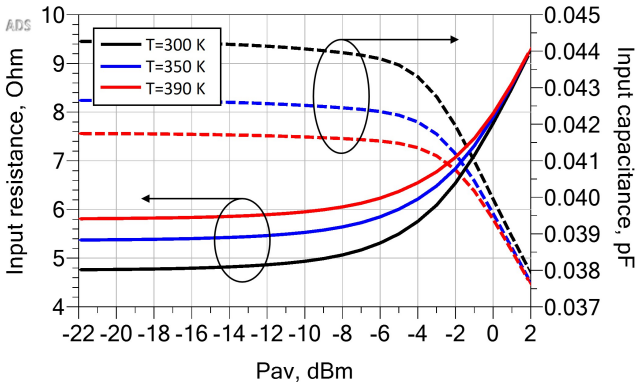

Fig. 6.8 Input impedance as a function of temperature and available power.

6.4 Self-heating LS analysis through T-Xpars

The LS analysis is repeated to account for self-heating effects in the FinFET power amplifier [90], hence the ADS implemented model is slightly different from the previous one. From the simulation standpoint, when a time-varying temperature is present on the *Temp* terminal in Fig. 6.1, the model predicts an instantaneous variation of the device electrical characteristics, which is of course not physical since it does not include thermal dynamics, low-frequency dispersion, etc. To account for thermal dynamics and self-heating, instead, an external lumped *RC* thermal network is coupled to the T-Xpar model as shown in Fig. 6.9 [92]. The instantaneous dissipated power in the device is calculated through an *SDD* (Symbolically Defined Device of ADS) block, exploiting current probes in the circuit as controlling currents at selected ports. The instantaneous power is then fed as the current flowing through the *RC* thermal impedance block, yielding the junction temperature. The latter is applied to the *Temp* terminal of the T-Xpar model, dynamically selecting the values of the X-parameters as a function of the time-varying temperature. In this example, the thermal resistance is varied from 0.33 to 1 K/μW (calculated as already shown in Section 5.2, Fig. 5.3), while the thermal capacitance is sized so as to yield a first-order thermal cut-off frequency of 10 kHz. Notice that from the electrical standpoint, Xpars represent a quasi-memoryless model, hence the slow thermal dynamic is here entirely due to the thermal impedance. The ADS Xpar model is validated through self-heating LS simulations performed by the in-house TCAD code, which solves self-consistently the SHS system (2.38). Fig. 6.10 shows that the ADS model correctly predicts the FinFET self-heating: as expected in a class-A stage, the junction temperature decreases as a function of the input power, while in back-off the thermal dissipation is larger due to the DC power consumption and the lower PA efficiency.

6.4.1 SH analysis with pulsed input power

To highlight the capability of the implemented self-consistent dynamic electrothermal model, the FinFET PA is tested under pulsed RF operation [93, 94]. In this analysis, the thermal resistance is set to 1 K/μW and the carrier frequency is equal to 70 GHz, which is the operating frequency of the designed stage. The input power is switched 'ON' ($P_{\mathrm{av}} = -2$ dBm) and 'OFF' ($P_{\mathrm{av}} = 0$ dBm) with 50% duty cycle. Rise and fall

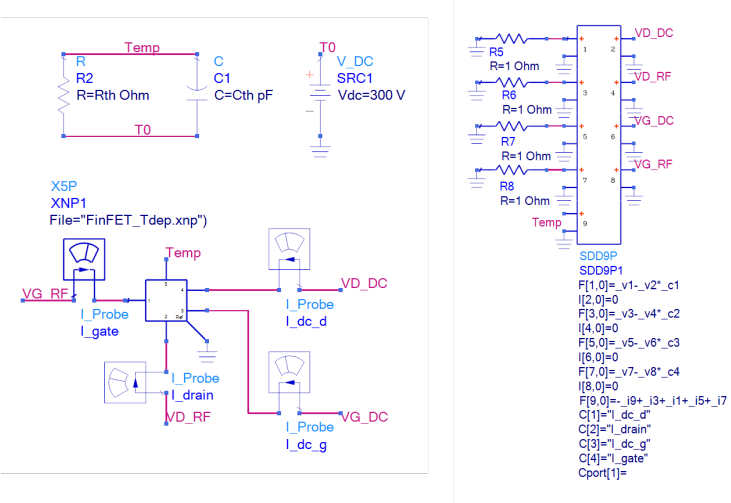

Fig. 6.9 Circuit implementation of the dynamic self-consistent thermal model. An SDD is used to compute the instantaneous power of the device, which is fed to the thermal impedance to evaluate the dynamic temperature value used as a parameter for the T-Xpar model. This implementation follows [14].

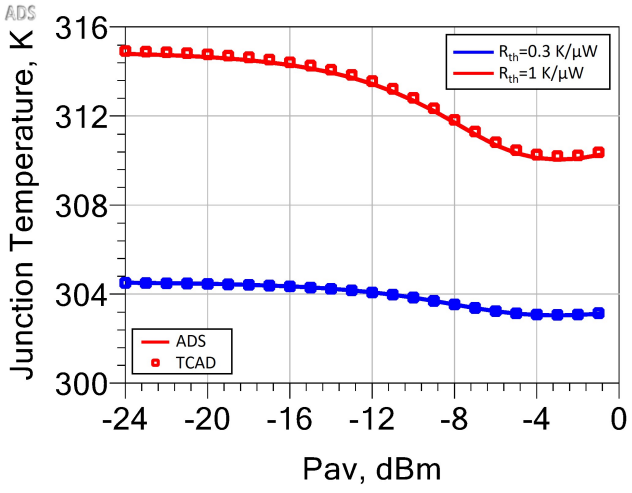

Fig. 6.10 Comparison of the FinFET junction temperature predicted, respectively by the self-consistent TCAD simulations and the ADS model.

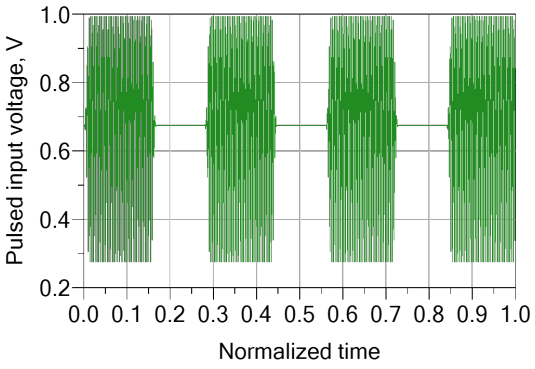

Fig. 6.11 Example of pulsed input voltage. The time range is normalized to 4 periods.

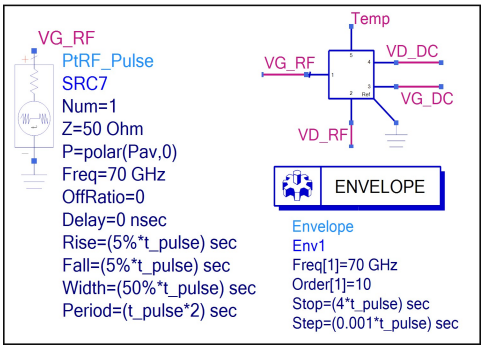

Fig. 6.12 Circuit implementation of the pulsed thermal self-heating analysis.

time are set equal to 5% of the pulse duration. The resulting modulated input voltage, shown in Fig. 6.11, is obtained at circuit level using the *PtRF_Pulse* component of ADS and *Envelope* simulations necessary to model the slow thermal dynamics of the stage. As shown in Fig. 6.12, the *PtRF_Pulse* component allows to create a pulse modulated RF carrier with a frequency defined by the 'Freq' parameter, i.e. 70 GHz. Concerning the pulse amplitude, the 'OffRatio' defines the low state of the pulse (0 dBm) relative to the high state, defined by 'P' (-2 dBm). The input power source is represented by an envelope signal characterized by a pulse duration 't_pulse' with a certain 'Rise' and 'Fall' time (5%t_pulse) and a duty cycle defined by the the 'Width' parameter (50%t_pulse). The *Envelope* component of ADS, which is used since the pulse duration is much lower than the RF carrier duration, is basically defined by fundamental frequency (70 GHz) and the maximum number of harmonics, namely 'Order' (10 harmonics).

Three different pulse durations are exploited, namely 5 ms, 50 μs and 0.5 μs. Given the thermal cut-off frequency of 10 kHz (thermal time constant of 15 μs) we expect that the FinFET temperature follows the time-varying power envelope in the slower pulse case, exhibits a noticeable delay (rise/fall times) with respect to the power pulses in the intermediate case and is essentially insensitive to power variations in the last, faster pulse, case. Fig. 6.13a shows the temperature baseband envelope in the three cases, confirming the expectations. Notice from Fig. 6.10 that the selected input power (-2 dBm) induces a temperature decrease of about 5 K. Therefore if the pulse duration is long enough the device exhibits thermal cooling. Fig. 6.13b confirm the results showing the phase difference between the temperature baseband envelope and the output power fundamental envelope. In the

slower case, temperature and power envelopes are in phase, while in the faster pulse case the temperature variations are essentially null over the entire pulse cycle. The hysteresis, typical of the thermal dynamic behavior [14], is significant for a pulse duration close to the thermal time constant (intermediate case). Fig. 6.14 shows the fundamental envelope of the PA available and output power in the three cases. Since the output power is about 2 mW and the available power 0.3 mW, the gain of the stage is about 8 dB. When the pulse is 'ON', the temperature and, consequently, the output power assume a constant value over the pulse duration, which is equal to 2 mW in the slower case and 1.95 mW in the faster case (see again Fig. 6.13b). Moreover, as highlighted in the inset, the pulsed power is modulated by thermal effects, producing in the intermediate case a non constant temperature over the pulse duration, as already shown in Fig. 6.13a, and a non constant output power, leading to the hysteresis behavior of Fig. 6.13b.

6.4.2 Comparison between Class A and Class B stages

The self-heating LS analysis in pulsed operating conditions is repeated for a Class B FinFET PA since this stage is expected to operate differently from the Class A when thermal dynamics is present. To this aim, the T-Xpar model is extracted changing the gate voltage from 0.675 V, corresponding to class A stage, to 0.5 V, corresponding to class B stage. TCAD LS simulations are repeated for the extraction of the X-parameters with no differences with respect to the previous case. The T-Xpar for the Class B stage is imported in Keysight ADS, where the simulation setup is the same of Figs. 6.9 and 6.12.

In Fig. 6.15 the analysis of the pulsed power amplifier is reported: in order to compensate the lower class B gain, the available input power is adapted to keep the same output power in both Class A and Class B stages. Fig. 6.15a shows the predicted temperature as a function of the output power for 3 different pulse lengths, the same used in the previous case, while Fig. 6.15b shows the temperature variation as a function of time. There is an expected opposite behavior of the class A and B stages: the former is hotter when the pulse is 'OFF', while the latter gets cooler. The thermal shunt, though, makes temperature variations to be quenched by increasing the pulse speed, in fact temperature is almost constant in the faster case. Fig. 6.16 reports the output power variation as a function of the (normalized) time, highlighting the capability of the T-Xpar model of predicting the P_{out} thermal dispersion. From

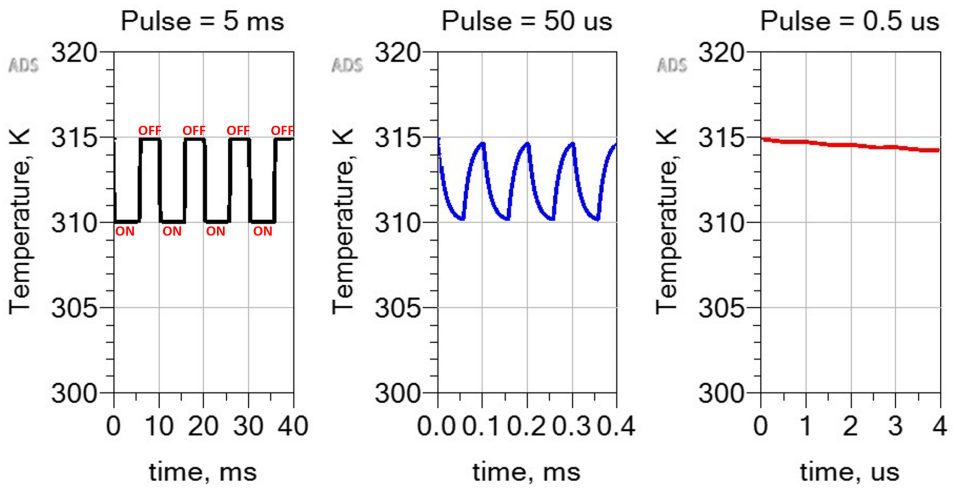

(a) Dynamic temperature variation over the pulse cycle.

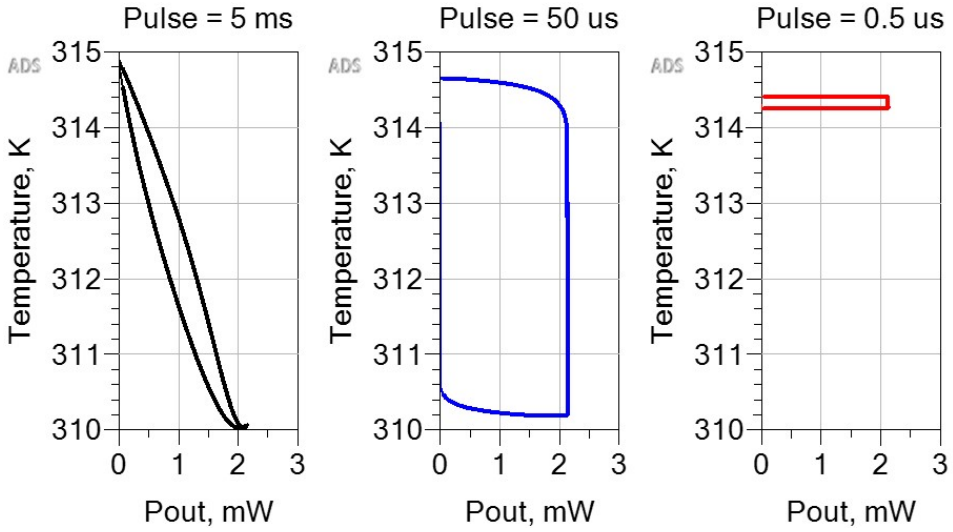

(b) Dynamic temperature variation as a function of the output power over the pulse cycle.

Fig. 6.13 Results of the pulsed mode analysis of the matched FinFET in class A for the 3 different pulse durations.

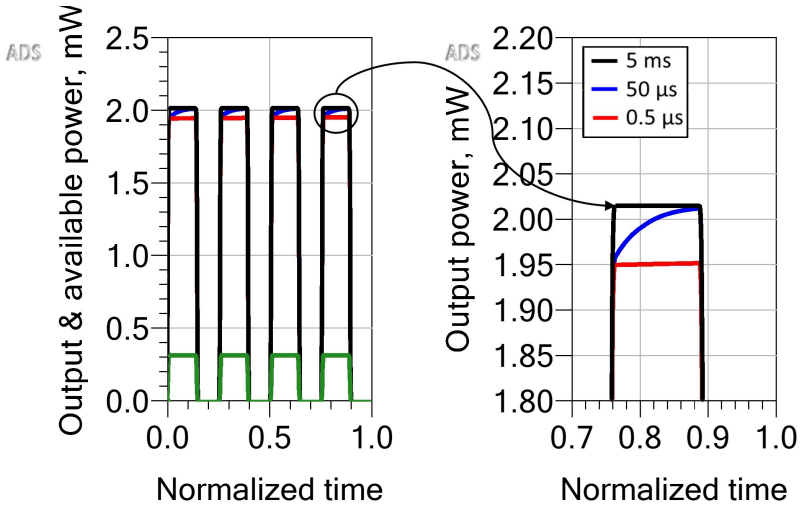

Fig. 6.14 Variation of the PA output power as a function of time (normalized over 4 periods) for three different pulse durations. The green curve represents the input power pulse envelope. The right figure shows the details of the output power envelope time-dependency during the on state.

the zoom of Fig. 6.16b the opposite behavior of the two stages is further highlighted: the output power is constant during the 'ON' state of the slower and faster cases, and reaches a maximum value at 5 ms for the Class A and at 0.5 μs for the Class B. The intermediate case is characterized by a non constant output power, passing from a maximum to a minimum value in the Class A stage and from a minimum to a maximum in the Class B one. Finally, Fig. 6.17 shows results obtained for a pulse length of 0.5 μs sweeping the gate voltage from 0.5 V, corresponding to the Class B stage, to 0.675 V, corresponding to the Class A stage. In particular, the temperature at baseband linearly increases with respect to the gate voltage, going from 310 K to 350 K. On the other hand, the output power decreases from 1.8 mW at 0.5 V to about 1.7 mW at 0.62 V, where it starts to increase up to 1.8 mW at 0.675 V. This analysis demonstrates that the implemented model can continuously interpolate among the Xpar data both in terms of temperature and gate bias.

6.5 Conclusions

In this chapter, an efficient implementation of a dynamic electro-thermal model for a 54 nm FinFET device is directly extracted from LS TCAD simulations via T-dependent Xpars in a 50 Ω environment at three different temperatures: 300 K,

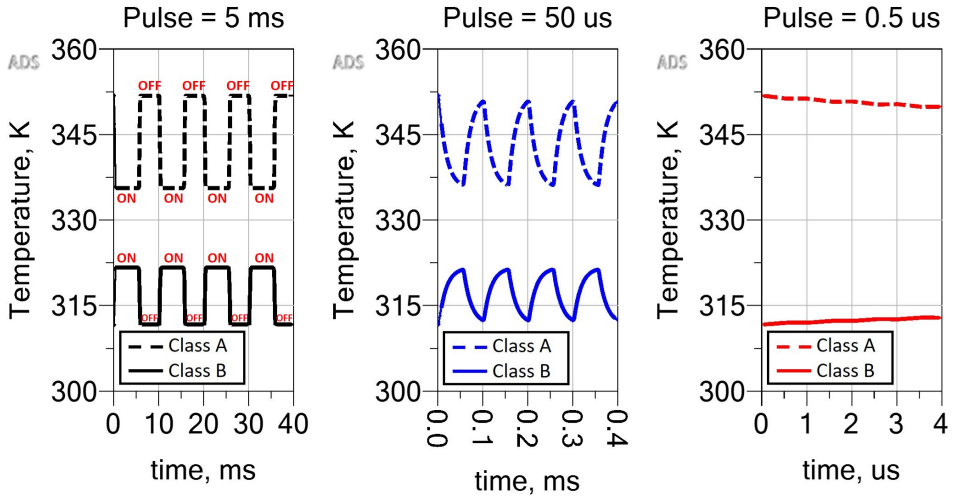

(a) Dynamic temperature variation over the pulse cycle.

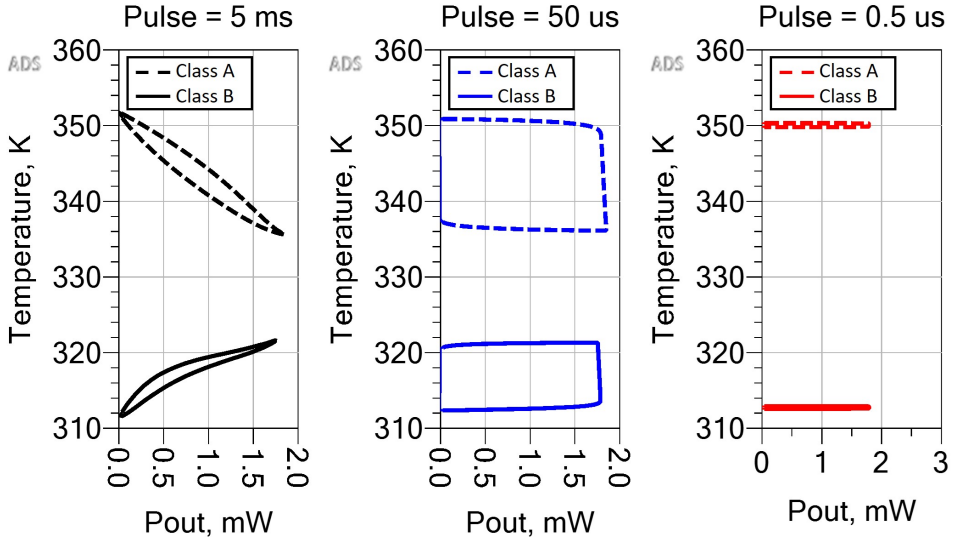

(b) Dynamic temperature variation as a function of the output power over the pulse cycle.

Fig. 6.15 Results of the pulsed mode analysis of the matched FinFET in class A and class B for the 3 different pulse durations.

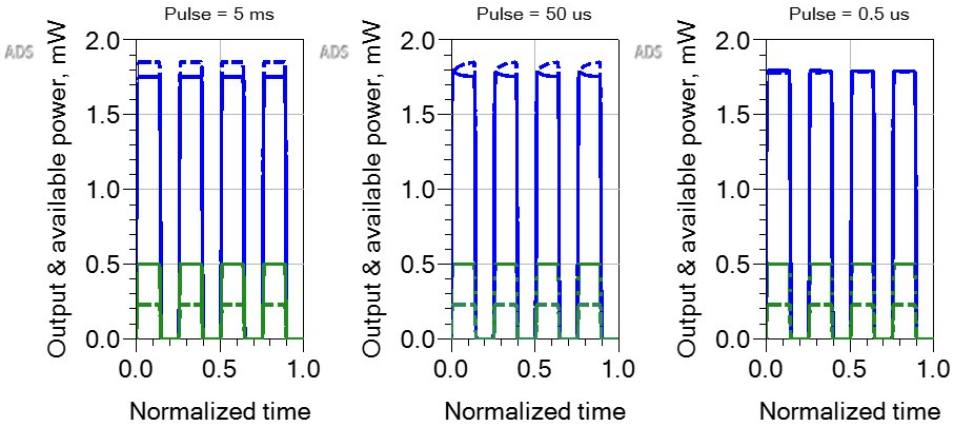

(a)

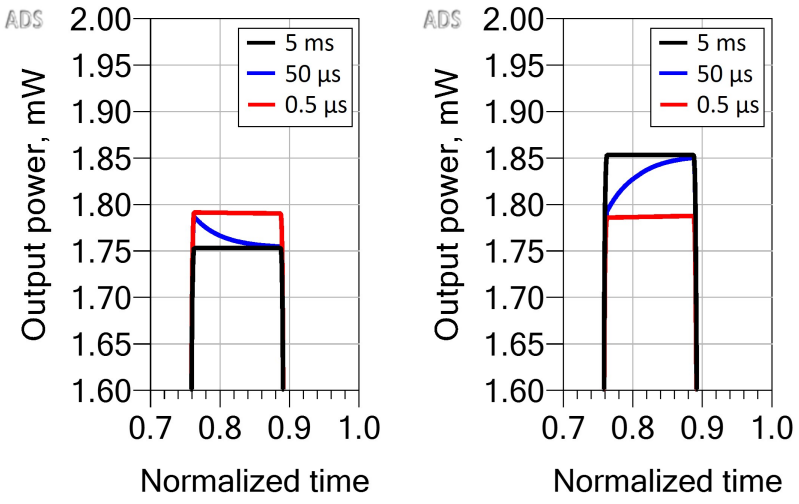

(b)

Fig. 6.16 Results of the pulsed mode analysis of the matched FinFET: (a) output power variation over the cycle in class A (dashed lines) and class B (solid lines) and (b) detailed view of the output power behavior in the 'ON' state for the 3 different pulse durations.

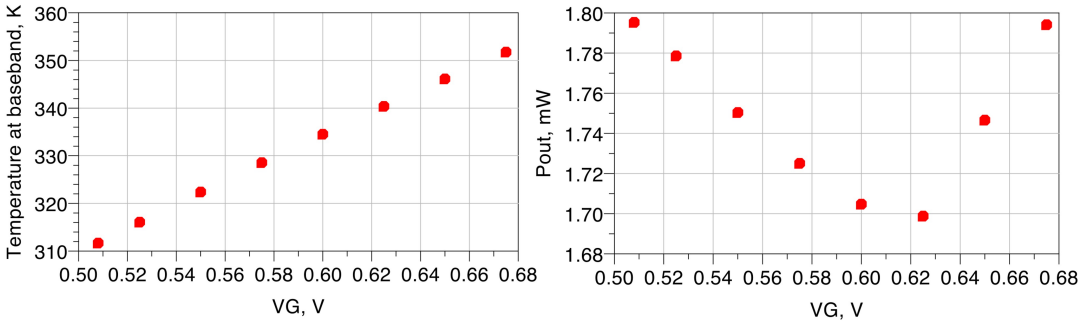

Fig. 6.17 Results of the pulsed mode analysis of the matched FinFET: (left) temperature at baseband and (right) output power at the RF envelope at different gate bias voltages, from class A to class B, for a pulse length of 0.5 μs.

340 K, 380 K. The model is validated against LS TCAD analysis, including self-heating, by simulating a class A power amplifier with a single tone excitation in the range [310-390] K. In particular, T-dependent LS simulations confirm the thermal degradation of the FinFET PA in terms of output power, gain, efficiency, etc., in all operating conditions. As an example, the PAE shows a significant spread in back-off region, reaching a variation of 10 percentage points. Moreover, the self-heating LS analysis is performed for two different thermal impedances with cut-off frequency of 10 KHz and exhibits a reduction of the junction temperature as a function of the input power up to 5 K for $R_{\text{th}} = 1$ K/μW. Then, the ADS envelope analysis is exploited to demonstrate the effect of PA self-heating in pulsed operating conditions: three different pulse durations are selected to highlight the role of thermal memory in the behavior of both temperature and output power. It can be noticed that if the pulse duration is long enough, the device exhibits thermal cooling. The envelope analysis is repeated for a Class B PA, showing an opposite behavior with respect to the Class A stage: during the 'OFF' state, the latter is hotter and the Class B stage is cooler. The proposed approach represents an efficient way to evaluate the impact of temperature dynamics on PA performance and it is worth noticing that the same analysis is not possible adopting a mere Xpar model at 300 K.

Chapter 7

TCAD analysis of GaN HEMT dynamics through the trap rate equation

GaN HEMT devices are a sufficiently mature technology in high-power and high-frequency applications and they are widely exploited in communication and space power applications. Nonetheless, nitride-based materials are characterized by trapping mechanisms, which limit the RF device performances and need to be deeply studied. Various characterization techniques have been proposed to identify the trap dynamic behavior, linking the trap occupation to the gate/drain current delay in terms e.g. of rise/fall time in the response to specific stimuli such as voltage steps or pulses [95, 96]. Pulsed S-parameters and noise measurements are used to assess the trap-related dispersion of AC and RF parameters [97]. In fact, the peculiar low frequency dispersion of the device Y parameters has become a standard method to characterize the trap dynamics [5]. Since characterizations typically provide only the device terminal current dynamics, TCAD analysis represents a unique opportunity to investigate the effect of the trap localization, especially when trap density varies in the device volume.

In this chapter, a TCAD sensitivity analysis of a Fe-doped AlGaN/GaN HEMT device in DC and AC conditions is presented. The simulations are performed solving the PDD-ECE-TRE system (2.46), introduced in Chapter 2, in order to provide an accurate insight into the impact of trap dynamics in the GaN-based structure. The

TCAD sensitivity analysis is carried out exploiting the GF-based approach through the variation of selected trap model parameters, such as the trap concentration and the trap energy. The proposed technique provides a more relevant application example of the GF approach, allowing for fast and accurate investigation of trap effects in GaN HEMT devices, which are continuously evolving, e.g. by introducing Fe doping.

7.1 Device under analysis

A HEMT structure of 0.150 μm gate length, whose dimensions are set in line with the up-to-date technologies [98], is considered in Fig. 7.1. The AlGaN barrier layer is 15 nm thick with 25% Al mole fraction, while the GaN layer is divided into a 5 nm thick channel region and a 2 μm deep buffer region, both with residual donor doping of 10^{15} cm^{-3}. The buffer region is characterized by a Fe-induced deep acceptor-like trap concentration $N_{\mathrm{t}} = 10^{18}$ cm^{-3} with nominal energy $E_{\mathrm{Ct}} = E_{\mathrm{C}} - 0.45$ eV and electron and hole capture cross-sections $\sigma_n = \sigma_p = 3 \times 10^{-16}$ cm^2. Fig. 7.1 shows the details of the HEMT structure, including the source and drain doped regions and the S/D contacts. The TCAD analysis is carried out including the GaN spontaneous polarization and both the AlGaN spontaneous and piezoelectric polarization, corresponding to $-2.9 \cdot 10^{-6}$ C/cm^2 and $-5.04 \cdot 10^{-6}$ C/cm^2, respectively, following Table 2.5. The resulting net polarization charge at the AlGaN/GaN interface is $q_{\mathrm{PE}} = 2.14 \times 10^{-6}$ C/cm^2 with 90% activation, hence $\sigma_{\mathrm{pol}} = 1.2 \times 10^{13}$ cm^{-2}. On the other hand, the polarization charge at the interface with contacts and passivation layers is exactly compensated. The polarization model implemented in the in-house software is the Synopsys `Simplified strain model` [26]. Furthermore, a fixed interface negative charge $\sigma_{\mathrm{int}} = -2 \times 10^{12}$ cm^{-2} is also added at the barrier/passivation interface. The electron mobility includes dependency on lattice temperature and doping, while velocity saturation is modelled with the Caughey-Thomas model with $v_{n,\mathrm{sat}} = 2.5 \times 10^7$ cm/s for both AlGaN and GaN. Fe doping acts like a deep acceptor-like trap with trap energy $E_{\mathrm{t}} = E_{\mathrm{C}} - 0.45\,\mathrm{eV}$ (being E_{C} the conduction band edge) and electron and hole capture cross-sections $\sigma_n = \sigma_p = 3 \times 10^{-16}$ cm^2 [5]. Finally, a contact resistance of 0.4 Ω mm is considered at the source and drain terminals.

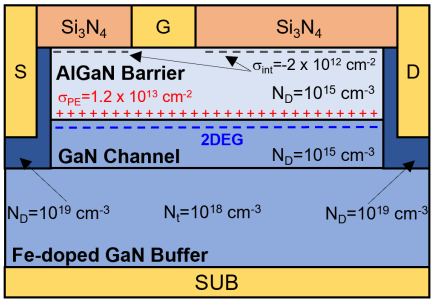

Geometrical Parameter	Value (nm)
Si_3N_4 Passivation Thick.	100
AlGaN Barrier Thick.	15
GaN Channel Thick.	150
GaN Buffer Thick.	2000
Gate Length	150
Gate-Source Length	800
Gate-Drain Length	2000

Fig. 7.1 Simulated HEMT structure.

7.2 DC sensitivity analysis

The DC simulation of the Fe-doped GaN HEMT is performed at different drain and gate voltages. Figs. 7.2a and 7.2b show, respectively, the device output characteristics and transcharacteristics, which exhibit a saturation current $I_{D,ss}$ of 1.15 A/mm and a threshold voltage of -2.5 V. The occupied trap concentration n_t reaches a maximum value of 10^{18} cm^{-3} in the buffer region immediately below the channel, then decreases moving away from the channel down to 10^{15} cm^{-3} (see Fig. 7.3). Static performance of GaN-based HEMTs are strongly influenced by the type of traps and their localization [99], as well as by the device geometrical dimensions, e.g. through the variation of access region length [100] and barrier thickness [36] or the addition of a GaN cap layer [101]. As shown in Fig. 7.4, the threshold voltage is insensitive to the increased gate-source length from 0.8 to 1.2 μm, while the saturation current is reduced by the greater access resistance and the presence of barrier/passivation traps along a higher L_{GS}. Moreover, Fig. 7.5 shows that a lower AlGaN barrier thickness of 12 nm not only reduces the value of $I_{D,ss}$, but leads also to a higher threshold voltage. Finally, the presence of a GaN cap layer (see Fig. 7.6) leads to a slightly greater 2DEG density, a consequent shift of the threshold voltage towards negative values and a significant increase of the drain saturation current, with no effects on the output resistance, as shown in Fig. 7.7. This choice reduces the current collapse due to gate-lag and drian-lag and improves the cut-off frequency [101].

As anticipated, the presence of traps significantly affects the device performance in DC conditions: as shown in Fig. 7.8, Fe-doped buffer traps lead to a clear reduction of the output conductance, a strong degradation of the saturation current

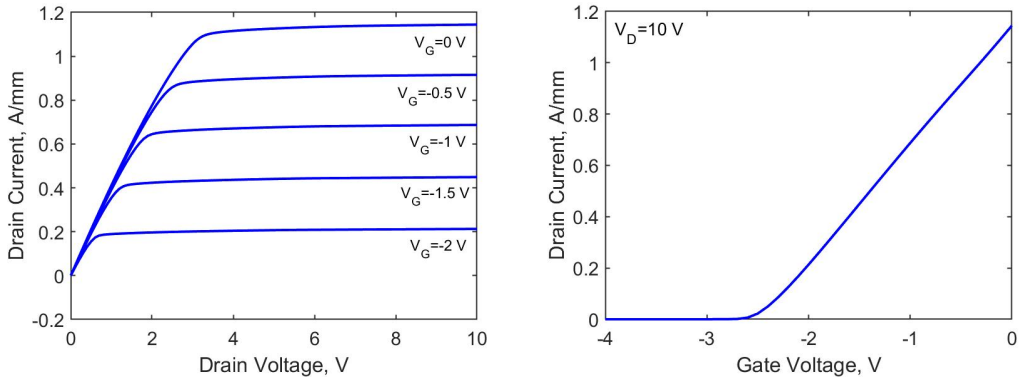

(a) HEMT output characteristics. (b) HEMT transcharacteristic at $V_{\mathrm{D}} = 10$ V.

Fig. 7.2 DC drain current of the GaN HEMT device in presence of traps.

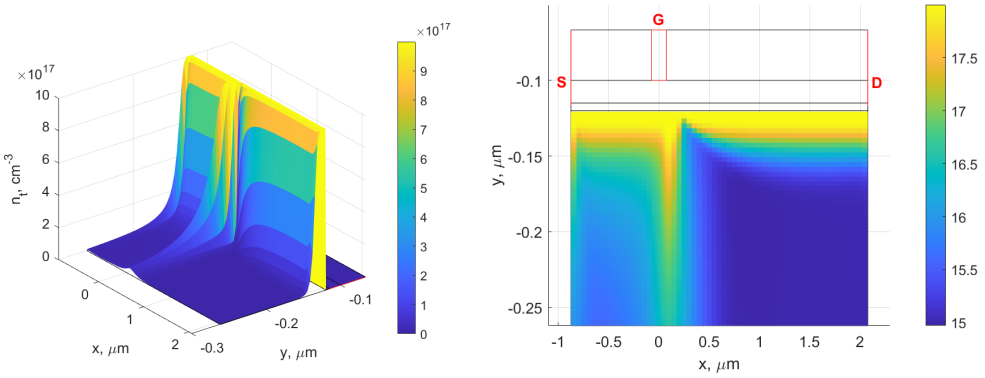

(a) 3D distribution in linear scale. (b) 2D distribution in logarithmic scale.

Fig. 7.3 Spatial distribution of the occupied trap concentration at $V_{\mathrm{D}} = 10$ V and $V_{\mathrm{G}} = 0$ V.

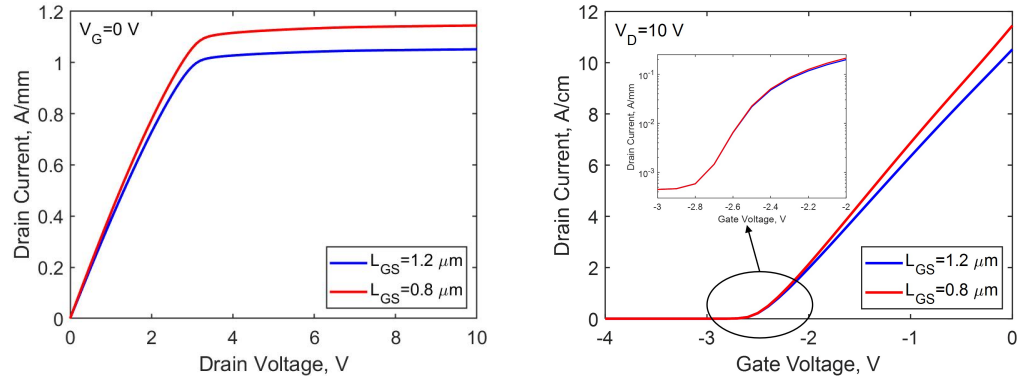

(a) HEMT output characteristic at $V_{\mathrm{G}} = 0$ V for different L_{GS}. (b) HEMT transcharacteristic at $V_{\mathrm{D}} = 10$ V: the inset is a zoom in logarithmic scale.

Fig. 7.4 DC drain current for two different L_{GS}.

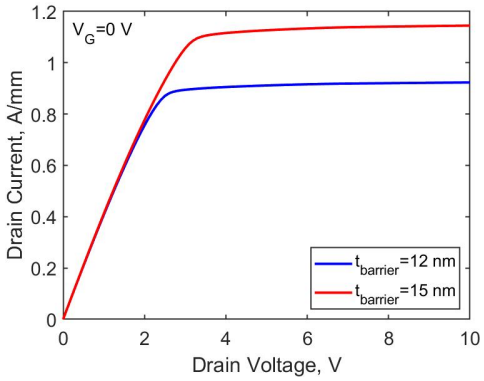

(a) HEMT output characteristic at $V_G = 0$ V.

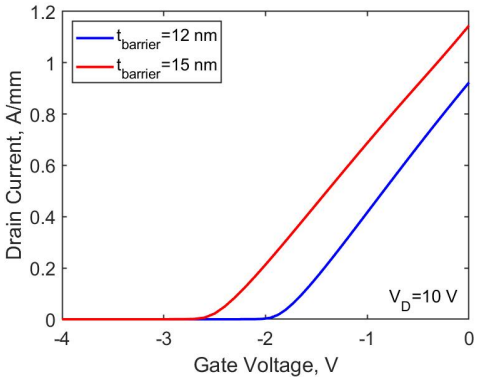

(b) HEMT transcharacteristic at $V_D = 10$ V.

Fig. 7.5 DC drain current for two different AlGaN barrier thicknesses.

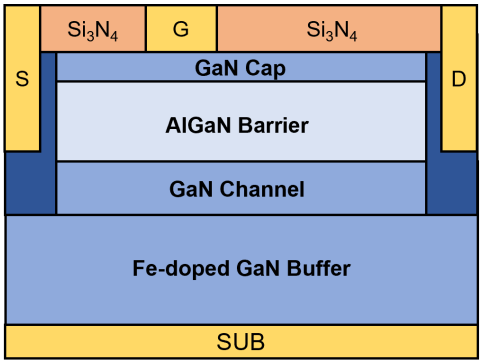

Fig. 7.6 HEMT structure with GaN cap layer.

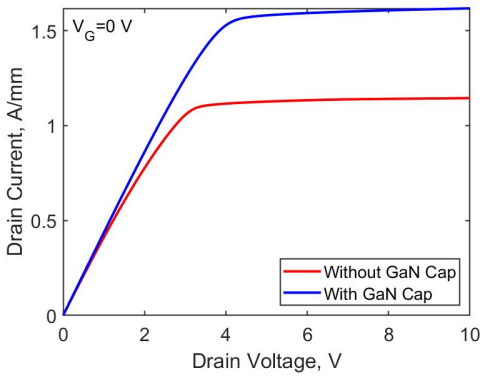

(a) HEMT output characteristic at $V_G = 0$ V.

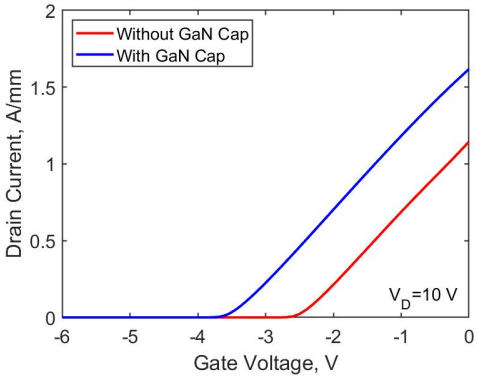

(b) HEMT transcharacteristic at $V_D = 10$ V.

Fig. 7.7 DC drain current for two different AlGaN barrier thicknesses.

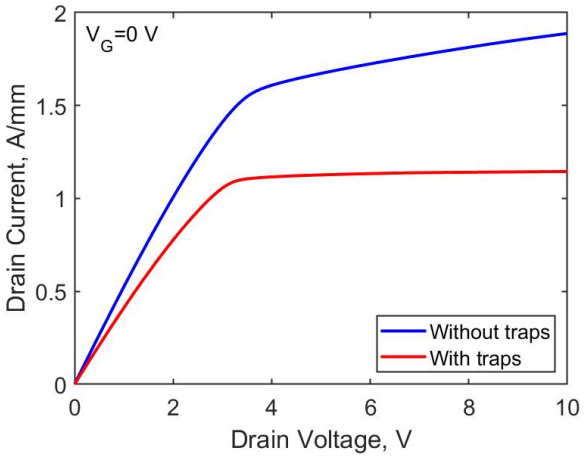

Fig. 7.8 HEMT output characteristics at $V_G = 0$ V with and without traps.

and a consequent increase of the threshold voltage. Their effect is dependent on both the localization inside the device and on the trap model parameters, i.e. concentration, energy level, cross section, etc. In this scenario, a complete DC sensitivity analysis is useful to understand the impact of traps with respect to the variation of a trap model parameter: the analysis can be carried out by repeated TCAD simulations, but the GF-based approach is exploited, as in the previous chapters, since it provides significant numerical advantage. First, the DC sensitivity analysis is performed varying the trap concentration N_t, solving the PDD-ECE-TRE system (2.46), varying N_t by $[\pm 5\%, \pm 10\%, \pm 15\%]$ with respect to the nominal case in order to find a *reference solution* (incremental method, INC). The INC solution is used to validate the GF-based analysis: GFs are extracted in DC conditions at nominal N_t and exploited to calculate the drain current variation according to (4.50). As shown in Fig. 7.9, the larger is the trap concentration, the higher the number of occupied traps and the lower the drain current [5]. In fact, Fe-doped traps are acceptor-like traps responsible of the capture/emission of electrons from/to the conduction band, therefore with a higher N_t, more electrons can be captured from the channel region leading to the increase of n_t and the reduction of the drain current. Then, the analysis is repeated taking into account the trap energy E_t as model parameter to be varied: this corresponds to vary the energy difference $E_{Ct} = E_C - E_t$ in the range $[0.4 - 0.5]$ eV with respect to the nominal value $E_{Ct} = 0.45$ eV. Moving E_t away from E_C, the electron emission rate to the conduction band decreases, hence the number of occupied traps increases reducing the electrons of the channel region and leading to a lower drain current,

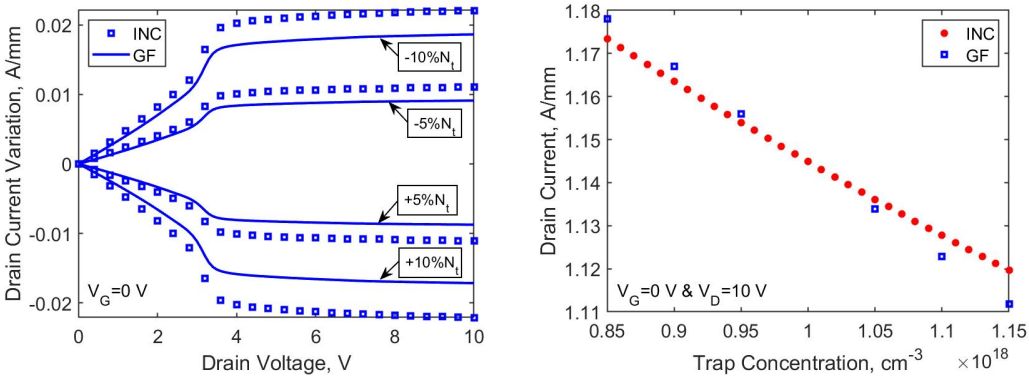

(a) Drain current variation with varying trap concentration at $V_G = 0$ V.

(b) Drain current as a function of the trap concentration at $V_G = 0$ V and $V_D = 10$ V.

Fig. 7.9 DC drain current and its variation with varying trap concentration.

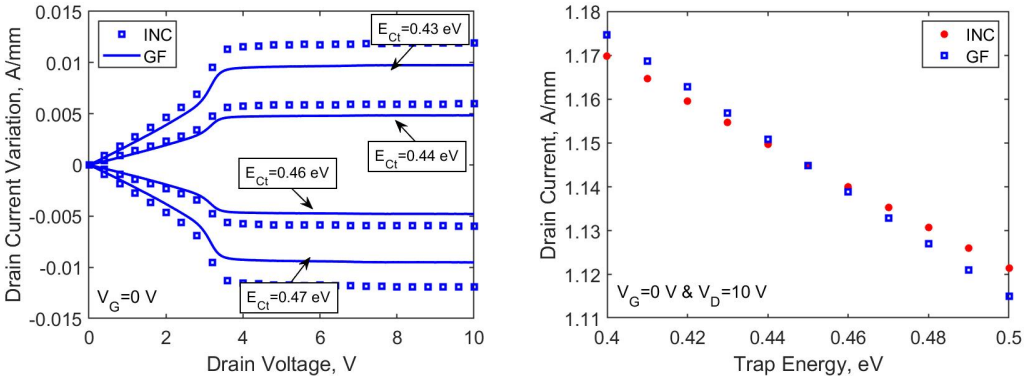

(a) Drain current variation with varying trap energy at $V_G = 0$ V.

(b) Drain current as a function of the trap energy at $V_G = 0$ V and $V_D = 10$ V.

Fig. 7.10 DC drain current and its variation with varying trap energy.

as shown in Fig. 7.10. Both the sensitivity analyses demonstrate a good agreement between the GF approach and the INC method, which is more numerically intensive.

7.3 AC sensitivity analysis

The effect of Fe-doped traps with respect to a trap parameter variation is now investigated in AC conditions through the extraction of the GaN HEMT Y parameters. The analysis is carried out taking as DC bias point $V_D = 10$ V and $V_G = -2.22$ V,

corresponding to $10\%I_{\mathrm{D,ss}}$, in the perspective of investigating the trap effects on the typical bias condition for power amplifiers. The problem is addressed with the AC sensitivity analysis, at different trap energy levels, performed solving the PDD-ECE-TRE system (2.46) with $N_{\mathrm{H}} = 1$, an input tone of 1 mV amplitude recursively applied to each terminal and a tone frequency in the range between 10 Hz to 1 MHz. At each frequency, repeated AC simulations for two different trap energies $E_{\mathrm{Ct}} = [0.445, 0.455]$ eV are performed to find the HEMT Y-matrix following (4.52), corresponding to the reference solution (incremental method, INC). While the reference solution is estimated with repeated AC simulations at different trap energies, the GF-based analysis only requires one simulation at nominal E_{Ct}, giving a great advantage in terms of computational cost and an excellent agreement with the INC solution. In fact, CGFs are calculated with nominal Fe trap energy E_{t}, such that $E_{\mathrm{Ct}} = 0.45$ eV. Then, the current variation with varying E_{Ct} is obtained through (4.54b), and hence the Y parameters are evaluated according to (4.56).

The Y_{22} and Y_{21} components as a function of frequency are hereafter reported [6, 5]. The real part of Y_{22}, shown in Fig. 7.11a, is characterized by two corner frequencies, which are slightly shifted towards negative values with increasing E_{Ct}: the lower one is at around 464 Hz and the upper one at 20 kHz. In the imaginary part of Y_{22}, shown in Fig. 7.11b, Fe-doped traps are responsible of a positive peak at $f_{\mathrm{peak}} \approx 2.15$ kHz in $\mathrm{Imag}\{Y_{22}\}$. With decreasing E_{Ct}, the peak is shifted towards higher frequency values and the imaginary part of Y_{22} slightly increases. This TCAD technique allows for unique opportunities for a further insight on these results through the investigation of the local variation sources $\tilde{\mathrm{LS}}_k^{(\alpha)}$, according to (4.55). In particular, $\tilde{\mathrm{LS}}_k^{(\alpha)}$ highlights which parts of the device contribute to ΔY_{22}: the dominant contribution is found to be the local variation source of the trap rate equation at the drain contact $\tilde{LS}_{\mathrm{D}}^{(n_{\mathrm{t}})}$. Therefore, the imaginary part of the ratio $\tilde{LS}_{\mathrm{D}}^{(n_{\mathrm{t}})}/V_{1,\mathrm{D}}$, namely $\mathrm{Imag}\{\Delta Y_{22}^{(n_{\mathrm{t}})}\}$, is reported at different frequencies. Figs. 7.12 and 7.13 show the local variation source for $E_{\mathrm{Ct}} = 0.455$ eV (5 meV variation with respect to the nominal value) for the two frequencies $f_1 < f_{\mathrm{peak}}$ and $f_2 > f_{\mathrm{peak}}$. In general the source is mainly significant only in the buffer region below the gate where the position of $E_{\mathrm{F}n}$ modulates the trap occupation. $\mathrm{Imag}\{\Delta Y_{22}^{(n_{\mathrm{t}})}\}$ at f_1 is more concentrated at the source side of the channel and assumes positive values, while at f_2 it is more extended towards the drain contact and becomes negative. Fig. 7.14a shows that the real part of Y_{21} is rigidly shifted towards higher values with decreasing E_{Ct}, while the frequency peak at around 1 kHz is almost insensitive to

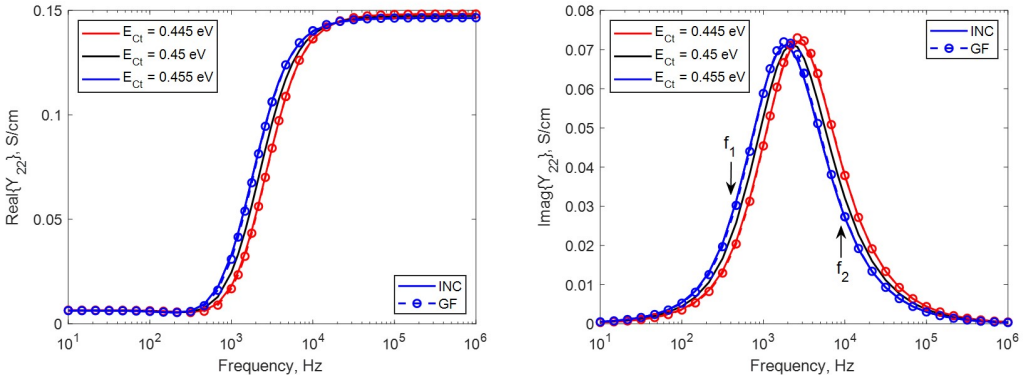

(a) Real part of the Y_{22} parameter. (b) Imaginary part of the Y_{22} parameter.

Fig. 7.11 Y_{22} parameter as a function of frequency at difference trap energy levels.

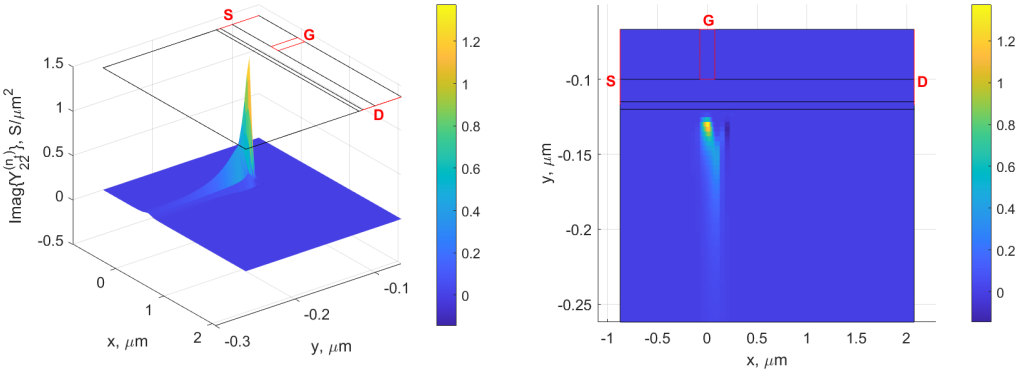

(a) 3D spatial distribution. (b) 2D spatial distribution.

Fig. 7.12 Local variation source at frequency $f_1 = 464$ Hz reported in Fig. 7.11b.

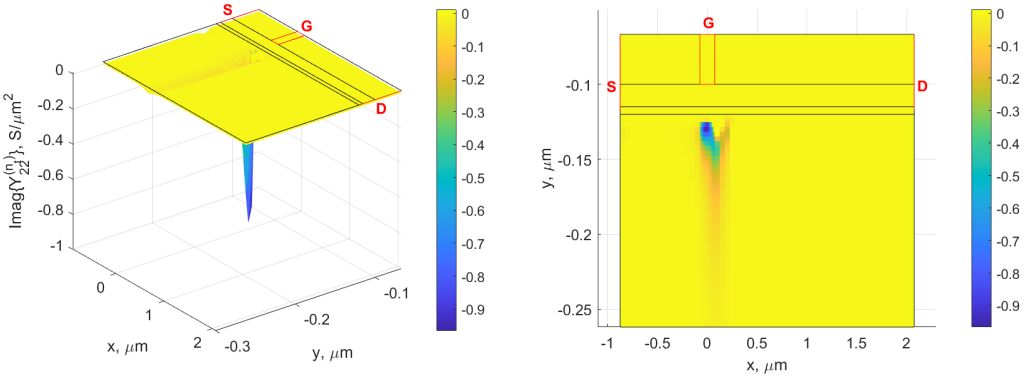

(a) 3D spatial distribution. (b) 2D spatial distribution.

Fig. 7.13 Local variation source at frequency $f_2 = 10$ kHz reported in Fig. 7.11b.

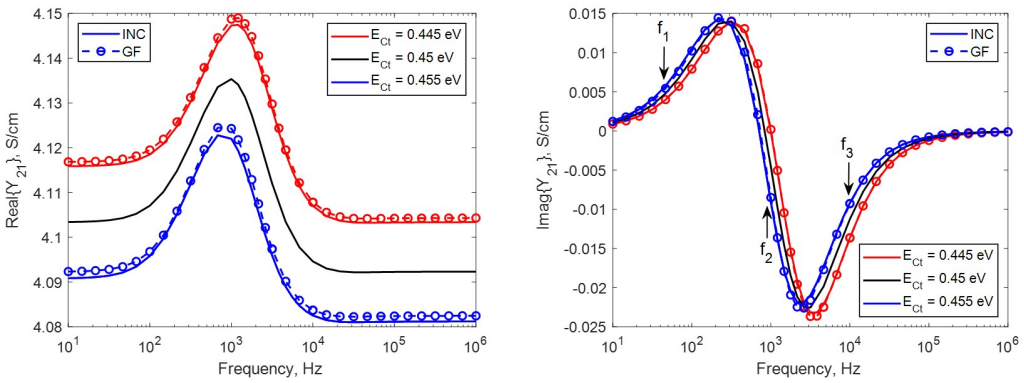

(a) Real part of the Y_{21} parameter.

(b) Imaginary part of the Y_{21} parameter.

Fig. 7.14 Y_{21} parameter as a function of frequency at difference trap energy levels.

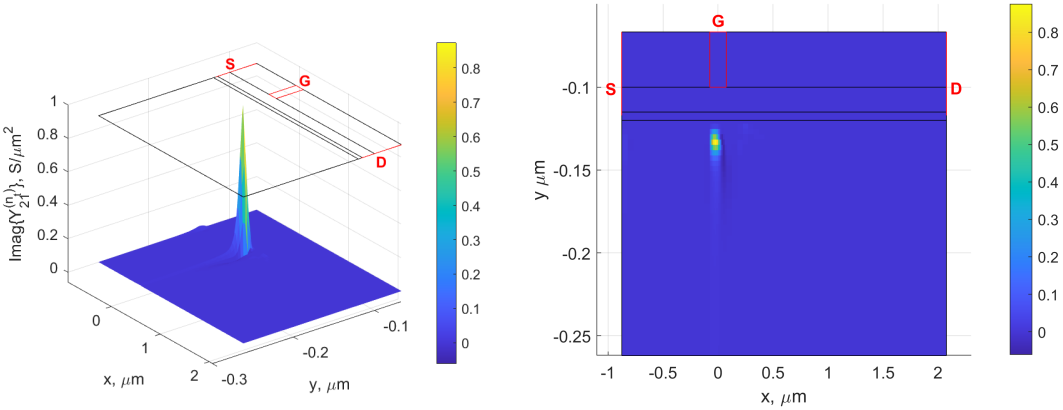

(a) 3D spatial distribution.

(b) 2D spatial distribution.

Fig. 7.15 Local variation source at frequency $f_1 = 46$ Hz reported in Fig. 7.14b.

trap energy variations. Fig. 7.14b exhibits two frequency peaks in the imaginary part of Y_{21} [5]: a positive peak at $f_{\text{peak,a}} = 250$ Hz and a negative peak $f_{\text{peak,b}}$ at around 3 kHz due to the presence of buffer traps. With decreasing trap energy level, the buffer peak shifts towards higher frequencies, while the surface peak is almost insensitive to E_{Ct} variations. Figs. 7.15, 7.16 and 7.17 show the imaginary part of the ratio $\tilde{LS}_{\text{D}}^{(n_t)}/V_{1,\text{G}}$, namely $\text{Imag}\{\Delta Y_{21}^{(n_t)}\}$ at three different frequencies. Going from f_1 to f_3, the local variation source is more distributed towards the drain and in depth of the buffer region: in particular it has positive values at frequency $f_1 < f_{\text{peak,a}}$ and mostly negative at f_2. At $f_3 > f_{\text{peak,b}}$ there is a sharp negative peak under the gate at source side and a broad positive region under the whole gate area.

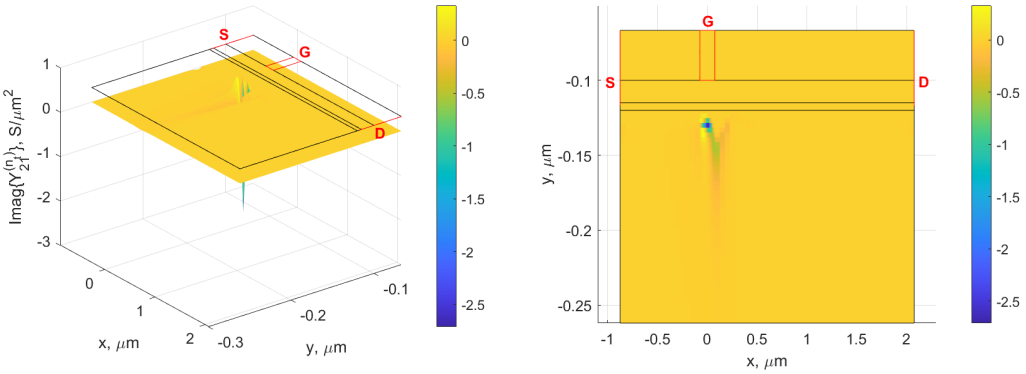

(a) 3D spatial distribution. (b) 2D spatial distribution.

Fig. 7.16 Local variation source at frequency $f_2 = 1$ kHz reported in Fig. 7.14b.

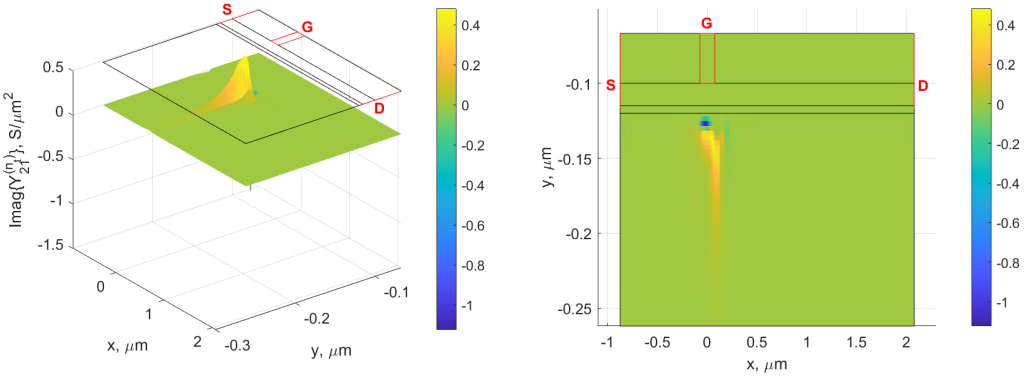

(a) 3D spatial distribution. (b) 2D spatial distribution.

Fig. 7.17 Local variation source at frequency $f_3 = 10$ kHz reported in Fig. 7.14b.

7.4 Conclusions

In this chapter, an efficient implementation of the in-house TCAD drift-diffusion model coupled to the trap rate equation is presented. The model is validated, with excellent results, in DC conditions, where the effect of traps is investigated as a function of the trap model parameters, i.e. concentration and energy level. A degradation of the drain current is obtained both with increasing concentration N_t and energy level E_{Ct}. Furthermore, the model is applied in AC conditions through the analysis of the Y parameter low-frequency dispersion, showing the Y parameter sensitivity to the trap energy and the corresponding local sensitivity. In particular, the imaginary part of Y_{22} is reported showing that Fe-doped traps are responsible of the positive frequency peak at 2.15 kHz, which is shifted towards higher values with decreasing E_{Ct}. Moreover, $\mathrm{Imag}\{\Delta Y_{22}^{(n_t)}\}$ highlights that the local variation source $\tilde{LS}_D^{(n_t)}$, concentrated in the buffer region below the gate, is slightly shifted towards the drain contact with increasing frequency. On the other hand, the imaginary part of Y_{21} has a positive peak at 250 Hz and a negative peak at 3 kHz due to buffer traps. The latter increases in terms of frequencies with decreasing E_{Ct}. The analysis of $\mathrm{Imag}\{\Delta Y_{21}^{(n_t)}\}$ demonstrates that the local variation source is distributed towards the drain and more in depth of the buffer region with increasing frequency. Therefore, the GF-based technique is a powerful tool not only to compute the sensitivity of the AC Y parameters in a numerically efficient and accurate way, but also to extract the local sensitivity, showing the areas of the device where traps influence most the HEMT AC features. Finally, the presented AC analysis can be readily extended to the dynamic large-signal analysis with no further code variations.

Chapter 8

Conclusions

Physics-based simulations represent a powerful tool to understand the behavior of active devices exploiting both conventional and innovative techniques able to describe the electrical, optical and thermal properties. The continued shrinking of transistors to even smaller dimensions has led to critical aspects, such as a significant technological variability, the strong impact of parasitics and a difficult thermal management. Consequences of this process are especially relevant in the wide panorama of RF/microwave devices, from the conventional MOSFET device to the most recent innovative technologies, such as Tunnel FETs, FeFETs, GaN HEMT and FinFETs. The consequent spread of microwave device performance makes necessary a physics-based sensitivity analysis with respect to physical and technological parameters in both static and dynamic conditions.

An in-house, pre-existing 2D physics-based simulator, allowing for LS multi-tone periodic and quasi-periodic analysis through the HB technique, has been extended. The original version of the in-house code is based on the drift-diffusion model, implemented on MATLAB® with the Sharfetter-Gummel discretization technique. It has been extended to take into account all the temperature dependencies, entering in a wide set of physical models. The T-dependent TCAD solver has been enhanced through the implementation of the self-heating equation, which takes into account the heat dissipation inside the device. Further improvements have been achieved through the refinement of the pre-existing trap rate equation, the thermionic emission model and the piezoelectric polarization model, which have a central role in the simulation of heterostructure devices, especially based on III-V semiconductors. The in-house

simulator gives the possibility to perform mixed-mode simulations, allowing for the analysis of circuits including single and multiple interacting devices. Mixed-mode simulations are directly performed in the frequency domain exploiting the HB technique, making the in-house solver well suited for the analysis of RF/microwave devices. A significant impact on the behavior of active devices is due to frequency dispersion phenomena, which can be investigated through the self-heating equation and the trap rate equation, making the in-house simulator very appealing with respect to commercial solvers. On the other hand, including multiple physical effects in TCAD simulations requires coupling additional equations to the original drift-diffusion model leading to extra simulation time that may prove a limiting factor in the widespread diffusion of TCAD tools. To overcome these limits one can rely on the continuous amelioration of computation capabilities and, most significantly, on new techniques for agile and flexible sensitivity analysis. From the TCAD standpoint, the modeling approach adopted in this work is based on the Green's Functions technique. The TCAD solver allows for a numerically efficient way to estimate the relevant GFs, which represents a generalization of the Adjoint method [64, 65], namely Generalized Adjoint Approach [57, 66, 67]. The GF technique is, thus, exploited for an efficient sensitivity analysis aimed at calculating the device response to a small variation of physical/technological parameters from a nominal condition.

A temperature-dependent sensitivity analysis is proposed, presented and demonstrated in a 54 nm Si FinFET Class A power amplifier in both the DC case, including self-heating, and the LS regime. The technique always shows an excellent agreement of the GF approach with incremental TCAD simulations and an advantage in terms of simulation time of about 20% [70]. T-dependent simulations show a strong degradation of the DC drain current at increasing temperature, especially in presence of a thermal resistance, while in LS regime they present a detailed degradation of output power in all operating conditions, showing more than 1 dB power reduction at $T = 350$ K. The thermal sensitivity is demonstrated to be higher in back-off and limited in compression, where the output power variation due to T is dominated by the knee-voltage walk-out. LS T-dependent simulations with concurrent load variations demonstrate that the stage is dominated by thermal degradation [73], while concurrent T and doping variations in LS regime show that the PA output power is significantly affected: at 1 dB compression point the available gain exhibits about 1 dB available power spread with doping at $T = 320$ K [74].

A complete dynamic thermal analysis is demonstrated on the same device exploiting the Xpar model, extracted from LS TCAD simulations in a 50 Ω environment, into Keysight ADS. The T-Xpar model is validated against LS TCAD analysis, including self-heating, and accurately predicts the PA mismatch with increasing temperature and varying back-off condition [89, 90]. It reproduces the reduction of the maximum output power and the variation of the DC power consumption due to the knee voltage thermal walk-out. In the range [300-390] K, there is more than 15% power loss, 2 dB gain degradation and up to 10 percentage points efficiency loss. Exploiting the ADS envelope analysis, the effect of PA self-heating in pulsed operating conditions is demonstrated, highlighting the effect of thermal memory. Finally, the pulsed operated analysis is repeated for a Class B power amplifier in order to highlight the different role of thermal memory with a different bias condition [91].

As a further significant example, the GaN-based HEMT technology is addressed. DC and AC sensitivity analyses are performed to investigate the impact of traps on 0.150 μm Fe-doped AlGaN/GaN HEMT. The GF approach is exploited to compute the DC sensitivity with respect to a variation of a trap physical parameter, showing accurate results with respect to repeated DC TCAD simulations at varied model parameters. The analysis demonstrates a reduction of the drain current with increasing Fe-doped trap concentration from $-15\%N_{\mathrm{t}}$ to $15\%N_{\mathrm{t}}$, while the same trend is obtained varying the trap energy level from 0.4 eV to 0.5 eV. Moreover, traps are responsible of the low-frequency dispersion of AC performance. Here, the GF approach is exploited to compute the sensitivity of the AC Y parameters towards the variation of the trap energy. Due to the presence of buffer traps, the frequency peak of $\mathrm{Imag}\{Y_{22}\}$ shows frequency dispersion with a shift towards higher frequency values with decreasing trap energy level, while two frequency peaks can be noticed in the imaginary part of the Y_{21} parameter. The negative peak, due to buffer traps, is shifted towards higher frequencies with a reduction of the trap energy, while the positive peak is almost insensitive to energy variations. In this analysis the GF approach is also exploited to extract the local sensitivity, giving a unique insight into the device operating conditions and showing the parts of the device where traps influence most the HEMT AC parameter.

References

[1] J. Mazurier, O. Weber, F. Andrieu, A. Toffoli, O. Rozeau, T. Poiroux, F. Allain, P. Perreau, C. Fenouillet-Beranger, O. Thomas, M. Belleville, and O. Faynot. On the variability in planar FDSOI technology: From MOSFETs to SRAM Cells. *IEEE Transactions on Electron Devices*, 58(8):2326–2336, 2011.

[2] Y. Liu and J. S. Yuan. CMOS RF power amplifier variability and reliability resilient biasing design and analysis. *IEEE Transactions on Electron Devices*, 58(2):540–546, 2011.

[3] P.G. Mautry and J. Trager. Self-heating and temperature measurement in sub-μm MOSFETs. In *19th European Solid State Device Research Conference (ESSDERC)*, page 675–678. Institute of Electrical and Electronics Engineers (IEEE), 1989.

[4] C. Prasad, L. Jiang, D. Singh, M. Agostinelli, C. Auth, P. Bai, T. Eiles, J. HicksC. H. Jan, K. Mistry, S. Natarajan, B. Niu, P. Packan, D. Pantuso, I. Post, S. Ramey, A. Schmitz, B. Sell, S. Suthram, J. Thomas, C. Tsai, and P. Vandervoorn. Self-heat reliability considerations on Intel's 22nm Tri-Gate technology. In *2013 IEEE International Reliability Physics Symposium (IRPS)*, page 675–678. Institute of Electrical and Electronics Engineers (IEEE), 2013.

[5] J.C. Nallatamby, J. A. Silva Dos Santos, P. V. Raja, M. Bouslama, and R. Sommet. Surface and buffer trap signatures in fe-doped AlGaN/GaN HEMT identified by LF S-parameter TCAD simulations. In *2022 17th European Microwave Integrated Circuits Conference (EuMIC)*. Institute of Electrical and Electronics Engineers (IEEE), Sept. 2022.

[6] N. K. Subramani. *Physics-based TCAD device simulations and measurements of GaN HEMT technology for RF power amplifier applications*. PhD thesis, Université de Limoges, 2017.

[7] G. Masetti, M. Severi, and S. Solmi. Modeling of carrier mobility against carrier concentration in Arsenic-, Phosphorus-, and Boron-Doped Silicon. *IEEE Transactions on Electron Devices*, ED-30(7):764–769, 1983.

[8] W. R. Thurber, R. L. Mattis, Y. M. Liu, and J. J. Filliben. The relationship between resistivity and dopant density for phosphorusand boron-doped silicon. *NBS Special Publication*, pages 400–64, 1981.

[9] N. D. Arora, J. R. Hauser, and D. J. Roulston. Electron and hole mobilities in silicon as a function of concentration and temperature. *IEEE Transactions on Electron Devices*, ED-29(72):292–295, 1982.

[10] H. Hjelmgren and Ting-Wei Tang. Thermionic emission in a hydrodynamic model for heterojunction structures. *Solid-State Electronics*, 37(9):1649–1657, 1994.

[11] Mark R. Pinto. *Comprehensive semiconductor device simulation for silicon ULSI*. PhD thesis, Stanford University, 1990.

[12] S. Donati Guerrieri. *Linear and Nonlinear Physics-Based Noise Analysis of Semiconductor Devices Through the Impedance Field Method*. PhD thesis, Politecnico di Torino, Università di Genova, Università di Trento, 1999.

[13] F. Bonani and G. Ghione. *Noise in Semiconductor Devices, Modeling and Simulation*. Springer-Verlag, Berlin, 2001.

[14] Sean J. Gillespie, David E. Root, Mihai Marcu, and Peter H. Aaen. Electrothermal X-Parameters for dynamic modeling of RF and microwave power transistors. In *2018 13th European Microwave Integrated Circuits Conference (EuMIC)*. Institute of Electrical and Electronics Engineers (IEEE), Sept. 2018.

[15] Y. Taur and H. Ning. *Fundamentals of Modern VLSI Devices, Second Edition*. Cambridge University Press, 2009.

[16] S. Donati Guerrieri, F. Bonani, and G. Ghione. Physics-based analysis to address critical aspects of FinFET mm-wave applications: Variability and thermal management. In *2019 PhotonIcs and Electromagnetics Research Symposium - Spring (PIERS-Spring)*. Institute of Electrical and Electronics Engineers (IEEE), June 2019.

[17] S. Donati Guerrieri, F. Bonani, F. Bertazzi, and G. Ghione. A unified approach to the sensitivity and variability physics-based modeling of semiconductor devices operated in dynamic conditions—Part I: Large-signal sensitivity. *IEEE Transactions on Electron Devices*, 63(3):1195–1201, mar 2016.

[18] U. Mishra and J. Singh. *Semiconductor Device Physics and Design*. Springer, 2008.

[19] F. Bonani, S. Donati Guerrieri, G. Ghione, and M. Pirola. A TCAD approach to the physics-based modeling of frequency conversion and noise in semiconductor devices under large-signal forced operation. *IEEE Transactions on Electron Devices*, 48(5):966–977, may 2001.

[20] C. Prasad. A review of self-heating effects in advanced CMOS technologies. *IEEE Transactions on Electron Devices*, 66(11):4546–4555, nov 2019.

[21] F. Bonani, V. Camarchia, F. Cappelluti, S. Donati Guerrieri, G. Ghione, and M. Pirola. When self-consistency makes a difference. *IEEE Microwave Magazine*, 9(5):81–89, oct 2008.

[22] W. Shockley. *Electrons and Holes in Semiconductors*. D.Van Nostrand Company Inc., 1950.

[23] W. Van Roosbroeck. *Theory of the flow of electrons and holes in germanium and other semiconductors*. Nokia Bell Labs, Princenton, NJ, 1950.

[24] S.M. Sze and Kwok K. Ng. *Physics of Semiconductor Devices*. John Wiley and Sons, Inc., 2006.

[25] Alan H.Marshak and David Assaf III. A generalized Einstein relation for semiconductors. *Solid-State Electronics*, 16:675–679, 1973.

[26] https://www.synopsys.com/silicon/tcad/device-simulation/sentaurus-device.html.

[27] S. D. Guerrieri, E. Catoggio, and F. Bonani. Tcad simulation of microwave circuits: The doherty amplifier. *Solid-State Electronics*, 197:108445, 2022.

[28] S. A. Maas. *Nonlinear Microwave Circuits*. Artech House, 1988.

[29] B. Troyanovsky. *Frequency Domain Algorithms For Simulating Large Signal Distortion in Semiconductor Devices*. PhD thesis, Stanford University, Department of Electrical Engineering, 1997.

[30] C. Prasad. A review of self-heating effects in advanced CMOS technologies. *IEEE Transactions on Electron Devices*, 66(11):4546–4555, 2019.

[31] P. Emilio Bagnoli, C. Casarosa, M. Ciampi, and E. Dallago. Thermal resistance analysis by induced transient (TRAIT) method for power electronic devices thermal characterization—Part I: Fundamentals and theory. *IEEE Transactions on Power Electronics*, 13(6):1208–1219, 1998.

[32] J. G. Felbinger, M.V.S. Chandra, Y. Sun, L. F. Eastman, J. Wasserbauer, F. Faili, D. Babic, D. Francis, and F. Ejeckam. Comparison of GaN HEMTs on diamond and SiC substrates. *IEEE Electron Device Letters*, 28(11):948–950, oct 2007.

[33] B. Lu and T. Palacios. High breakdown (> 1500 v) AlGaN/GaN HEMTs by substrate-transfer technology. *IEEE Electron Device Letters*, 31(9):951–953, sep 2010.

[34] R. S. Pengelly, S. M. Wood, J. W. Milligan, S. T. Sheppard, and W. L. Pribble. A review of GaN on sic high electron-mobility power transistors and mmics. *IEEE Transactions Microwave Theory and Techniques*, 60(6):1764 – 1783, 1998.

[35] Y. F. Wu, M. Moore, A. Saxler, T. Wisleder, and P. Parikh. 40-W/mm double field-plated GaN HEMTs. In *64th Device Research Conference*, page 151–152. Institute of Electrical and Electronics Engineers (IEEE), 2007.

[36] J. W. Chung, W. E. Hoke, E. M. Chumbes, and T. Palacios. AlGaN/GaN HEMT with 300-GHz. *IEEE Electron Device Letters*, 31(3):195–197, mar 2010.

[37] M. J. Uren, K. J. Nash, R. S. Balmer, T. Martin, E. Morvan, N. Caillas, S. L. Delage, D. Ducatteau, B. Grimbert, and J. C. De Jaeger. Punch-through in short-channel AlGaN/GaN FETs. *IEEE Transactions on Electron Devices*, 53(2):395–398, feb 2006.

[38] W. Bludau, A. Onton, and W. Heinke. Temperature dependence of the band gap in silicon. *Journal of Applied Physics*, 45(4):1846–1848, 1974.

[39] C. Lombardi, S. Manzini, A. Saporito, and M. Vanzi. A physically based mobility model for numerical simulation of nonplanar devices. *Transaction of computer-aided design*, 7(11):1164–1171, 1988.

[40] C. Canali; G. Majni; R. Minder; G. Ottaviani. Electron and hole drift velocity measurements in silicon and their empirical relation to electric field and temperature. *IEEE Transactions on Electron Devices*, ED-22(11):1045–1047, 1975.

[41] D. M. Caughey and R. E. Thomas. Carrier mobilities in silicon empirically related to doping and field. In *Proceedings of the IEEE*, volume 55, pages 2192–2193. Institute of Electrical and Electronics Engineers (IEEE), Dec. 1967.

[42] H. W. Thim. Computer study of bulk GaAs devices with random one-dimensional doping fluctuations. *Journal of Applied Physics*, 39(8):3897–3904, 1968.

[43] K. Horio and H. Yanai. Numerical modeling of heterojunctions including the thermionic emission mechanism at the heterojunction interface. *IEEE Transactions on Electron Devices*, 37(3):1093–1908, 1990.

[44] O. Ambacher, J. Smart, J. R. Shealy, N. G. Weimann, K. Chu, M. Murphy, W. J. Schaff, L. F. Eastman, R. Dimitrov, L. Wittmer, M. Stutzmann, W. Rieger, and J. Hilsenbeck. Two-dimensional electron gases induced by spontaneous and piezoelectric polarization charges in N- and Ga-face AlGaN/GaN heterostructures. *Journal of Applied Physics*, 85(6):3222–3233, 1999.

[45] S. Selberherr. *Analysis and Simulation of Semiconductor Devices*. Springer-Verlag, Wien, 1984.

[46] J. D. Lambert. *Numerical Methods for Ordinary Differential Systems: The Initial Value Problem*. John Wiley and Sons, Inc., 1992.

[47] R. S. Varga. *Matrix iterative analysis*. Springer, 1962.

[48] M. Brown Barron. *Computer Aided Analysis of Insulated Gate Field Effect Transistors*. PhD thesis, Stanford University, 1969.

[49] C. H. Price. *Two-Dimensional Numerical Simulation of Semiconductor Devices*. PhD thesis, Stanford University, 1982.

[50] D. L. Scharfetter and H. K. Gummel. Large-signal analysis of a silicon read diode oscillator. *IEEE Transactions on Electron Devices*, 16(1):64–77, 1969.

[51] J. Sato-Iwanaga, K. Fujimoto, Y. Ota, K. Inoue, B. Troyanovsky, and R. W. Dutton Z. Yu. Distortion analysis of GaAs MESFETs based on physical model using PISCES-HB. In *International Electron Devices Meeting, San Francisco, USA*, pages 163–166. Institute of Electrical and Electronics Engineers (IEEE), Dec. 1996.

[52] K. S. Kundert, J. K. White, and A. Sangiovanni-Vincentelli. *Steady-state methods for simulating analog and microwave circuits*. Kluwer Academic Publishers, Boston, 1990.

[53] S. Donati Guerrieri, F. Bonani, M. Pirola, and G. Ghione. Sensitivity-based optimization and statistical analysis of microwave semiconductor devices through multidimensional physical simulation. *International Journal of Microwave and Millimeter-Wave Computer-Aided Engineering*, 7(1):129–143, 1997.

[54] F. Bonani, S. Donati Guerrieri, F. Filicori, G. Ghione, and M. Pirola. Physics-based large-signal sensitivity analysis of microwave circuits using technological parametric sensitivity from multidimensional semiconductor device models. *IEEE Transactions on Microwave Theory and Techniques*, 45(5):846–855, 1997.

[55] J. M. Ortega and W. C. Rheinboldt. *Iterative Solution of Nonlinear Equations in Several Variables*. New York: Academic Press, 1970.

[56] W. Shockley, J. A. Copeland, and R. P. James. The impedance field method of noise calculation in active semiconductor devices. *Quantum theory of atoms, molecules, and the solid-state*, pages 537–563, 1966.

[57] F. Bonani, G. Ghione, M. R. Pinto, and R. K. Smith. An efficient approach to noise analysis through multidimensional physics-based models. *IEEE Transactions on Electron Devices*, 45(1):261–269, 1998.

[58] F. Bonani, S. Donati Guerrieri, and G. Ghione. Physics-based simulation techniques for small- and large-signal device noise analysis in RF applications. *IEEE Transactions on Electron Devices*, 50(3):633–644, mar 2003.

[59] S. Donati Guerrieri, F. Bonani, F. Bertazzi, and G. Ghione. A unified approach to the sensitivity and variability physics-based modeling of semiconductor devices operated in dynamic conditions.—Part II: Small-signal and conversion matrix sensitivity. *IEEE Transactions on Electron Devices*, 63(3):1202–1208, mar 2016.

[60] C. M. van Vliet. Macroscopic and microscopic methods for noise in devices. *IEEE Transactions on Electron Devices*, 41(11):1902–1915, 1994.

[61] S.E. Laux. Techniques for small-signal analysis of semiconductor devices. *IEEE Transactions on Electron Devices*, 32(10):2028–2037, 1985.

[62] K. M. van Vliet, A. Friedman, R. J. J. Zijlstra, A. Gisolf, and A. van der Ziel. Noise in single injection diodes. I: A survey of methods. *Journal of Applied Physics*, 46:1804–1813, 1975.

[63] F. H. Branin. IEEE transactions on circuit theory. *Network sensitivity and noise analysis simplied*, 20(3):285–288, 1973.

[64] S. Director and R. Rohrer. IEEE transactions on circuit theory. *Automated network design-The frequency-domain case*, 16(3):330–337, 1969.

[65] F. H. Branin. IEEE journal of solid-state circuits. *Computationally efficient electronic-circuit noise calculations*, 6(4):204–213, 1971.

[66] F. Bonani, G. Ghione, M. R. Pinto, and R. K. Smith. A novel implementation of noise analysis in general-purpose PDE-based semiconductor device simulators. In *Proceedings of International Electron Devices Meeting, Washington, DC, USA*. Institute of Electrical and Electronics Engineers (IEEE), Dec. 1995.

[67] F. Bonani, M. R. Pinto, R. K. Smith, and G. Ghione. An efficient approach to multi-dimensional impedance field noise simulation of bipolar devices. In *Proceedings of the 13th International Conference on Noise in Physical Systems and 1/f Fluctuations*. V. Bareikis, R. Katilius (World Scientific, Singapore), 1995.

[68] R. J. Gilmore and M. B. Steer. IEEE journal of microwave and millimiter-wave computater-aided engineering. *Nonlinear circuit analysis using the method of harmonic balance—a review of the art. II. Advanced concepts*, 1(2):159–180, 1991.

[69] J. Roychowdhury, D. Long, and P. Feldmann. IEEE journal of solid-state circuits. *Cyclostationary noise analysis of large RF circuits with multitone excitations*, 33(3):324–336, 1971.

[70] E. Catoggio, S. Donati Guerrieri, and F. Bonani. Efficient TCAD thermal analysis of semiconductor devices. *IEEE Transactions on Electron Devices*, 68(11):5462 – 5468, 2021.

[71] A. M. Bughio, S. Donati Guerrieri, F. Bonani, and G. Ghione. Physics-based modeling of FinFET RF variability. In *2016 11th European Microwave Integrated Circuits Conference (EuMIC)*. IEEE, oct 2016.

[72] S. Donati Guerrieri, C. Ramella, F. Bonani, and G. Ghione. Efficient sensitivity and variability analysis of nonlinear microwave stages through concurrent TCAD and EM modeling. *IEEE Journal on Multiscale and Multiphysics Computational Techniques*, 4:356–363, 2019.

[73] E. Catoggio, S. Donati Guerrieri, F. Bonani, and G. Ghione. Efficient TCAD temperature-dependent large-signal simulation of a FinFET power amplifier. In *2021 16th European Microwave Integrated Circuits Conference (EuMIC)*. Institute of Electrical and Electronics Engineers (IEEE), Jun 2022.

[74] E. Catoggio, S. Donati Guerrieri, F. Bonani, and G. Ghione. Efficient TCAD large-signal temperature-dependent variability analysis of a FinFET power amplifier. In *2021 International Conference on Simulation of Semiconductor Processes and Devices (SISPAD)*. Institute of Electrical and Electronics Engineers (IEEE), Sep. 2021.

[75] Jean-Pierre Raskin. FinFET versus UTBB SOI — a RF perspective. In *2015 45th European Solid State Device Research Conference (ESSDERC)*. IEEE, sep 2015.

[76] A. M. Bughio, S. Donati Guerrieri, F. Bonani, and G. Ghione. Multi-gate FinFET mixer variability assessment through physics-based simulation. *IEEE Electron Device Letters*, 38(8):1004–1007, aug 2017.

[77] S. Callender, S. Pellerano, and C. Hull. An E -band power amplifier with 26.3% PAE and 24-GHz bandwidth in 22-nm FinFET CMOS. *IEEE Journal of Solid-State Circuits*, 54(5):1266–1273, may 2019.

[78] H.-J. Lee, B. Sell, Y. Zhang, S. Morarka, S. Rami, Q. Yu, M. Weiss, G. Liu, M. Armstrong, C. Y. Su, and D. Ali. Implementation of high power RF devices with hybrid workfunction and OxideThickness in 22nm low-power FinFET technology. In *2019 IEEE International Electron Devices Meeting (IEDM)*. IEEE, dec 2019.

[79] Ken Uchida and Tsunaki Takahashi. Thermal-aware CMOS: Challenges for future technology and design evolutions. In *2016 46th European Solid-State Device Research Conference (ESSDERC)*. IEEE, sep 2016.

[80] M. Yunik. *Design of Modern Transistor Circuits*. Prentice-Hall Inc., 1973.

[81] S. Donati Guerrieri, F. Bonani, and G. Ghione. A comprehensive technique for the assessment of microwave circuit design variability through physical simulations. In *2017 IEEE MTT-S International Microwave Symposium (IMS)*. IEEE, jun 2017.

[82] Simona Donati Guerrieri, Marco Pirola, and Fabrizio Bonani. Concurrent efficient evaluation of small-change parameters and Green's Functions for TCAD device noise and variability analysis. *IEEE Transactions on Electron Devices*, 64(3):1269–1275, mar 2017.

[83] S. Donati Guerrieri, F. Bonani, and G. Ghione. TCAD analysis of FinFET temperature-dependent variability for analog applications. In *2019 International Conference on Simulation of Semiconductor Processes and Devices (SISPAD)*. IEEE, sep 2019.

[84] S. Donati Guerrieri, C. Ramella, E. Catoggio, and F. Bonani. Bridging the gap between physical and circuit analysis for variability-aware microwave design: Modeling approaches. *Electronics*, 11(6):860, mar 2022.

[85] S. Donati Guerrieri, F. Bonani, and G. Ghione. Linking X parameters to physical simulations for design-oriented large-signal device variability modeling. In *2019 IEEE MTT-S International Microwave Symposium (IMS)*. IEEE, jun 2019.

[86] D. Root, J. Horn, J. Verspecht, and M. Marcu. *X-Parameters*. Cambridge University Press, 2013.

[87] S. Donati Guerrieri, F. Bonani, and G. Ghione. Physically-based statistical analysis of nonlinear circuits through X-parameters. In *2019 14th European Microwave Integrated Circuits Conference (EuMIC)*. IEEE, sep 2019.

[88] https://www.keysight.com/zz/en/products/software/pathwave-design-software/pathwave-advanced-design-system.html.

[89] E. Catoggio, S. Donati Guerrieri, C. Ramella, and F. Bonani. Thermal modeling of RF FinFET PAs through temperature-dependent x-parameters extracted from physics-based simulations. In *2022 International Workshop on Integrated Nonlinear Microwave and Millimetre-Wave Circuits (INMMiC)*. IEEE, apr 2022.

[90] S. Donati Guerrieri, C. Ramella, E. Catoggio, and F. Bonani. TCAD-based dynamic thermal X-parameters for PA self-heating analysis. In *2022 17th European Microwave Integrated Circuits Conference (EuMIC)*. Institute of Electrical and Electronics Engineers (IEEE), Sept. 2022.

[91] E. Catoggio, S. Donati Guerrieri, C. Ramella, and F. Bonani. Multi-bias thermal X-Parameter model for efficient physics-based FinFET simulation in RF CAD tools. In *Proceedings of SIE 2022*. Springer, 2023.

[92] N. Craig, V. Zomorrodian, S. Warren, and J. Gengler. Measurement-based temperature-dependent X-Parameter models from high-Power MMIC power amplifiers. In *2018 IEEE 19th Wireless and Microwave Technology Conference (WAMICON)*. Institute of Electrical and Electronics Engineers (IEEE), 2018.

[93] A. Chernenko and E. Ziganshin. Pulse-doppler UWB radar. In *2006 3rd International Conference on Ultrawideband and Ultrashort Impulse Signals*. IEEE, sep 2006.

[94] Hiroshi Matsumura, Ikuo Soga, Shoichi Shiba, Kazuaki Oishi, Yoichi Kawano, Yasuhiro Nakasha, and Toshihide Suzuki. E-band impulse radio transceiver with 2-bit pulse-position modulation. In *2018 15th European Radar Conference (EuRAD)*. IEEE, sep 2018.

[95] A. M. Angelotti, G. P. Gibiino, A. Santarelli, and C. Florian. Experimental characterization of charge trapping dynamics in 100-nm AlN/GaN/alGaN-on-Si HEMTs by wideband transient measurements. *IEEE Transactions on Electron Devices*, 67(8):3069 – 3074, jun 2020.

[96] N. Zagni, A. Chini, F. M. Puglisi, P. Pavan, and G. Verzellesi. On the modeling of the Donor/Aceptor compensation ratio in Carbon-doped GaN to univocally reproduce breakdown voltage and current collapse in lateral GaN power HEMTs. *Micromachines*, 12(6), jun 2021.

[97] P. Beleniotis, F. Schnieder, S. Chevtchenko, and M. Rudolph. Localization of trapping effects in GaN HEMTs with pulsed S-parameters and compact models. In *2022 17th European Microwave Integrated Circuits Conference (EuMIC)*. Institute of Electrical and Electronics Engineers (IEEE), Sept. 2022.

[98] P. Vigneshwara Raja, Nandha Kumar Subramani, Florent Gaillard, Mohamed Bouslama, Raphaël Sommet, and Jean-Christophe Nallatamby. Identification of buffer and surface traps in fe-doped AlGaN/GaN HEMTs using Y21 frequency dispersion properties. *Electronics*, 10(24):3096, dec 2021.

[99] A. Chini, V. Di Lecce, M. Esposto, G. Meneghesso, and E. Zanoni. Evaluation and numerical simulations of GaN HEMTs electrical degradation. *IEEE Electron Device Letters*, 30(10), oct 2009.

[100] k. Sharma, A. Dasgupta, S. Ghosh, S. A. Ahsan, S. Khandelwal, and Y. Singh Chauhan. Effect of access region and field plate on capacitance behavior of GaN HEMT. In *2015 IEEE International Conference on Electron Devices and Solid-State Circuits (EDSSC)*. Institute of Electrical and Electronics Engineers (IEEE), 2015.

[101] S. Sarkar, R. P. Khade, A. DasGupta, and N. DasGupta. Effect of GaN cap layer on the performance of AlInN/GaN-based HEMTs. *Microelectronic Engineering*, 258:111756, 2022.

Appendix A

The Harmonic Balance Technique

Consider the generic mixed-mode configuration of a non-linear microwave circuit of Fig. A.1, characterized by the active device, which is a non-linear component, and the input/output linear matching networks [12]. An external time-dependent voltage $v_{\text{in}}(t)$ of arbitrary amplitude is applied to the input terminal. If the peak amplitude of the input source is not small enough, the device operates in Large-Signal conditions where harmonic components will be generated and the linearization procedure can not be performed. The LS input can be composed of one or two tones plus a DC bias, therefore the circuit operates in a periodic or quasi-periodic LS regime, respectively. As a consequence, all the terminals voltages $v_k(t)$ and currents $i_k(t)$ involved in the microwave circuit are periodic or quasi-periodic functions of time. The periodic and quasi-periodic LS regime has a great relevance in the design of devices for analog applications, especially in the RF and microwave fields where most of the applications show non-linearities.

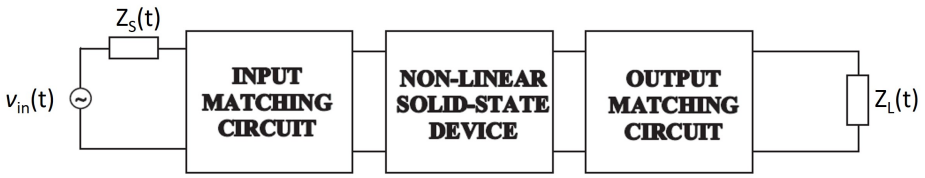

Fig. A.1 Schematic representation of a mixed-mode configuration characterized by solide-state device connected to the input and output matching network.

Voltage and current components can be written in the time-domain regime or in a frequency-domain regime. Frequency domain approaches are usually preferred

because they are easier and more efficient solutions for periodic or quasi-periodic operation regimes. One of the main used techniques suited for non-linear networks is the *Harmonic Balance* (HB) method [28], whose initial formulation considers all the frequencies generated by the circuit belonging to the set nf_0 (n integer). The frequency f_0 can be associated to a single-tone sinusoidal excitation or to a set of commensurate[1] excitations.

Let's consider the case of a single-tone periodic LS excitation at fundamental frequency ω_0:

$$\omega_i = i\omega_0 \qquad i = 0,1,2,...,N_{\mathrm{H}} \tag{A.1}$$

The time-dependent signal can be expressed in terms of voltage or current as the real Fourier expansion truncated at the upper harmonic N_{H}:

$$i_k(t) = i_{k0} + \sum_{i=1}^{N_{\mathrm{H}}} [i_{kci}\ cos(i\omega_0 t) + i_{ksi}\ sin(i\omega_0 t)] \tag{A.2a}$$

$$v_k(t) = v_{k0} + \sum_{i=1}^{N_{\mathrm{H}}} [v_{kci}\ cos(i\omega_0 t) + v_{ksi}\ sin(i\omega_0 t)] \tag{A.2b}$$

It is possible to write the same expressions in a vector form with $2N_{\mathrm{H}}+1$ elements including the DC component:

$$i_k(t) \Longleftrightarrow [i_{k0}, i_{kc1}, i_{ks1}, i_{kc2}, i_{ks2}, ..., i_{kcN_{\mathrm{H}}}, i_{ksN_{\mathrm{H}}}]^T = i_{k\mathrm{H}}^T \tag{A.3a}$$

$$v_k(t) \Longleftrightarrow [v_{k0}, v_{kc1}, v_{ks1}, v_{kc2}, v_{ks2}, ..., v_{kcN_{\mathrm{H}}}, v_{ksN_{\mathrm{H}}}]^T = v_{k\mathrm{H}}^T \tag{A.3b}$$

At the same time, signals in time domain can be sampled into $2N_{\mathrm{H}}+1$ equispaced times, therefore calling T_0 the fundamental period, voltages and currents can be expressed as time sample arrays:

$$i_k(t) \Longleftrightarrow [i_k(t_1), i_k(t_2), ..., i_k(t_{2N_{\mathrm{H}}+1})]^T = i_k^T \tag{A.4a}$$

$$v_k(t) \Longleftrightarrow [v_k(t_1), v_k(t_2), ..., v_k(t_{2N_{\mathrm{H}}+1})]^T = v_k^T \tag{A.4b}$$

[1] A set of frequencies is commensurate when all the possible ratios between any two frequencies are rational numbers.

Knowing that:

$$i_k(t_n) = i_{k0} + \sum_{i=1}^{N_\mathrm{H}} [i_{kci}\ cos(i\omega_0 t_n) + I_{ksi}\ sin(i\omega_0 t_n)] = \mathbf{\Gamma}_n^{-1} \cdot i_{k\mathrm{H}} \tag{A.5a}$$

$$v_k(t_n) = v_{k0} + \sum_{i=1}^{N_\mathrm{H}} [v_{kci}\ cos(i\omega_0 t_n) + v_{ksi}\ sin(i\omega_0 t_n)] = \mathbf{\Gamma}_n^{-1} \cdot v_{k\mathrm{H}} \tag{A.5b}$$

where

$$\mathbf{\Gamma}_n^{-1} = [1, cos(\omega_0 t_n), sin(\omega_0 t_n), cos(2\omega_0 t_n), sin(2\omega_0 t_n), ..., cos(N_\mathrm{H}\omega_0 t_n), sin(N_\mathrm{H}\omega_0 t_n)] \tag{A.6}$$

The matrix $\mathbf{\Gamma}^{-1}$ can be defined having $\mathbf{\Gamma}_n^{-1}$ as rows:

$$\mathbf{\Gamma}^{-1} = \begin{pmatrix} 1 & cos(\omega_0 t_1) & sin(\omega_0 t_1) & \dots & cos(N_\mathrm{H}\omega_0 t_1) & sin(N_\mathrm{H}\omega_0 t_1) \\ 1 & cos(\omega_0 t_2) & sin(\omega_0 t_2) & \dots & cos(N_\mathrm{H}\omega_0 t_2) & sin(N_\mathrm{H}\omega_0 t_2) \\ \vdots & \vdots & \vdots & \ddots & \vdots & \vdots \\ 1 & cos(\omega_0 t_{2N_\mathrm{H}+1}) & sin(\omega_0 t_{2N_\mathrm{H}+1}) & \dots & cos(N_\mathrm{H}\omega_0 t_{2N_\mathrm{H}+1}) & sin(N_\mathrm{H}\omega_0 t_{2N_\mathrm{H}+1}) \end{pmatrix} \tag{A.7}$$

We finally obtain the following expressions:

$$i_k = \mathbf{\Gamma}^{-1} \cdot i_{k\mathrm{H}} \qquad v_k = \mathbf{\Gamma}^{-1} \cdot v_k \tag{A.8a}$$

$$i_{k\mathrm{H}} = \mathbf{\Gamma} \cdot i_k \qquad v_{k\mathrm{H}} = \mathbf{\Gamma} \cdot v_k \tag{A.8b}$$

A non-linear network can be characterized by linear reactive elements such as capacitors and inductors, whose expressions depend on the time derivatives of voltages and currents, respectively. In this case, the truncated Fourier expansion becomes:

$$\frac{di_k(t)}{dt} = i'_k(t) = \sum_{i=1}^{N_\mathrm{H}} [-i\omega_0 i_{kci}\ sin(i\omega_0 t) + i\omega_0 i_{ksi}\ cos(i\omega_0 t)] \tag{A.9}$$

Knowing that the frequency domain array associated to $i'_k(t)$ is:

$$i'_k(t) \Longleftrightarrow [0, -\omega_0 i_{ks1}, \omega_0 i_{kc1}, -2\omega_0 i_{ks2}, 2\omega_0 i_{kc2}, ..., -N_\mathrm{H}\omega_0 i_{ksN_\mathrm{H}}, N_\mathrm{H}\omega_0 i_{kcN_\mathrm{H}}]^T \tag{A.10}$$

the final expression in matrix form can be found as follows:

$$i'_k = \begin{pmatrix} 0 \\ -\omega_0 i_{ks1} \\ \omega_0 i_{kc1} \\ \vdots \\ -N_{\mathrm{H}}\omega_0 i_{ksN_{\mathrm{H}}} \\ N_{\mathrm{H}}\omega_0 i_{kcN_{\mathrm{H}}} \end{pmatrix} = \underbrace{\begin{pmatrix} 0 & 0 & 0 & \dots & 0 & 0 \\ 0 & 0 & -\omega_0 & \dots & 0 & 0 \\ 0 & \omega_0 & 0 & \dots & 0 & 0 \\ \vdots & \vdots & \vdots & \ddots & \vdots & \vdots \\ 0 & 0 & 0 & \dots & 0 & -N_{\mathrm{H}}\omega_0 \\ 0 & 0 & 0 & \dots & N_{\mathrm{H}}\omega_0 & 0 \end{pmatrix}}_{\mathbf{\Omega}} \underbrace{\begin{pmatrix} i_0 \\ i_{kc1} \\ iI_{ks1} \\ \vdots \\ i_{kcN_{\mathrm{H}}} \\ i_{ksN_{\mathrm{H}}} \end{pmatrix}}_{\mathbf{i}_{k\mathrm{H}}} \tag{A.11}$$

In compact form we can write:

$$i'_{k\mathrm{H}} = \mathbf{\Omega} \cdot i_{k\mathrm{H}} \tag{A.12}$$

The HB formalism can be expressed in a direct (real) Fourier representation, which is more convenient in most of the non-linear circuit analyses, but it can also be exploited in a complex notation. Using the complex representation, the Fourier expansion of currents and voltages becomes:

$$i_k(t) = \sum_{n=-N_{\mathrm{H}}}^{N_{\mathrm{H}}} \tilde{I}_{kn} \exp(\mathrm{j}\omega_n t) \tag{A.13a}$$

$$v_k(t) = \sum_{n=-N_{\mathrm{H}}}^{N_{\mathrm{H}}} \tilde{V}_{kn} \exp(\mathrm{j}\omega_n t) \tag{A.13b}$$

where

$$\omega_n = n\omega_0 \qquad i = 0, \pm 1, \pm 2, ..., \pm N_{\mathrm{H}} \tag{A.14}$$

It is possible to write the same expressions in a vector form of $2N_{\mathrm{H}} + 1$ elements:

$$i_k(t) \Longleftrightarrow [\tilde{I}_{-kN_{\mathrm{H}}}, \tilde{I}_{k(-N_{\mathrm{H}}+1)}, ..., \tilde{I}_{k0}, ..., \tilde{I}_{k(N_{\mathrm{H}}-1)}, \tilde{I}_{kN\mathrm{H}}]^T \tag{A.15a}$$

$$v_k(t) \Longleftrightarrow [\tilde{V}_{-kN_{\mathrm{H}}}, \tilde{V}_{k(-N_{\mathrm{H}}+1)}, ..., \tilde{V}_{k0}, ..., \tilde{V}_{k(N_{\mathrm{H}}-1)}, \tilde{V}_{kN_{\mathrm{H}}}]^T \tag{A.15b}$$

Knowing that time domain signals can be sampled into $2N_{\mathrm{H}} + 1$ equispaced times as shown in Eq. (A.4), the previous expressions can be written in the following way:

$$i_k(t_n) = \sum_{n=-N_{\mathrm{H}}}^{N_{\mathrm{H}}} \tilde{I}_{kn} \exp(\mathrm{j}\omega_n t_n) = \tilde{\mathbf{\Gamma}}_n^{-1} \cdot \tilde{I}_{k\mathrm{H}} \tag{A.16}$$

$$v_k(t_n) = \sum_{n=-N_H}^{N_H} \tilde{V}_{kn} \exp(j\omega_n t_n) = \tilde{\mathbf{\Gamma}}_n^{-1} \cdot \tilde{V}_{kH} \tag{A.17}$$

where

$$\tilde{\mathbf{\Gamma}}_n^{-1} = [\exp(j\omega_{-N_H} t_n), ..., \exp(j\omega_0 t_n), ..., \exp(j\omega_{N_H} t_n)] \tag{A.18}$$

The matrix $\tilde{\mathbf{\Gamma}}^{-1}$ can be defined having $\tilde{\mathbf{\Gamma}}_n^{-1}$ as rows:

$$\tilde{\mathbf{\Gamma}}^{-1} = \begin{pmatrix} e^{j\omega_{-N_H} t_1} & \dots & e^{j\omega_{-1} t_1} & e^{j\omega_0 t_1} & e^{j\omega_1 t_1} & \dots & e^{j\omega_{N_H} t_1} \\ e^{j\omega_{-N_H} t_2} & \dots & e^{j\omega_{-1} t_2} & e^{j\omega_0 t_2} & e^{j\omega_1 t_2} & \dots & e^{j\omega_{N_H} t_2} \\ \vdots & \vdots & \vdots & \ddots & \vdots & \vdots & \\ e^{j\omega_{-N_H} t_{2N_H+1}} & \dots & e^{j\omega_{-1} t_{2N_H+1}} & e^{j\omega_0 t_{2N_H+1}} & e^{j\omega_1 t_{2N_H+1}} & \dots & e^{j\omega_{N_H} t_{2N_H+1}} \end{pmatrix} \tag{A.19}$$

The final expressions in matrix form are:

$$i_k = \tilde{\mathbf{\Gamma}}^{-1} \cdot \tilde{I}_{kH} \quad \mathbf{v}_k = \tilde{\mathbf{\Gamma}}^{-1} \cdot \tilde{V}_{kH} \tag{A.20}$$

$$\tilde{I}_{kH} = \tilde{\mathbf{\Gamma}} \cdot i_k \quad \tilde{V}_{kH} = \tilde{\mathbf{\Gamma}} \cdot v_k \tag{A.21}$$

As explained previously, in non-linear networks time derivatives of voltages and currents can be involved for the definition of reactive elements such as capacitors and inductors. Therefore, there is the need to express them using the HB technique in the complex domain:

$$\frac{di_k(t)}{dt} = i'_k(t) = \sum_{n=-N_H}^{N_H} j\omega_n \tilde{I}_{kn} \exp(j\tilde{\omega}_n t) \tag{A.22}$$

The frequency domain array associated to $i'_k(t)$ is:

$$i'_k(t) \Longleftrightarrow [j\omega_{-N_H} \tilde{I}_{-kN_H}, ..., j\omega_{-1} \tilde{I}_{-k1}, j\omega_0 \tilde{I}_{k0}, j\omega_1 \tilde{I}_{k1}, ..., j\omega_N \tilde{I}_{kN_H}]^T \tag{A.23}$$

Therefore, the final expression in matrix form is:

$$\tilde{I}'_{k\mathrm{H}} = \begin{pmatrix} \mathrm{j}\omega_{N_\mathrm{H}}\tilde{I}_{-kN_\mathrm{H}} \\ \vdots \\ \mathrm{j}\omega_{-1}\tilde{I}_{-k1} \\ \mathrm{j}\omega_0\tilde{I}_{k0} \\ \mathrm{j}\omega_1\tilde{I}_{k1} \\ \vdots \\ \mathrm{j}\omega_{N_\mathrm{H}}\tilde{I}_{kN_\mathrm{H}} \end{pmatrix} = \mathrm{j}\cdot \underbrace{\begin{pmatrix} \omega_{-N_\mathrm{H}} & \dots & 0 & 0 & 0 & \dots & 0 \\ \vdots & \vdots & \vdots & \ddots & \vdots & \vdots & \vdots \\ 0 & \dots & \omega_{-1} & 0 & 0 & \dots & 0 \\ 0 & \dots & 0 & \omega_0 & 0 & \dots & 0 \\ 0 & \dots & 0 & 0 & \omega_1 & \dots & 0 \\ \vdots & \vdots & \vdots & \ddots & \vdots & \vdots & \vdots \\ 0 & \dots & 0 & 0 & 0 & \dots & \omega_{N_\mathrm{H}} \end{pmatrix}}_{\tilde{\mathbf{\Omega}}} \underbrace{\begin{pmatrix} \tilde{I}_{-kN_\mathrm{H}} \\ \vdots \\ \tilde{I}_{-k1} \\ \tilde{I}_{k0} \\ \tilde{I}_{k1} \\ \vdots \\ \tilde{I}_{kN_\mathrm{H}} \end{pmatrix}}_{\tilde{I}_{k\mathrm{H}}} \tag{A.24}$$

In compact form, one can write:

$$\tilde{I}'_{k\mathrm{H}} = \tilde{\mathbf{\Omega}} \cdot \tilde{I}_{k\mathrm{H}} \tag{A.25}$$